Studies of electron transfer in self-assembled monolayers and bilayer lipid membranes

CAMPOS, RUI

Studies of Electron Transfer in Self – Assembled Monolayers and Bilayer Lipid Membranes

Rui César de Almeida Campos

A thesis submitted in part fulfilment
of the requirements for the degree of
Doctor of Philosophy

Department of Chemistry

Durham University

March 2012

I. Abstract

The work presented on this thesis is focused on studies of the kinetics of electron transfer in bilayer lipid membranes (BLMs). Three different types of BLM were studied: i) tethered, ii) pore suspended (commonly known as 'black') and iii) based on the avidin – biotin interaction (these are part of the wider group of polymer cushioned BLMs).

In order to produce tethered BLMs (tBLMs) of the best quality possible, self – assembled monolayers (SAMs) of a thiolipid (1,2-dipalmitoyl-*sn*-glycero-phosphothioethanol (DPPTE)) and of the same thiolipid mixed with L-α-phosphatidylcholine (EggPC) were characterised and their behaviour compared to that of SAMs of two alkanethiols (1 – heptanethiol and 1 – dodecanethiol). The SAMs that were formed by a mixture of lipids (DPPTE+EggPC) presented better kinetic parameters and were the chosen to produce tBLMs.

Tethered BLMs were made by using the SAM described above as the lower leaflet; the second leaflet was deposited by vesicle fusion, the vesicles were made of EggPC. tBLMs are commonly used as model membranes, however in biophysical studies free-standing membranes or 'black' lipid membranes are more realistic models of cellular processes. The rates of electron transfer in both types of bilayer lipid membranes are compared. These BLMs were modified using two very important mitochondrial membrane associated molecules – ubiquinone-10 (UQ_{10}) and α-tocopherol (VitE). The studies involved the use three redox couples, $Fe(CN)_6^{3-/4-}$, $Ru(NH_3)_6^{3+/2+}$ and NAD^+/NADH using

cyclic voltammetry and electrochemical impedance spectroscopy. The NAD^+/NADH couple is of particular interest as it is the key to several important biochemical processes.

The last type of BLM that was studied was the BLMs based on the avidin – biotin interaction. Avidin was deposited on a platinum surface by electrodeposition and then vesicles composed of EggPC and 1,2-dioleoyl-*sn*-glycero-3-phosphoethanolamine-N-(biotinyl) (sodium salt) (DOPE(B)) are burst by applying +0.7V (*vs.* Ag/AgCl, KCl 3.5M), leading to the formation of a supported BLM. The vesicles used had methylene blue (MB) inside; its release, when the vesicles burst, was monitored by cyclic voltammetry and UV-Vis. The kinetic parameters were determined based on the EIS measurements using $Fe(CN)_6^{3-/4-}$ and $Ru(NH_3)_6^{3+/2+}$ as redox couples.

"O homem é um ser inteligente, sem dúvida, mas não tanto quanto seria desejável."

"The man is an intelligent being, no doubt, but not as much as it would be desirable."

José Saramago (1922 – 2010)

Portuguese author, Nobel Prize for literature in 1998

II. Acknowledgements

Four and a half years ago I started a journey that is now coming to an end. The path was not always easy but it was, definitely, worth. From all the people that helped me in this journey there are those whose contribution I'll never forget.

The first is my supervisor, Dr Ritu Kataky. Thank you for your help, patience, guidance, understanding, etc. Thank you for everything! During these years you went far and beyond your duties as supervisor to make my journey as smooth as possible. THANK YOU

Paula, there are no words to express my gratitude towards you. You're not only the woman I love but also my best friend. We've shared so many things, personal and professionally, that our lives will always be connected. Your resilience inspires me! Amo-te tanto muito!

To my family! Dad and mum, you are the best people that I know and I'd be happy if you have just half the pride in me that I have in you! Pedro thanks for taking care of me when I was just a little brat and for being always there. Luz you are a great sister–in–law; you don't just "take care" of my brother but you have also given me the two best nephews that one could ask for! Thank you all!

The past and present members of the sensors group, created a friendly and warm environment to work. Thank you all.

My good friends, Dr. Francisco Aguiar, Dr. Alice Delcourt – Lançon, Dr. Ioana Pera, Rachael Daunton, Dr. João Pires and Dr. João Mendes, thank you all for putting up with me!

To the staff in the chemistry department of Durham University (specially: Jean, Tony, Elizabeth, Jeff, people in the glass, electrical and mechanical workshops) thank you for all your help during these years.

Professor Isabel Ferra and Professor Ana Carreira (Department of Chemistry, University of Beira Interior – Portugal) thank you for encouraging me come to England and for being so hard with me when I was just an undergrad!! Thank you!

Finally I would like to thank EPSRC for financial support.

To all of those that I am forgetting, sorry and thank you!

Rui Campos

III. Declaration

The research described in this thesis was undertaken in the Department of Chemistry of Durham University between October 2007 and March 2012. All work is my own, other than where stated otherwise. No part of this work has been submitted previously for a degree at this or any other university.

Aspects of chapters 4 and 5 are based on the following published work:

- Francisco A. Aguiar , Rui Campos , Changsheng Wang , Rukkiat Jitchati, Andrei S. Batsanov , Martin R. Bryce and Ritu Kataky, ***Phys. Chem. Chem. Phys.***, 2010, **12**, 14804-14811
- Rui Campos and Ritu Kataky, ***J. Phys. Chem. B***, 2012, **116**, 3909–3917

Statement of Copyright

Table of Contents

List of Symbols and Abbreviations

This list has some of the common symbols and abbreviations used throughout this work. It is not an exhaustive list, any other symbols or abbreviations will be defined as and when they occur in the text.

The usual unit is that commonly used in electrochemical measurements. If a different unit is used in a particular case this will be indicated in the text.

Symbol	Meaning	Usual Unit
A	Area	cm^2
a	Microelectrode radius	μm
C	Capacitance	F
C_{dl}	Double – layer capacitance	F
C_∞	Bulk concentration	mol dm^{-3}
C_0	Concentration at null time	mol dm^{-3}
D	Diffusion coefficient	$cm^2\ s^{-1}$
d	Length of the molecule that forms the monolayer/bilayer	Å
d_a	Average thickness of a film with defects	Å
d_0	Average thickness of a defect free film	Å
E	Electrode potential versus a reference	V

Symbol	Meaning	Usual Unit
E^0	Standard electrode potential	V
E_f	Formal potential	V
E_F	Fermi level	eV
E_p	Peak potential	V
E_{pa}	Anodic peak potential	V
E_{pc}	Cathodic peak potential	V
E_λ	Switching potential for cyclic voltammetry	V
e	Elementary charge	1.6022×10^{-19} C
e^-	Electron	
erf(x)	Error function of x	
erfc(x)	Error function complement of x	
F	Faraday constant	96485.4 C mol^{-1}
f	Frequency	s^{-1} or Hz
ΔG	Gibbs free energy change in a chemical process	kJ mol^{-1}
ΔG_s	Standard Gibbs free energy of solvation	kJ mol^{-1}
$\Delta G^‡$	Standard Gibbs free energy of activation	kJ mol^{-1}
$\Delta H^‡$	Standard enthalpy of activation	kJ mol^{-1}
i	Current	A
i_0	Current measured at bare electrode	A
J(x,t)	Flux at distance x and time t	mol cm^{-2} s^{-1}
K	Equilibrium constant	
k_B	Boltzmann constant	1.38099×10^{-23} J K^{-1}
k_f	Heterogeneous rate constant of forward (oxidation) reaction	cm s^{-1}

Symbol	Meaning	Usual Unit
k_b	Heterogeneous rate constant of backward (reduction) reaction	cm s^{-1}
k_0	Electron – transfer rate constant for bare electrode	cm s^{-1}
k_{app}	Apparent electron transfer rate constant	cm s^{-1}
k_{th}	Theoretical electron transfer rate constant	cm s^{-1}
n	Stoichiometric number of electrons involved in an electrode reaction	
O	Generic oxidised form of an electroactive specie	
Q	Charge	C
R	Generic reduced form of an electroactive specie	
	Molar gas constant	8.31451 J K^{-1} mol^{-1}
	Resistance	Ω
R_{ct}	Charge – transfer resistance	Ω
$\Delta S^{\ddagger}$	Standard entropy of activation	kJ mol^{-1} K^{-1}
T	Absolute temperature	K
t	Time	s
υ	Scan rate	V s^{-1}
x	Distance from the working electrode surface	cm
Z'	Real part of impedance	Ω
Z''	Imaginary (complex) part of impedance	Ω
Z_w	Warburg impedance	Ω
α	Transfer coefficient	
β	Electrode tunnelling coefficient	$Å^{-1}$
δ	Diffusion layer thickness	cm

Symbol	Meaning	Usual Unit
ε	Permittivity	C N^{-1} m^{-2}
ε_0	Vacuum permittivity	8.854E-12 C N^{-1} m^{-2}
η	Overpotential	V
	Viscosity of the solvent	Kg s^{-1} m^{-1}
θ_a	Fractional coverage of a film	
θ_i	Fractional coverage for defects with film thickness i	
μ	Chemical potential	J mol^{-1}
τ	Time period	s
ϕ	Phase angle	Rad
ω	Angular frequency	rad s^{-1}
γ	Growth or decay factor of the resistance	V^{-1}

Abbreviation	Meaning
BLM	Bilayer lipid membrane
CA	Chronoamperometry
CE	Counter electrode
CV	Cyclic voltammetry
DDT	1 – Dodecanethiol
DPPTE	1,2-dipalmitoyl-*sn*-glycero-phosphothioethanol (sodium salt)
DOPE(B)	1,2-dioleoyl-*sn*-glycero-3-phosphoethanolamine-N-(biotinyl) (sodium salt)
EggPC	L-α-phosphatidylcholine
EIS	Electrochemical impedance spectroscopy
HEPES	4-(2-Hydroxyethyl)piperazine-1-ethanesulfonic acid

Abbreviation	Meaning
HPT	1 – Heptanethiol
IHP	Inner Helmholtz plane
MB	Methylene blue
NHE	Normal hydrogen electrode
OCP	Open circuit potential
OHP	Outer Helmholtz plane
PBS	Phosphate buffer solution
RE	Reference electrode
SAM	Self – assembled monolayer
UV	Ultraviolet
WE	Working electrode
psBLM	Pore suspended bilayer lipid membrane
sBLM	Supported bilayer lipid membrane

VII. List of Illustrations

2. Electrochemistry **Page**

2. Electrochemistry

3. Experimental Methods

4. Self – Assembled Monolayers on Au(111) **Page**

4. Self – Assembled Monolayers on Au(111) **Page**

4. Self – Assembled Monolayers on Au(111) **Page**

5. Bilayer Lipid Membranes Modified with Bio – Electroactive Molecules

5. Bilayer Lipid Membranes Modified with Bio – Electroactive Molecules **Page**

5. Bilayer Lipid Membranes Modified with Bio – Electroactive Molecules **Page**

5. Bilayer Lipid Membranes Modified with Bio – Electroactive Molecules **Page**

5. Bilayer Lipid Membranes Modified with Bio – Electroactive Molecules **Page**

6. Bilayer Lipid Membranes Based on the Avidin – Biotin Interaction

6. Bilayer Lipid Membranes Based on the Avidin – Biotin Interaction **Page**

6. Bilayer Lipid Membranes Based on the Avidin – Biotin Interaction **Page**

Appendix

List of Tables

5. Bilayer Lipid Membranes Modified with Bio – Electroactive Molecules **Page**

6. Bilayer Lipid Membranes Based on the Avidin – Biotin Interaction

Appendix

Studies of Electron Transfer in Self – Assembled Monolayers and Bilayer Lipid Membranes

1. Introduction

The cell membrane is a remarkable entity. It is between 4 – 8 nm thick, it maintains the territorial integrity of a cell or organelle while regulating the flow of matter, information and energy between the interior and exterior environment.[1,2] The biological activities of membranes come from their remarkable physical properties; membranes are flexible, self-sealing and selectively permeable to polar solutes. Figure 1.1 shows a schematic representation of a cell membrane according to the currently accepted model. This model was proposed by Singer and Nicolson[3] in 1972 and it is known as the "fluid mosaic model".

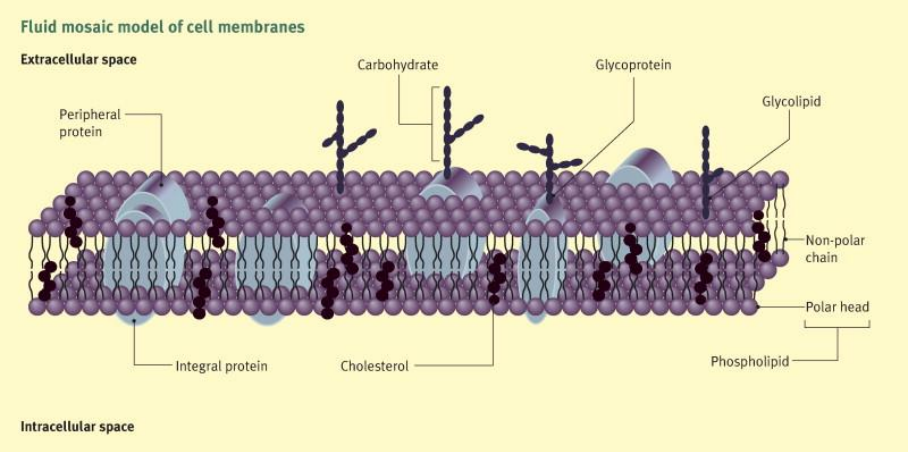

Figure 1.1 – Fluid mosaic model of cell membrane.[4] Reproduced from Ref. 4 with permission from Elsevier.

Because the cell membrane is such a complex structure, it is difficult to study individual functions. To avoid this complex structure, model membranes are widely used to mimic the cell membrane. They are made of the same basic components – the lipids, and then modified to fit the function that is object of study.[5]

Robert Hooke was, most likely, the first researcher to report black lipid membranes. This happened in 1672 while he was observing soap bubbles under, what would become the microscope.[6] Although this first report is more than three centuries old, it was not until 1962/63 that Rudin's group reported the BLM technique to lipid bilayer reconstitution.[7,8] Since then many studies have been done using bilayer lipid membranes (BLMs) as model for the cell membrane.

Several methods to produce bilayer lipid membranes have been developed over the years including solid – supported, tethered, suspended, polymer – cushioned or supported vesicular layers.[9]

Black lipid membranes are achieved by "painting" an organic solution of lipid in the septum that separates two aqueous solutions. When both chambers are filled, the bilayer is formed.[10,11] The formation of the BLM can be monitored by optical microscopy, when there is no BLM present the septum allows light to pass, when the BLM is formed the "hole" becomes black (hence the name black lipid membranes).[10,12,13] Techniques like Langmuir – Blodgett and black lipid membranes are widely used but they present problems of stability and reproducibility.[10,12]

To overcome the problems of free standing membranes, BLMs supported on polycarbonate fibers were developed by Mountz and Tien in 1978.[14] After this first report of supported bilayers others followed, being specially relevant those of Plant[15] and Florin[16] where the production of BLMs on metallic supports is reported – tethered bilayer lipid membranes (tBLMs).[17]

Tethered BLMs are more robust and stable than black lipid membranes and are deposited on a conductive substrate which makes their analysis/characterisation easier.[15] This type of bilayer is very good to study electron translocation across the lipid bilayer but has the

drawback of not being useful for the study of ion transfer; also this type of BLM is not ideal to mimic the environment for transmembrane proteins.[18]

To mimic the environment for transmembrane proteins, and its inherent complex nature, polymer cushioned phospholipid bilayers have been developed.[19] Using a polymer cushion, the membrane is not in direct contact with the surface but it still allows studies using surface techniques.[18]

The purpose of the research presented in this thesis was the characterisation, in terms of electron transfer, of the following mimics of the cell membrane: SAMs, BLMs (tethered, supported and cushioned) and BLMs modified with bioactive molecules. Each of the experimental chapters (chapters 4, 5 and 6) includes a detailed description of the type of BLM used; its advantages, disadvantages and main characteristics. The novelty of this work was the fact that the pore suspended membranes allow proteins inserted between intra and extra cellular fluids to be studied.

In chapter 2 the electrochemical principles and techniques used are discussed; this gives a good background of the concepts that were employed in the research presented in this thesis.

Chapter 3 includes the experimental details of each of the experimental chapters. Materials, instrumentation and detailed experimental information are given.

In chapter 4 the characterisation of four different SAMs is discussed. Two of the SAMs (HPT and DDT) are used as model system for the SAMs that involve thiolipids. SAMs of DPPTE and DPPTE+EggPC were made to evaluate which was better to serve as lower leaflet of tethered BLMs.

Chapter 5 is where the characterisation of two different types of BLM: pore suspended lipid membranes and tethered BLMs is made. After characterisation the BLMs were

modified with two bioactive molecules, ubiquinone 10 and α–tocopherol and also an equimolar mixture of these.

Cushioned BLMs were studied in chapter 6; these BLMs were made by depositing a layer of avidin in a Pt electrode and then, using a biotin modified lipid – DOPE(B), the BLMs are formed by applying voltage to the vesicles solution.

In the last chapter of this thesis general conclusions are presented and possible future directions of study are presented.

References

(1) von Heijne, G.; Rees, D. *Curr. Opin. Struct. Biol.* **2008**, *18*, 403–405.
(2) Lehninger, A.; Nelson, D.; Cox, M. *Lehninger Principles of Biochemistry*; 5th ed.; W. H. Freeman, 2008.
(3) Singer, S. J.; Nicolson, G. L. *Science* **1972**, *175*, 720–731.
(4) Christopher, F. *Surgery* **2007**, *25*, 401–406.
(5) Steinem, C.; Janshoff, A.; Ulrich, W.-P.; Sieber, M.; Galla, H.-J. *Biochim. Biophys. Acta, Biomembr.* **1996**, *1279*, 169–180.
(6) Tien, H. T.; Ottova, A. L. *J. Membr. Sci.* **2001**, *189*, 83–117.
(7) Mueller, P.; Rudin, D. O.; Tien, H. T.; Wescott, W. C. *Nature* **1962**, *194*, 979–980.
(8) Mueller, P.; Rudin, D. O.; Tien, H. T.; Wescott, W. C. *J. Phys. Chem.* **1963**, *67*, 534–535.
(9) Richter, R. P.; Berat, R.; Brisson, A. R. *Langmuir* **2006**, *22*, 3497–3505.
(10) Ries, R. S.; Choi, H.; Blunck, R.; Bezanilla, F.; Heath, J. R. *J. Phys. Chem. B* **2004**, *108*, 16040–16049.
(11) Wilburn, J. P.; Wright, D. W.; Cliffel, D. E. *Analyst* **2006**, *131*, 311–316.
(12) Tien, H. T. *J. Phys. Chem.* **1967**, *71*, 3395–3401.
(13) Van, N. T.; Tien, H. T. *J. Phys. Chem.* **1970**, *74*, 3559–3568.
(14) Mountz, J. M.; Tien, H. T. *Photochem. Photobiol.* **1978**, *28*, 395–400.
(15) Plant, A. L. *Langmuir* **1993**, *9*, 2764–2767.
(16) Florin, E. L.; Gaub, H. E. *Biophys. J.* **1993**, *64*, 375–383.
(17) Tien, H. T.; Ottova-Leitmannova, A. *Planar Lipid Bilayers (BLMs) and Their Applications*; 1st ed.; Elsevier Science, 2003.
(18) Castellana, E. T.; Cremer, P. S. *Surf. Sci. Rep.* **2006**, *61*, 429–444.
(19) Wong, J. Y.; Majewski, J.; Seitz, M.; Park, C. K.; Israelachvili, J. N.; Smith, G. S. *Biophys. J.* **1999**, *77*, 1445–1457.

2. Electrochemistry

From the origins of electrochemistry to the latest developments. This chapter will present electrochemistry as a fascinating field within the chemistry world. The most used techniques will be explained and discussed along with basic concepts and very important know how. Electrochemical impedance spectroscopy (EIS) is presented as a very powerful tool that enables a better characterisation of the system under study. Although EIS is a very sensitive technique, it cannot give all the answers; it is a complementary technique and other methods should be used to clarify the interfacial processes.

2.1. Origins of Electrochemistry

Electrochemistry was "born" when, in the beginning of the nineteenth century, Alessandro Volta (Figure 2.1) presented his results to the Royal Society of London. The results presented by Volta described the first electrochemical cell – "Voltaic Piles".[1]

Then in the 1830s, Michael Faraday (Figure 2.2) did the first quantitative studies of electrolysis and used, for the first time, the nomenclature that is used nowadays. Faraday is responsible for many words used daily in the electrochemistry world including 'electrode', 'cathode' and 'ion'.[2]

Figure 2.1 – Alexandro Volta. Image supplied by, and reproduced with permission from, the National Portrait Gallery, London (www.npg.org.uk).

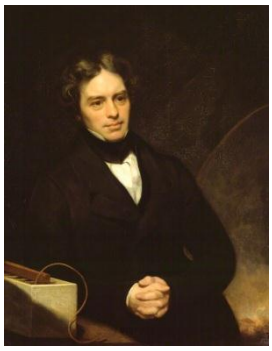

Figure 2.2 – Michael Faraday, one of the 'fathers' of electrochemistry. Image supplied by, and reproduced with permission from, the National Portrait Gallery, London (www.npg.org.uk).

Electrochemistry is the branch of chemistry that studies the interaction between electricity and chemical effects. It is a large and important area of physical chemistry. It is, however, difficult to define precisely the limits of this area, not simply on account of its size but also because of its influence in so many areas in chemistry as well in biology and physics.[2,3]

2.2. Fundamentals of Electrochemistry

Electrochemistry involves chemical phenomenon associated with charge transfer (either ions or electrons). The redox reactions involve the transfer of electrons between two species. If this transfer occurs in solution the reaction is homogeneous, if the transfer is on the electrode surface the reaction is heterogeneous. When these transfers occur, two (one

in each direction) or more charge transfers at opposite directions must happen to ensure electroneutrality.[4]

The amount of chemical change produced is proportional to the total amount of electrical charge passed through the cell – Faraday's law. The current that is generated from this type of reaction is called Faradaic current.[3,4]

The redox reactions are so called because one of the species involved is reduced and the other is oxidized. The one that loses electrons is said to be oxidized (reduction reaction) and the one that gains electrons is said to be reduced (oxidation reaction). If these reactions occur spontaneously the electrochemical cell is called galvanic (figure 2.3a). On the other hand, if an external supply of electrical energy is required to make these reactions occur the electrochemical cell is called electrolytic (figure 2.3b).[3,4]

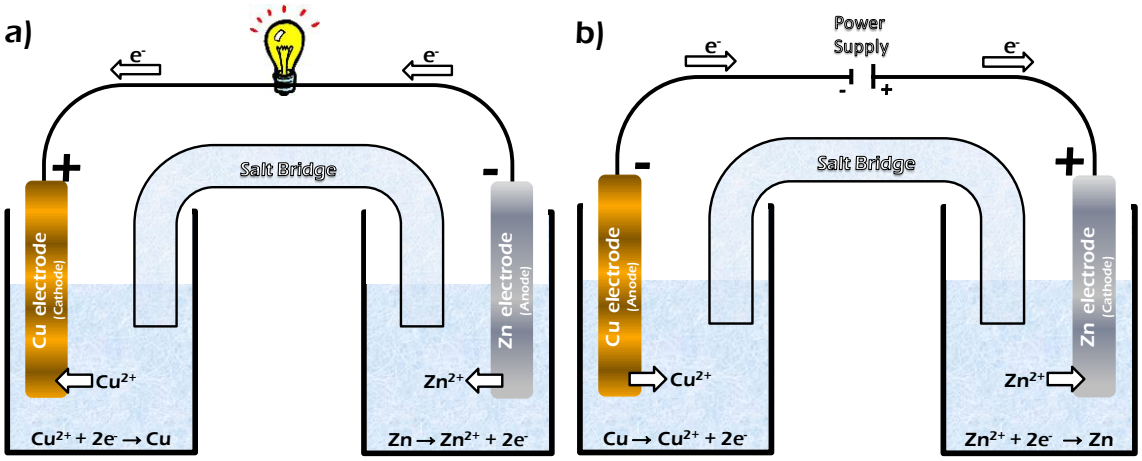

Figure 2.3 – Schematic diagram of a) Galvanic and b) electrolytic cells.

2.3. Electrodes

Different types of electrodes are used in electrochemistry and electroanalysis. The general case consists of a three electrode set-up, figure 2.4.[3,5] This set-up encompasses an electrode where the process occurs – **working or indicator electrode**, an electrode which

controls the potential of the working electrode – **reference electrode**, and also an electrode in which the current flows – **counter or auxiliary electrode**.

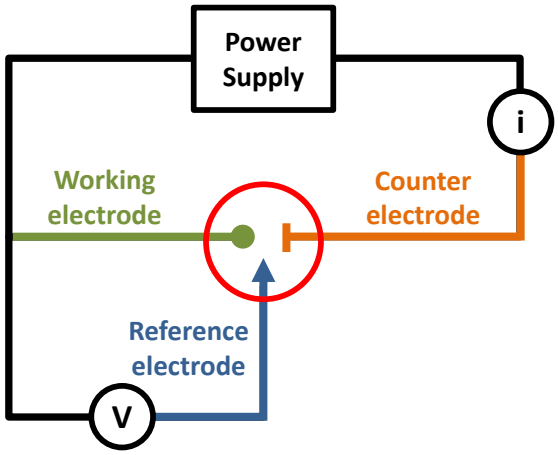

Figure 2.4 – Schematic representation of a three electrode electrochemical cell.

2.3.1. Working Electrode

The most basic definition of working electrode is that this is the electrode where the reactions under study take place. It can be made of several materials, and thus its material should be chosen taking into account different parameters: the redox behaviour of the analyte in solution, the background current over the potential region required for the experiments, electrical conductivity, surface reproducibility, mechanical properties, cost, availability and toxicity.[3,4,6] Figure 2.5 shows the potential range of various working electrodes in aqueous solutions.[3]

The most popular materials used in working electrodes are mercury, carbon and noble metals (gold, platinum and silver).

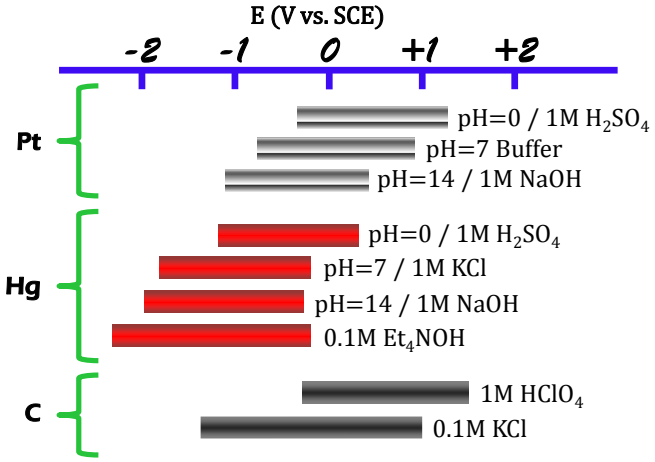

Figure 2.5 – Potential range of various working electrodes in aqueous solutions.[3]

2.3.1.1. Metal Electrodes

Metal electrodes are amongst the most used electrodes in electrochemistry and electroanalysis. This group of electrodes includes mercury electrodes and solid electrodes. Each of these has its advantages and disadvantages, *e.g.*, mercury electrodes present a high hydrogen overvoltage, resulting in an extended cathodic potential window, but have a lower anodic potential window when compared to solid electrodes.[7,8]

Mercury electrodes are now less used mainly due to mercury toxicity and they have been being replaced by solid electrodes. Platinum and gold are widely used and they offer favourable electron transfer kinetics, high conductivity with low background currents and a large anodic potential window.

2.3.1.2. Carbon Electrodes

Carbon electrodes exist in many types and configurations. Glassy carbon, carbon fibres, carbon black, graphite, carbon paste nanotube and boron doped diamond are used as electrodes. Generally carbon electrodes present a good cathodic potential range but have quality problems and they are hard to shape.[8]

Because the kinetics of electron transfer depends on the electrode surface electrochemical reactions, in most cases, are slower at the carbon electrodes than at metal electrodes.

2.3.2. Reference Electrode

The potential that is applied to the working electrode is measured against the reference electrode, *i.e.*, the reference electrode provides a stable and reproducible potential in a wide range of solutions against which the potential of the working electrode is applied.[9]

The accepted convention for reference electrodes is that, under standard conditions, the standard hydrogen electrode has a potential of zero at all temperatures; the potential of all the other reference electrodes is reported in reference to the standard hydrogen electrode.[9–12]

Properties like the simple manufacture, convenience on a day-to-day basis and high temperature range make the silver – silver/chloride electrode (Ag/AgCl) the most used reference electrode in aqueous solutions.[11]

The Ag/AgCl electrode, figure 2.6, is composed of a silver wire that is oxidised in the presence of chloride ions; an insoluble film of silver chloride is formed on the surface of the metal. When this electrode is immersed in solution of chloride ions, a potential is established according with the following half – cell reaction

$$AgCl_{(aq)} + e^{-} \leftrightarrow Ag_{(s)} + Cl^{-}_{(aq)}$$

The standard potential of an Ag/AgCl reference electrode is measured *vs.* the standard hydrogen electrode using the cell

$$Pt\left|H_{2(g,\ p=1bar)}\right|HCl_{(aq,\ a=1M)}\left|AgCl_{(s)}\right|Ag_{(s)} \qquad E_{cell} = +0.223V$$

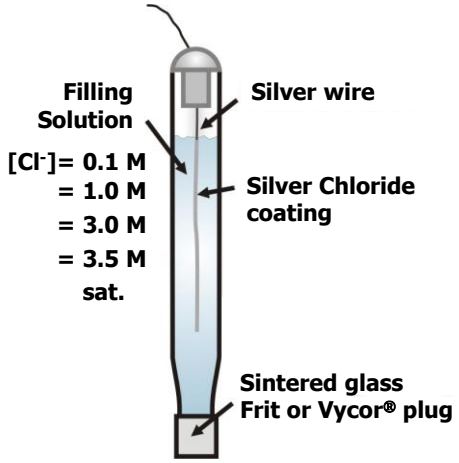

Figure 2.6 – Schematic representation of an Ag/AgCl reference electrode.

The filling solution of an Ag/AgCl reference electrode can have different concentrations; the Nernst equation is used to predict the potential at different concentrations:

$$E^{Cl^-/AgCl/Ag} = E^{0,Cl^-/AgCl/Ag} - \frac{RT}{F}\ln(a_{Cl^-}) \qquad (2.1)$$

Table 2.1 – Standard electrode potential for Ag/AgCl electrode at different concentrations of Cl^-.

Conditions	E^0 *vs.* NHE (V)
$a_{Cl^-} = 1M$	+0.223
KCl (0.1M)	+0.289
KCl (1M)	+0.237
KCl (3M)	+0.209
KCl (3.5M)	+0.205
KCl (sat.)	+0.199

One of the characteristics of a reference electrode is that its potential should be stable through the all experiment; the reference electrode should be non-polarisable (its potential should not change with the flow of current). When there is current flow in the

electrochemical cell, the interfacial potential varies as the current passes through the cell. To avoid polarisation of the reference electrode a third electrode is added to the system: the counter electrode.

2.3.3. Counter Electrode

The counter electrode is chosen not to interfere with the reaction. It exists to ensure that current does not flow through the reference electrode and usually has a surface area much larger than that of the working electrode to ensure that the reactions occurring in the working electrode are not limited by the surface area of the counter electrode.[9]

2.4. Electrochemical Double Layer

The electrode reactions occur in the interface between the electrode and the solution. Both the thermodynamic driving force and how the reactions take place depend on the structure of the interfacial region. This interfacial region was first described by Helmholtz in 1879[13,14] and since has been known as double – layer.[4]

Helmholtz model considered that both the positive and negative charges were sorted in a rigid way on both sides of the interface, as shown in figure 2.7.

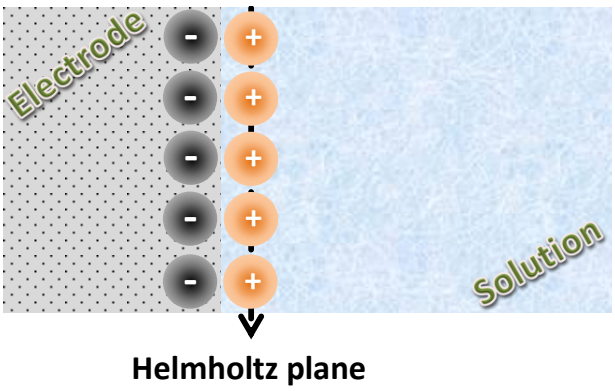

Figure 2.7 – The Helmholtz model of the electrical double layer.

This model can be compared to the classical parallel – plate capacitor problem. One plate is on the surface of the electrode and the other is on the centre of the ions, forming the Helmholtz plane.

Realising that both the applied potential and the electrolyte concentration would have influence on the value of the double layer capacity, Gouy[15] and Chapman[16], independently, developed a double layer model in which the double layer has variable thickness due to the movement of the ions – *diffuse double layer*. In this model the ions are seen as being infinitely small and can get infinitely close to the electrode.[3,4]

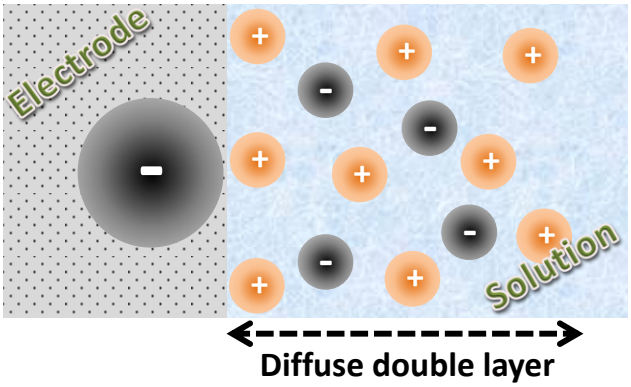

Figure 2.8 – The Gouy – Chapman model of the electrical double layer.

The Gouy – Chapman model was further developed by Stern.[17] Stern incorporated the Helmholtz and the Gouy – Chapman model in a single model, meaning that the double layer would be formed by a compact layer of ions close to the electrode surface (which was named outer Helmholtz plane – OHP) followed by a diffuse layer in the bulk solution.[3,4]

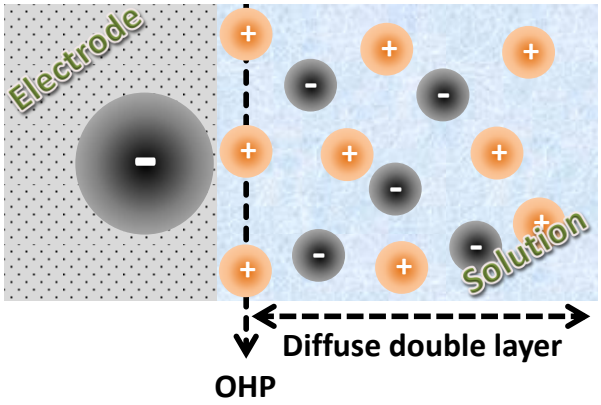

Figure 2.9 – The Stern model of the electrical double layer.

In 1947 Grahame[18] introduced the inner Helmholtz plane (IHP) to the Stern model. The inner Helmholtz plane passes through the ions that are adsorbed to the electrode surface, while the outer Helmholtz plane goes through the centre of the solvated and non – specifically adsorbed ions, figure 2.10.

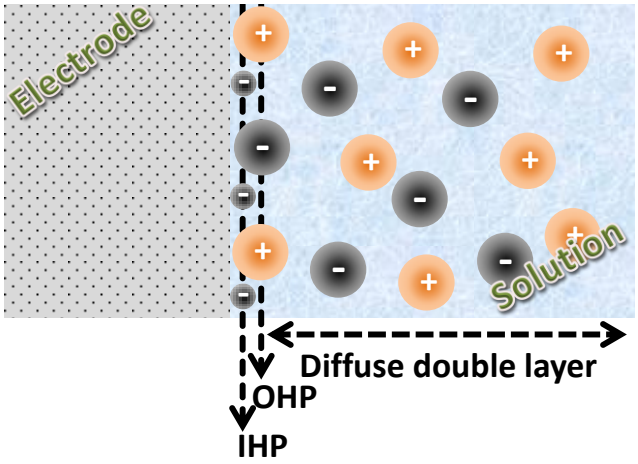

Figure 2.10 – The Grahame model of the electrical double layer.

The model that is currently accepted was developed by Bockris, Devanathan and Muller[19] and has taken into account the influence of the solvent molecules near the interface. Due to the electrode charge, the dipoles of these molecules would have a fixed alignment, figure 2.11.[3,4,20]

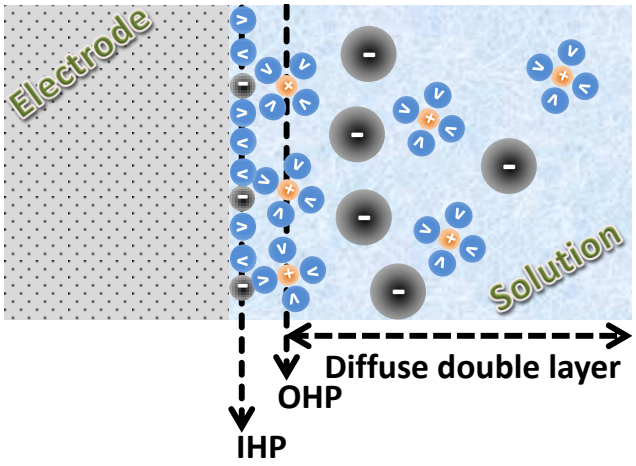

Figure 2.11 – The Bockris, Devanathan and Muller model of the electrical double layer.

2.5. Kinetics and Mechanism of Electrode Reactions

2.5.1. Transport Processes

The rate of electrode reactions is determined by the slowest step in the series of steps that take place. A simple reaction involves mass transport of the reactant from the bulk solution to the electrode surface, here occurs the electron transfer and then the product diffuses to the bulk solution (again mass transport). More complex reactions might involve other processes such as protonations, branching mechanisms or modification of the electrode surface.[3,4,10] Figure 2.12 shows a schematic representation of a general electrode reaction.

In step 1 the reactants reach the electrode surface, here several steps occur. Step 2 refers to the rearrangement of the ionic atmosphere, the reorientation of the solvent dipoles is step 3, and in step 4 there is alteration in the distances between the central ion and the ligands. Following these steps, the electron transfer takes place – step 5. Then there is relaxation and diffusion of the products to the bulk solution – step 6.[4]

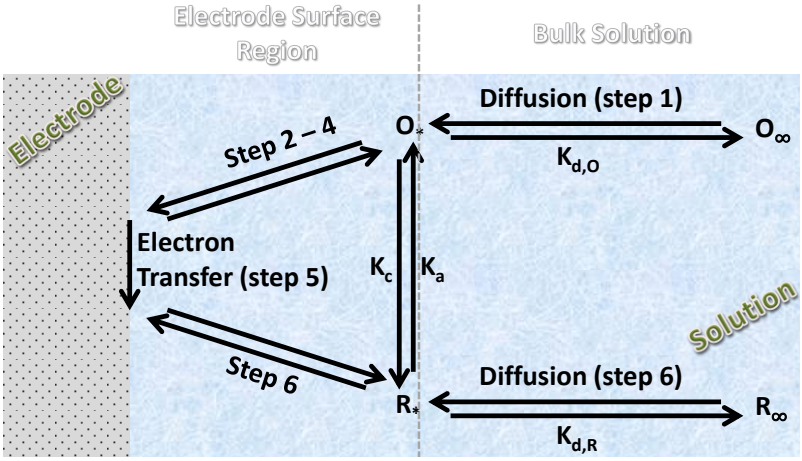

Figure 2.12 – Schematic representation of electron transfer at the electrode surface.

2.5.2. Rate of Electrode Reactions

The rate constant, k, is related with the activation enthalpy, $\Delta H^{\ddagger}$, by the Arrhenius expression,

$$k = A \exp\left[\frac{-\Delta H^{\ddagger}}{RT}\right] \qquad (2.2)$$

where A is the pre – exponential factor and can be expressed in terms of activation entropy, $\Delta S^{\ddagger}$,

$$A = A' \exp\left[\frac{\Delta S^{\ddagger}}{RT}\right] \qquad (2.3)$$

leading to,

$$k = A' \exp\left[\frac{-\left(\Delta H^{\ddagger} - T\,\Delta S^{\ddagger}\right)}{RT}\right] = A' \exp\left[\frac{-\Delta G^{\ddagger}}{RT}\right] \qquad (2.4)$$

The potential applied to the electrode is reflected on $\Delta G^{\ddagger}$ values. Considering a half reaction of the first order

$$O + ne^{-} \leftrightharpoons R$$

The couple O|R has an associated E_{Redox}, shown in figure 2.13. When a potential is applied to the electrode, it changes the highest level of electronic energy facilitating the reduction or oxidation processes. That level is the Fermi level, E_{Fermi}, and electrons are always transferred from and to this level. E_{Redox} is fixed and by altering the potential that is applied to the electrode (and by consequence E_{Fermi}), the electrode either supplies electrons to O – reduction, or removes electrons from R – oxidation. [3,4,20,21]

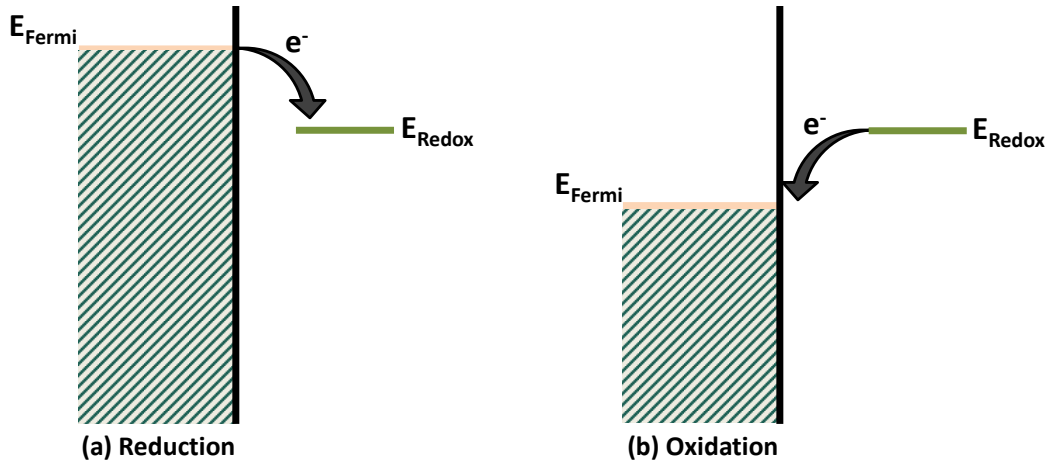

Figure 2.13 – Electron transfer in an inert metal electrode. E_{Fermi} is altered by the applied potential facilitating either the (a) reduction or the (b) oxidation processes.

The energy profile describing this process is shown on figure 2.14. Parabolic energy profiles are used to describe the energy of both reactants and products. The most important part is the intersection of both profiles; in this region the energy variation is almost linear.[4,22]

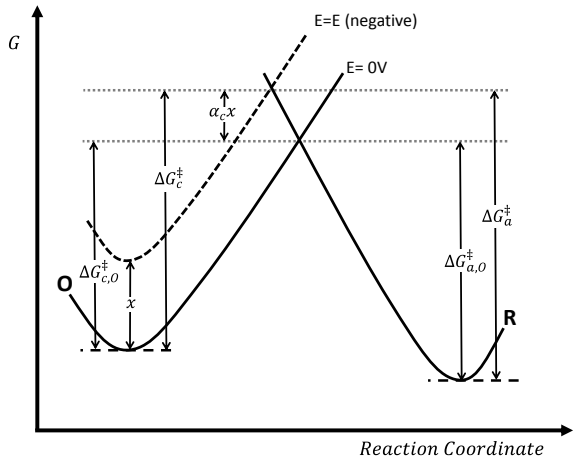

Figure 2.14 – Effect of a change in the applied potential on the reduction of O to R (considering that R is not present in the bulk solution or in the electrode material).

A change x in the free energy of O results in a change $\alpha_c x$ in the activation energy; so for a reduction

$$\Delta G_c^{\ddagger} = \Delta G_{c,0}^{\ddagger} + \alpha_c nFE \qquad (2.5)$$

and for an oxidation

$$\Delta G_a^{\ddagger} = \Delta G_{a,0}^{\ddagger} - \alpha_a nFE \qquad (2.6)$$

where:

E – Potential applied to the electrode

α – measure of the slope of the energy profiles.

α presents values between 0 and 1, being around 0.5 for metals. α=0.5 means that the activated complex is exactly halfway between the reactants and the products on the reaction coordinate.[3,4]

Substituting $\Delta G^{\ddagger}$ in equation (2.4) by equations (2.5) and (2.6), yields

$$k_c = A' \exp\left[\frac{-\Delta G_{c,0}^{\ddagger}}{RT}\right] \exp\left[\frac{-\alpha_c nFE}{RT}\right] \qquad (2.7)$$

for a reduction, and for an oxidation yields,

$$k_a = A' \exp\left[\frac{-\Delta G_{a,0}^{\ddagger}}{RT}\right] \exp\left[\frac{\alpha_a nFE}{RT}\right] \qquad (2.8)$$

Equations (2.7) and (2.8) can be rearranged leading to,

$$k_c = k_{c,0} \exp\left[\frac{-\alpha_c nFE}{RT}\right] \qquad (2.9)$$

and

$$k_a = k_{a,0} \exp\left[\frac{\alpha_a nFE}{RT}\right] \qquad (2.10)$$

As said before the reaction is first order, so at equilibrium

$$k_c[O]_* = k_a[R]_* \qquad (2.11)$$

where the subscript $*$ means close to the electrode.[4]

If

$$[O]_* = [R]_* \qquad (2.12)$$

and

$$k_{c,0} = k_{a,0} = k_0 \qquad (2.13)$$

where k_0 is the standard rate constant. With E_f being the formal potential, replacing $k_{c,0}$ and $k_{a,0}$ in equations (2.9) and (2.10) by equation (2.13) leads to

$$k_c = k_0 \exp\left[\frac{-\alpha_c nF\left(E - E_f\right)}{RT}\right] \qquad (2.14)$$

$$k_a = k_0 \exp\left[\frac{\alpha_a nF(E - E_f)}{RT}\right] \qquad (2.15)$$

This electrode kinetics formulation was first developed by Butler[23,24] and Volmer[25].[3,4] The current is proportional to the difference between the reduction and oxidation rates and is given by,

$$i = nFA(k_a[R]_* - k_c[O]_*) \qquad (2.16)$$

with A being the area of the working electrode.[3,4]

As previously mentioned the activation barrier for metals, figure 2.14, is halfway between the reactants and the products (α≈0.5). In less usual cases the activated complex structure is more towards the oxidised or reduced species and gives rise to values of α close to 0 or 1, respectively, as shown in figure 2.15.[3,4]

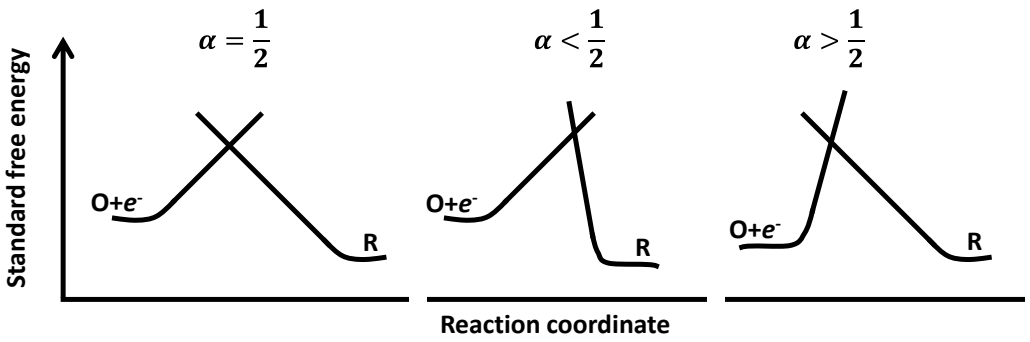

Figure 2.15 – The transfer coefficient (α) has a value between 0 and 1 indicating the symmetry of the barrier to reaction.[3,4]

Replacing k_c and k_a by equations (2.14) and (2.15), respectively, equation (2.16) can now be written as,

$$i = nFAk_0\left[[O]_* exp\left(\frac{-\alpha nF(E - E_f)}{RT}\right) - [R]_* exp\left(\frac{(1-\alpha)nF(E - E_f)}{RT}\right)\right] \qquad (2.17)$$

This is the Butler – Volmer equation, which is the fundamental relationship between the voltage applied and the current generated in an electrochemical cell.[3,4,21]

In equilibrium both rate constants are identical and the current in the cathode and anode are also equal, hence equation (2.17) can be rewritten as

$$nFAk_0[O]_* exp\left(-\alpha nf\left(E - E_f\right)\right) = nFAk_0[R]_* exp\left((1-\alpha)nf\left(E - E_f\right)\right) \qquad (2.18)$$

with f = $\frac{F}{RT}$.

Also in equilibrium, $[O] = [R] = C$, therefore the net current flow would be zero. Although, the balanced Faradaic activity can still be visualised as the exchange current, i_0. This current can be related to k_0

$$i_0 = nAFk_0C_* \qquad (2.19)$$

The Butler – Volmer equation simplifies to

$$i = i_0\left[exp\left(-\alpha nf\left(E - E_f\right)\right) - exp\left((1-\alpha)nf\left(E - E_f\right)\right)\right] \qquad (2.20)$$

Equation (2.20) is known as the current – overpotential equation. This means that is possible to investigate the kinetics of reactions with different i_0. The bigger i_0, the bigger the net current change will be on the variation of the overpotential $\left(\eta = E - E_f\right)$ and quicker the kinetics of the reaction.[3,21]

At high overpotentials the Butler – Volmer equation simplifies to the Tafel equation

$$\eta = \frac{1}{\alpha nf} ln(i_0) - \frac{1}{\alpha nf}\ln(i) \qquad (2.21)$$

Linearising,

$$\eta = a + b\ log(i) \qquad (2.22)$$

Where a is the intercept and b is the slope of the line in a plot of log I *vs.* η, figure 2.16. This plot is known as Tafel plot.

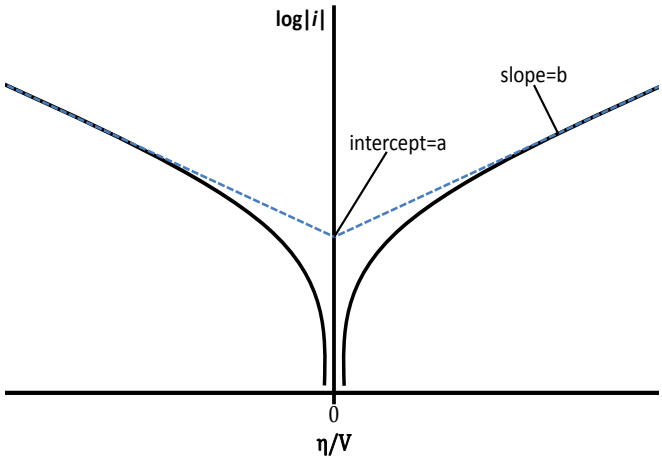

Figure 2.16 – Tafel plot for anodic and cathodic branches of the current – overpotential curve for $O + ne^- \rightleftharpoons R$ with α=0.5.[3]

2.5.3. Microscopic Theories of Electron Transfer

The heterogeneous electron transfer kinetics discussed, so far, is based on macroscopic concepts; the rate of reaction was expressed in terms of the phenomenological parameters k_0 and α. This kind of approach is very useful but it does not take into account the nature and structure of the reacting species, the solvent, the electrode material and adsorbed layers on the electrode. To obtain such information, a microscopic theory that describes how molecular structure and environment affect the electron transfer process.[3]

Major contributions to this area have been made by Libby[26], Marcus[27,28], Hush[29,30], Levich[31] and Dogonadze[32] among others.

One of the first concepts that has to be clear in order to look at the microscopic model, is the concept of inner and outer sphere electron transfer. This concept was introduced by Taube *et al.* in 1953 regarding the redox reactions of coordination complexes in solution.[33] Outer sphere were reactions between two species in which the coordination

spheres are maintained in the activated complex; in the inner sphere mechanism the ions share a ligand in an activated complex and the reaction occurs in that activated complex.[3,33]

This concept can also be applied to electrode reactions and in that case an outer sphere reaction refers to a reaction where the interaction between donor and acceptor is not strong, if any at all. The electrons can hop through space from the donor to the acceptor; Weaver and Anson[34] located the reactant centre or ion in the outer Helmholtz plane, figure 2.17 a). In the inner sphere electrode reaction the interaction between the donor and acceptor is very strong; this type of reaction involves adsorption on the electrode surface, if the adsorption is transitory the event of electron transfer is called intermolecular electron transfer, figure 2.17 b).[3,35]

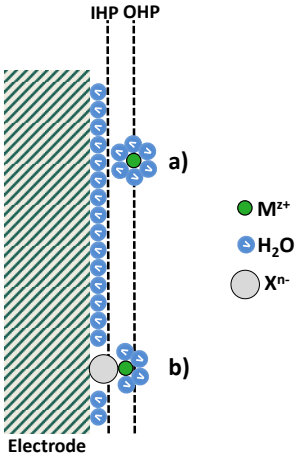

Figure 2.17 – Schematic representation for a) outer sphere and b) inner sphere redox reaction mechanism.

2.5.3.1. Marcus Microscopic Model

Marcus theory[36] was developed, initially for homogeneous systems, for outer sphere electron transfer mechanism but was later extended to inner sphere electron transfer mechanism by Hush[37].

As shown before the activation barrier can be represented by a parabola. The energy difference between reactants and products is represented by ΔG, figure 2.18, ΔG_s describes the solvation change and the reorganization between reactants and products and $\Delta G^{\ddagger}$ is the activation energy.[3,4,22,36,38] The intersection of the two parabolas yields*,

$$\Delta G^{\ddagger} = \frac{(\Delta G + \Delta G_s)^2}{4\Delta G_s} \qquad (2.23)$$

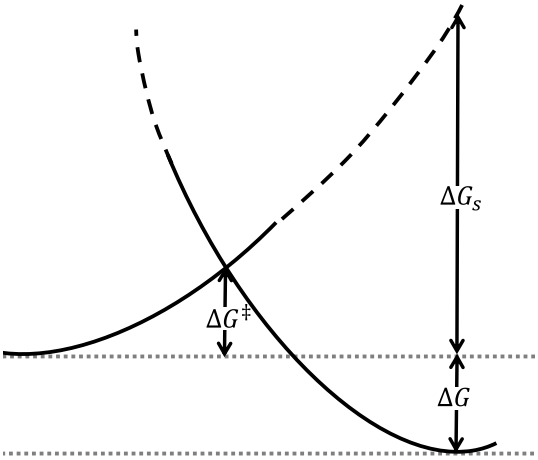

Figure 2.18 – Representation of reaction coordinate showing that the activation barrier is mainly due to solvent reorganisation.

The charge transfer coefficient, α, is given by

$$\alpha = \frac{RT}{F}\left|\frac{\partial \ln k}{\partial E}\right| = \frac{\partial \Delta G^{\ddagger}}{\partial E} \qquad (2.24)$$

Substituting $\Delta G^{\ddagger}$ in equation (2.24) by equation (2.23),

$$\alpha = -\frac{1}{2F}\left(1 + \frac{\Delta G}{\Delta G_s}\right)\frac{\partial \Delta G}{\partial E} = \frac{1}{2}\left(1 + \frac{\Delta G}{\Delta G_s}\right) \qquad (2.25)$$

In most of the cases $\Delta G_s \gg \Delta G$, this means that the kinetics is slow and $\alpha \approx \frac{1}{2}$; this provides a good link between the Marcus theory and the Butler – Volmer kinetics.[4,22]

* For geometrical derivation of Marcus theory see Appendix A1.

Equation (2.25) predicts that α changes with potential, the energy parabola in figure 2.14 move relative to one another as the electrode potential changes because the Gibbs energy of the electron in the metal energy changes.[22] For $E \sim E_f$, where $\Delta G \approx 0, \alpha \approx \frac{1}{2}$; when $\Delta G \gg 0$ and the reaction is thermodynamically difficult $\Delta G_s \approx \Delta G$ and $\alpha \to 1$. On the other extreme if $\Delta G \ll 0$ then $\Delta G_s \approx -\Delta G$ and $\alpha \to 0$.[3,4,22]

- ***Adiabatic and Non – Adiabatic Reactions***

For electron transfer to occur an overlap between the populated orbital of the donor and the empty orbital of the acceptor is necessary in the activated complex. In that overlap there is a quantum mechanical splitting between the two surfaces – the energy gap is a resonance energy. When that splitting is large, figure 2.19 a), there is a significant perturbation of the isolated R and P curves and the reaction from R to P occurs along the lower curve with a probability close to the unity – this type of reaction is adiabatic.[3,22] When the resonance energy is small, there is only a small perturbation on the potential energy curves of R and P; this leads to a non – adiabatic process and the probability of transfer of R to P is much smaller than unity.[3,22]

In most electron transfer reactions the resonance energy is small (in the order of a few kilojoules per mole or less), this is enough to ensure that the reaction is adiabatic but not enough to significantly alter the potential energy curves of R and P. Thus, the following expression can be written for the electrochemical rate constant,

$$k = KZe^{-\frac{\Delta G^{\ddagger}}{RT}} \qquad (2.26)$$

K – Transition probability (K~1 for adiabatic process and $K \ll 1$ for non – adiabatic process),

Z – pre – exponential term

$\Delta G^{\ddagger}$ – activation energy.[22]

The activation energy can be calculated with accuracy (equation (2.23)) as long as the R and P potential energy curves are known.

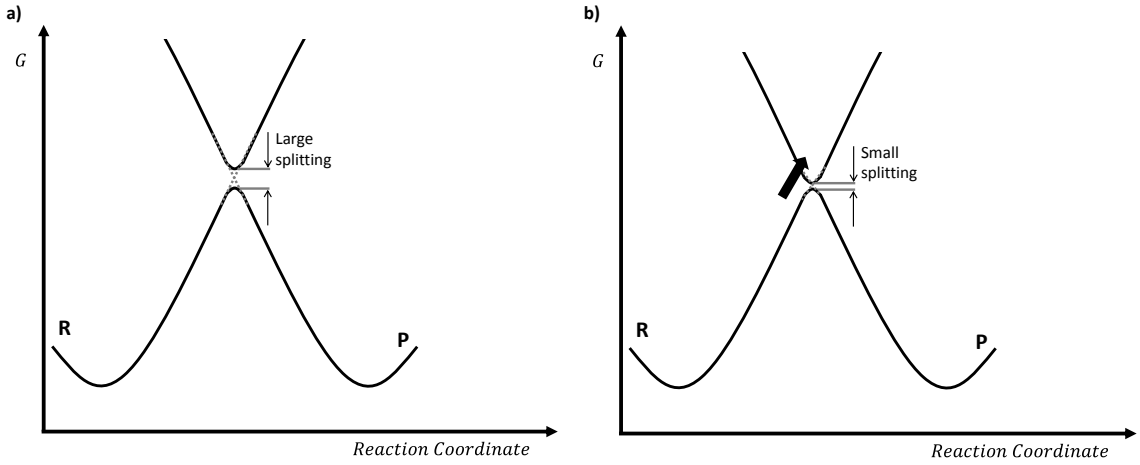

Figure 2.19 – Splitting of the energy curves in the intersection region. a) strong interaction between R and the electrode leads to a well-defined continuous curve connecting R with P. b) weak interaction between R and the electrode leads to a small splitting; when the system reaches the transition state it has a tendency to stay on the R curve, has indicated by the arrow. The probability of crossing to the P curve is small.[3,22]

2.6. Mass Transport Controlled Reactions

When the reaction is controlled by the mass transport it is said to be a nernstian or reversible reaction.[3,4] For this type of reactions the rate is determined by the flux (J) at which the electroactive specie is brought to the electrode surface by mass transport. The process of mass transport in the electrode/solution interface can occur due to convection, migration or diffusion.

In convection the movement is due to mechanical forces such as gas bubbling, pumping or stirring. It can also be due to thermal and/or density gradients within the solution. Migration is the movement of charged species due to an electric field, it is purely electrostatic. Diffusion is the movement of species due to a concentration gradient.[3,4,21]

The flux of species to the electrode is described mathematically by the Nernst – Plank equation, which simplified just for one dimension (along the x – axis) takes the following form

$$J(x,t) = \underbrace{-D\frac{\partial C(x,t)}{\partial x}}_{Diffusion} \underbrace{-\frac{ZFDC_{\infty}}{RT}\frac{\partial E(x,t)}{\partial x}}_{Migration} \underbrace{+C(x,t)V(x,t)}_{Convection} \qquad (2.27)$$

Where:

J(x, t) – Flux (mol cm^{-2} s^{-1})

D – Diffusion coefficient (cm^2 s^{-1})

$\frac{\partial C(x,t)}{\partial x}$ – Concentration gradient (at distance x and time t)

Z – Charge of the electroactive species

F – Faraday constant (C mol^{-1})

C_{∞} – Bulk concentration of the electroactive species (mol cm^{-3})

R – Gas constant (J mol^{-1} K^{-1})

T – Temperature (K)

$\frac{\partial E(x,t)}{\partial x}$ – Potential gradient (at distance x and time t)

V(x, t) – Hydrodynamic velocity.

Equation (2.27) encompasses all the three modes of mass transport, this makes it very complex and difficult to handle. However, some of the processes of mass transport can be minimised to the point that they can be neglected. Migration can be suppressed by adding a large excess of background electrolyte (when compared to the concentration of the

electroactive specie); convection can be minimised by using a quiescent solution. Under these conditions the mass transport is limited only by diffusion. This gives rise to Fick's first law; there is a concentration gradient in the electrode surface (within the electrical double layer) generated by the reaction occurring at the electrode surface. Fick's first law is express by the first term of equation (2.27),

$$J(x,t) = -D\frac{\partial C(x,t)}{\partial x} \qquad (2.28)$$

It is known that the current (i) is directly proportional to the flux and surface area (A),

$$i = -nFAJ \qquad (2.29)$$

The combination of equations (2.28) and (2.29) gives the general expression for the current response

$$i = nFDA\frac{\partial C(x,t)}{\partial x} \qquad (2.30)$$

The variation of concentration with time due to diffusion is described by Fick's second law,

$$\frac{\partial C(x,t)}{\partial t} = D\frac{\partial^2 C(x,t)}{\partial x^2} \qquad (2.31)$$

Independently of the coordinate system, Fick's second law has the following general form,

$$\frac{\partial C}{\partial t} = D\nabla^2 C \qquad (2.32)$$

where ∇ is the Laplace operator and it is different for each coordinate system as shown in table 2.2.

Table 2.2 – Fick's second law for Cartesian and spherical coordinates.

Coordinates	Laplace Operator	Fick's 2nd Law
Cartesian		
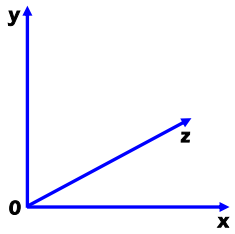	**One direction (x – axis)** $\nabla = \frac{\partial}{\partial x}$	$\frac{\partial C}{\partial t} = D\frac{\partial^2 C}{\partial x^2}$
	Three directions $\nabla = \frac{\partial}{\partial x} + \frac{\partial}{\partial y} + \frac{\partial}{\partial z}$	$\frac{\partial C}{\partial t} = D\left(\frac{\partial^2 C}{\partial x^2} + \frac{\partial^2 C}{\partial y^2} + \frac{\partial^2 C}{\partial z^2}\right)$
Spherical		
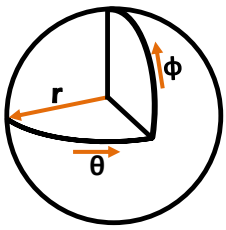	$\nabla = \frac{\partial}{\partial r} + \frac{1}{r}\frac{\partial}{\partial \theta} + \frac{1}{r\sin\theta}\frac{\partial}{\partial \phi}$	$\frac{\partial C}{\partial t} = D\left(\frac{\partial^2 C}{\partial r^2} + \frac{2}{r}\frac{\partial C}{\partial r}\right)$

Fick's laws describe the flux and the concentration of the electroactive specie as a function of position and time. The solution of Fick's second law gives the variation of flux, and consequently the diffusion limited current, but to solve there is the need to impose some boundaries.

The determination of the diffusion – limited current, I_d, is made using a step potential technique - chronoamperometry. The potential is changed, in a step manner, from a potential where no reaction of interest occurs to a potential where all electroactive species that reach the electrode surface react (figure 2.20). The current produced is plotted as a function of time.

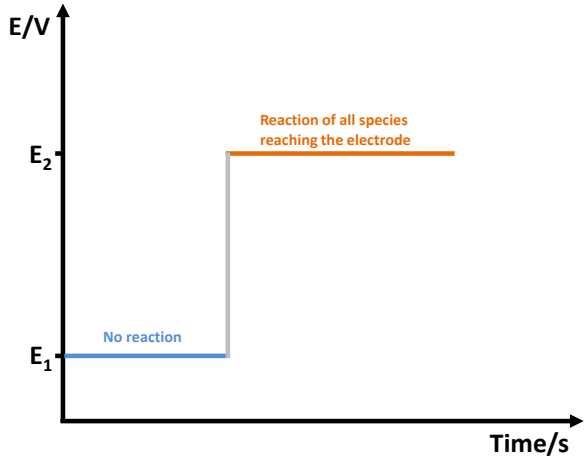

Figure 2.20 – Potential step to obtain diffusion – limited current of the electroactive species.

2.6.1. Diffusion at Planar Electrodes

For planar electrodes, Fick's second law is equation (2.31). The boundaries necessary to solve equation (2.31) are:

$t=0s \Longrightarrow C_0=C_\infty$ — When there is no electrode reaction, there is no concentration gradient.

$t\geq 0s \Longrightarrow \lim_{x\to\infty} C = C_\infty$ — At large distances from the electrode surface there is no variation in concentration.

$\left.\begin{matrix} t > 0 \\ x = 0 \end{matrix}\right\} \Longrightarrow C_0 = 0$ — There is no concentration of electroactive specie in the electrode surface.

with C_0 being the concentration at the electrode and C_∞ the concentration in the bulk solution.[3,4]

The diffusion – limited equation is obtained by using the Laplace transform[†] and the boundary conditions. It takes the following form,

[†] Most common Laplace transforms are presented in Appendix A2

$$I_d(t) = \frac{nFAD^{1/2}C_\infty}{(\pi t)^{1/2}} \qquad (2.33)$$

where n is the number of electrons involved and t the reaction time (s). All the other parameters have the same meaning as before.

Equation (2.33) is known as Cottrell equation. From this equation is observable that the current decreases with time,

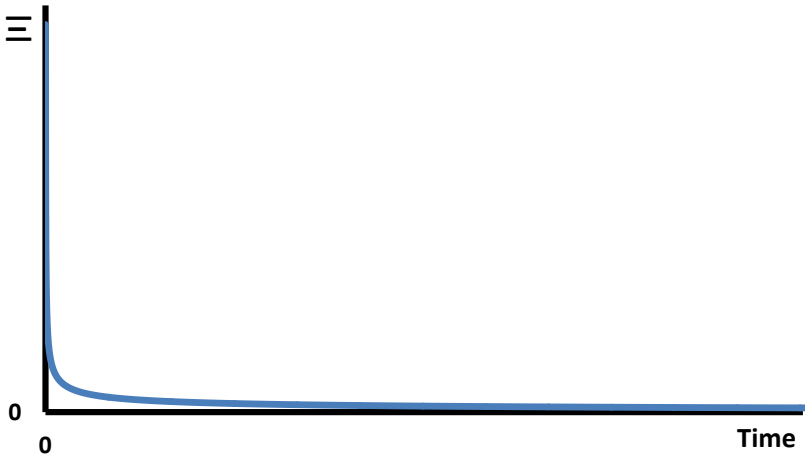

Figure 2.21 – Variation of current with time according to the Cottrell equation.

Due to double layer charging, for small values of t, there is a capacitive contribution to the current that has to be subtracted; this subtraction must take into account the ohmic drop.[4,20]

The concentration profile, near the electrode surface, can also be obtained using also Fick's second law. In this case chronopotentiometry is the technique used. In chronopotentiometry a constant current is applied to the electrode, this causes the oxidation or reduction of the electroactive species; the variation of potential is recorded with time.

For planar electrodes the variation of concentration with time is given by,

$$C_0 = C_\infty \mathrm{erf}\left[\frac{x}{2(Dt)^{1/2}}\right] \qquad (2.34)$$

Equation (2.34) is obtained by applying the Laplace transform and the same boundary conditions as before, with the exception of the third that now takes the form

$$\left.\begin{matrix} t > 0 \\ x = 0 \end{matrix}\right\} \Longrightarrow i = nFDA\left(\frac{\partial C(x,t)}{\partial x}\right)_{x=0}$$

The concentration gradient is being imposed at the electrode surface.

Figure 2.22 shows the concentration profile for several times after the start of a Cottrell experiment.

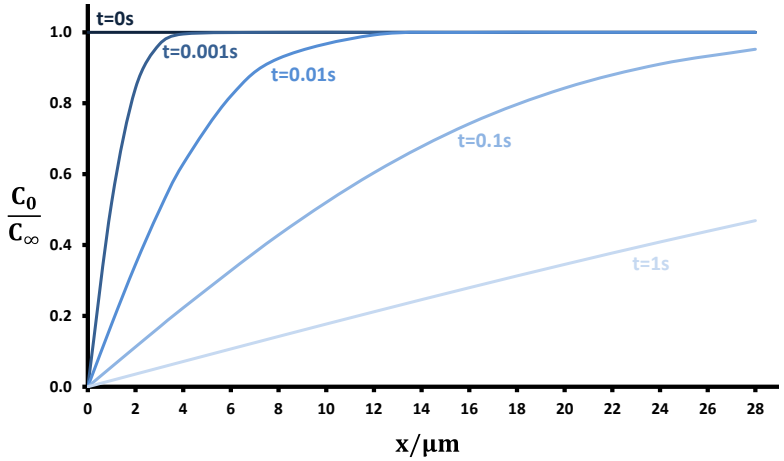

Figure 2.22 – Concentration profile for several times after the start of a Cottrell experiment. D=1.0×10^{-5} cm^2 s^{-1}.[3,4]

2.6.2. Diffusion at Spherical Electrodes

For spherical electrode, Fick's second law takes the following form,

$$\frac{\partial C}{\partial t} = D\left(\frac{\partial^2 C(r,t)}{\partial r^2} + \frac{2}{r}\frac{\partial C(r,t)}{\partial r}\right) \qquad (2.35)$$

The boundary conditions necessary to solve Fick's second law for spherical electrode are:

$\left.\begin{matrix} t = 0s \\ r \geq r_0 \end{matrix}\right\} \Longrightarrow C_0 = C_\infty$ When there is no electrode reaction, there is no concentration gradient.

$t \geq 0s \Longrightarrow \lim_{x \to \infty} C = C_\infty$ At large distances from the electrode surface there is no variation in concentration.

$\left.\begin{matrix} t > 0 \\ r = r_0 \end{matrix}\right\} \Longrightarrow C_0 = 0$ There is no concentration of electroactive specie in the electrode surface.

The diffusion – limited equation is then given by,

$$I_d(t) = nFADc_\infty \left[\frac{1}{(\pi Dt)^{1/2}} + \frac{1}{r_0}\right] \qquad (2.36)$$

Equation (2.36) is the Cottrell equation plus a spherical term dependent on the reciprocal of the electrode radius,

$$I_d(t) = \underbrace{\frac{nFAD^{1/2}C_\infty}{(\pi t)^{1/2}}}_{\textit{Cottrell Equation}} + \underbrace{\frac{nFADC_\infty}{r_0}}_{\textit{Spherical correction}} \qquad (2.37)$$

The diffusion – limited equation for spherical electrodes presents two extremes.[3,4,39]

- For short times, the spherical diffusion is much smaller than the linear diffusion and the second term of equation (2.37) can be neglected. This means that the diffusion equation is the Cottrell equation.
- For long times the spherical term dominates, and the current is given only by the second term of equation (2.37), this is a steady – state current. However, in macroelectrodes the steady state is never achieved due to effects of natural convection. This steady state is only reachable on microelectrodes, because the smaller the area the faster the steady state is achieved. The steady – state is

achieved when the rate of electrolysis is equal to the rate at which the electroactive specie diffuses to the electrode surface.

- The intermediate between the two limits should be avoided because the mass transport process becomes too complicated.

The concentration profile, near the spherical electrodes surface has as third boundary condition

$$\left.\begin{matrix} t > 0 \\ r = r_0 \end{matrix}\right\} \Longrightarrow i = nFDA\left(\frac{\partial C(r,t)}{\partial r}\right)_{r=r_0}$$

The concentration gradient is being imposed at the electrode surface.

and is given by,

$$C_0 = C_\infty - \frac{r_0}{r} erfc\left[\frac{r - r_0}{2(Dt)^{1/2}}\right] \qquad (2.38)$$

2.6.3. Diffusion at Microdisc Electrodes

For microdisc electrodes the current response is expressed using a modified equation of spherical electrodes (equation (2.37)), despite the non – uniform flux (the diffusion layer is a semi-sphere) of electroactive species to the electrode surface.[3,4,40]

Substituting r_0 by $\frac{\pi a}{4}$, with a being the radius of the disc, the equation for the variation of current with time is given by,

$$I_d(t) = \frac{nFAD^{1/2}C_\infty}{(\pi t)^{1/2}} + \frac{4nFADC_\infty}{\pi a} \qquad (2.39)$$

The two limits that were valid for spherical electrodes are also valid for microdisc electrodes. At short times, the current is given by the Cottrell equation (equation (2.33)) and at larger times is given by the second term of equation (2.39),

$$I_d(t) = \frac{4nFADC_\infty}{\pi a} \qquad (2.40)$$

The area of the microdisc, A, can be replaced by (πa^2), yielding

$$I_d(t) = 4nFADC_\infty a \qquad (2.41)$$

Equation (2.41) is known as the steady – state current equation.[3,4,39]

The terms "short" and "long" times mentioned before are relative terms, so there is the need to determine the times over which transient and steady – state behaviours will predominate and how this time regime is affected by the electrode radius. This is done by considering the ratio between both behaviours $\left({steady - state}/{transient} \right)$ and yields a dimensionless parameter,

$$\chi = \frac{\sqrt{\pi Dt}}{a} \qquad (2.42)$$

This expression can be used to calculate the time required so that the steady – state contribution will dominate the total current to a specified extent (e.g. 10 times).[39]

2.6.4. Diffusion Layer

At large distances from the electrode the concentration gradient tend asymptotically to zero and it is not linear. As a model, however, the diffusion layer is defined by,

$$D\left(\frac{\partial c}{\partial x}\right)_0 = D\,\frac{(c_\infty - c_0)}{\delta} \qquad (2.43)$$

where δ is the diffusion layer thickness, figure 2.23. Nernst[41] introduced an approximation defining the diffusion layer as the extrapolation of the concentration

gradient at the electrode surface until the bulk concentration is obtained.[4] The diffusion layer thickness can be related to the mass transfer coefficient (k_d), since when $c_0 = 0$

$$k_d = \frac{D}{\delta} \qquad (2.44)$$

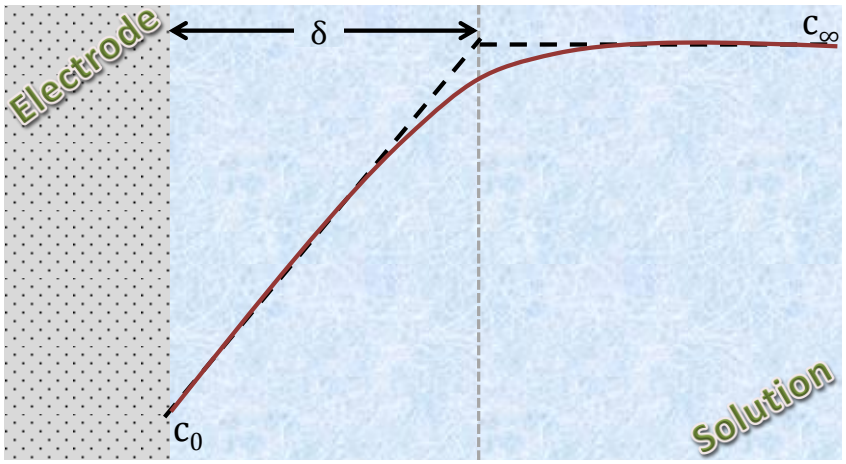

Figure 2.23 – The definition of the diffusion layer. $\left(\frac{\partial c}{\partial x}\right)_0$ is the concentration gradient at the electrode surface.

Inserting equation (2.43) to the Cottrell equation leads to the following expression,

$$\delta = (\pi D t)^{1/2} \qquad (2.45)$$

The thickness increases with $t^{1/2}$. This proves that for large t, the steady – state is never reached in conventional sized electrodes.[3,4]

2.7. Kinetics and Transport in Electrode Reactions

Transport to the electrode as described in section 2.5 assumes that the transport of species to the electrode surface is made exclusively by diffusion. With the rate of diffusion within the diffusion layer being described by the mass transfer coefficient (k_d) and the rate constants for oxidation and reduction being, respectively, k_a and k_c, the following can be written (assuming a simple electrode reaction $O + ne^- \rightarrow R$)

$$O_\infty \underset{k_{d,O}}{\overset{k_{d,O}}{\rightleftharpoons}} O_* \underset{k_a}{\overset{k_c}{\rightleftharpoons}} R_* \underset{k_{d,R}}{\overset{k_{d,R}}{\rightleftharpoons}} R_\infty$$

according to figure 2.24, where $k_{d,O}$ and $k_{d,R}$ are the mass transfer coefficients of the species O and R. Usually the mass transfer coefficients for O and R are different because this diffusion coefficients are different. Previously (section 2.5) the Butler – Volmer expressions for the kinetic rate constants were defined as,

$$k_c = k_0 \exp\left[\frac{-\alpha_c nF\left(E - E_f\right)}{RT}\right] \qquad (2.46)$$

$$k_a = k_0 \exp\left[\frac{\alpha_a nF\left(E - E_f\right)}{RT}\right] \qquad (2.47)$$

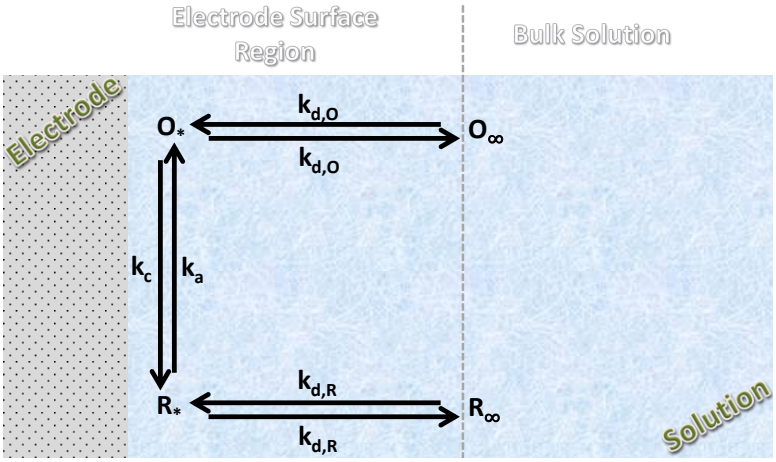

Figure 2.24 – Schematic representation for an oxidation – reduction reaction on an electrode surface.

Assuming that the rate of transport of electroactive species is equal to the rate of their reaction on the electrode surface – steady state $\left(\frac{\partial c}{\partial t}\right) = 0$; the flux of electroactive species is,

$$\left.\begin{aligned} J &= -k_c[O]_* + k_a[R]_* \\ &= k_{d,O}([O]_* - [O]_\infty) \\ &= k_{d,R}([R]_\infty - [R]_*) \end{aligned}\right\} \qquad (2.48)$$

When all the electroactive specie that reaches the electrode is oxidised or reduced, the diffusion – limited cathodic $(j_{L,c})$ or anodic $(j_{L,a})$ currents densities are obtained,

$$\frac{j_{L,c}}{nF} = -k_{d,O}[O]_\infty \qquad (2.49)$$

$$\frac{j_{L,a}}{nF} = -k_{d,R}[R]_\infty \qquad (2.50)$$

Since $k_d = \frac{D}{\delta}$ (equation (2.44)),

$$\frac{k_{d,O}}{k_{d,R}} = p = \left(\frac{D_O}{D_R}\right)^s \qquad (2.51)$$

Equation (2.48) becomes,

$$j = \frac{k_c j_{L,c} + p k_a j_{L,a}}{k_{d,O} + k_c + p k_a} \qquad (2.52)$$

When only O or R is present in solution equation (2.52) becomes, respectively,

$$-\frac{1}{j} = \frac{1}{\underbrace{nFk_c[O]_\infty}_{Kinetics}} + \frac{1}{\underbrace{nFk_{d,O}[O]_\infty}_{Transport}} \qquad (2.53)$$

$$\frac{1}{j} = \frac{1}{\underbrace{nFk_a[R]_\infty}_{Kinetics}} + \frac{1}{\underbrace{nFk_{d,R}[R]_\infty}_{Transport}} \qquad (2.54)$$

Equations (2.53) and (2.54) show that the total flux is due to a kinetic and a transport term. If $k_{c/a} \gg k_{d,O/R}$,

$$-\frac{1}{j} = \frac{1}{\underbrace{nFk_{d,O}[O]_\infty}_{Transport}} \qquad (2.55)$$

$$\frac{1}{j} = \frac{1}{\underbrace{nFk_{d,R}[R]_\infty}_{Transport}} \qquad (2.56)$$

On the other hand, if $k_{c/a} \ll k_{d,O/R}$

$$-\frac{1}{j} = \frac{1}{\underbrace{nFk_c[O]_\infty}_{Kinetics}} \qquad (2.57)$$

$$\frac{1}{j} = \frac{1}{\underbrace{nFk_a[R]_\infty}_{Kinetics}} \qquad (2.58)$$

The kinetic rate constants (k_c and k_a) depend on the applied potential and on the standard rate constant, k_0; k_d depends on the diffusion layer thickness. Altering $k_{c/a}$ and/or k_d two extreme situations are possible:

- $k_0 \gg k_d$ and in this case the systems is reversible, meaning that there is always equilibrium at the electrode surface and is possible to apply the Nernst equation at any potential;
- $k_0 \ll k_d$, in this case the system is said to be irreversible; kinetics are very important especially at potentials close to the equilibrium potential. It is necessary to apply a higher potential to overcome the activation barrier and allow the reaction to occur.[3,4]

2.8. Electrochemical Techniques

2.8.1. Cyclic Voltammetry

Cyclic voltammetry (CV) is, probably, the first technique that any electrochemist uses. The boost that made this technique flourish was the theoretical/simulation studies done by Nicholson and Shain.[42,43] Among other conclusions, they showed that cyclic voltammetry could be used to measure standard rate constants for electron transfer.[43]

Cyclic voltammetry is simple and gives qualitative and quantitative information about electrochemical reactions. A standard cyclic voltammetry experiment is made in a three electrode set-up (working, reference and counter electrodes).[3,4]

Like in other amperometric techniques, a potential is applied to the working electrode and the reply to that stimulus comes in the form of Faradaic current which is measured. In the case of CV the potential that is applied to the working electrode is swept from a starting potential ($E_{initial}$) to the end potential (E_{final}) and then swept to the end potential (which may be equal to the starting potential but does not have to be), figure 2.25. The potential applied is changed as a function of time at a defined rate; this rate is known as scan rate (ν).[3,4,22,44]

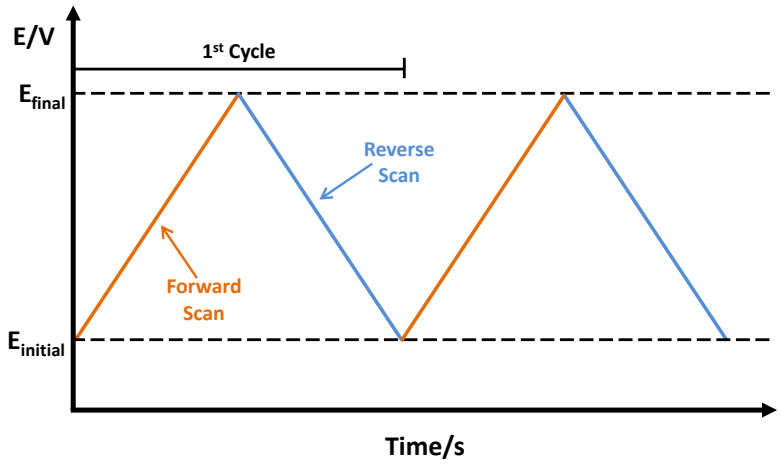

Figure 2.25 – Variation of the potential applied with time in cyclic voltammetry. The potential is applied in a triangular shape.

The current that is measured as a response to the applied potential includes the Faradaic current – current due to the redox reaction, and the Capacitive current – current due to the double layer charging; this current can be minimised by the addition of background/supporting electrolyte to the electrochemical cell.[4,6,22]

The current that is generated by the redox reaction is plotted as a function of the applied potential. The form of the voltammogram, i.e. the faradaic current, depends on i) the standard heterogeneous rate constant, k_0, and the formal potential of the redox couple; ii) the diffusion coefficient of O and R and iii) on the scan rate, together with the initial and final potentials.[4,22]

2.8.1.1. Cyclic Voltammetry at Planar Electrodes

For planar electrodes, the following equations have to be solved

$$\frac{\partial[O]}{\partial t} = D_O \frac{\partial^2[O]}{\partial x^2} \qquad (2.59)$$

$$\frac{\partial[R]}{\partial t} = D_R \frac{\partial^2[R]}{\partial x^2} \qquad (2.60)$$

with the following boundary conditions

$$t = 0 \quad x = 0 \quad [O]_* = [O]_\infty \quad [R]_* = 0 \qquad (2.61)$$

$$t > 0 \quad x \to \infty \quad [O] \to [O]_\infty \quad [R] \to 0 \qquad (2.62)$$

$$t > 0 \quad x = 0 \quad D_O \left(\frac{\partial[O]}{\partial x}\right)_0 + D_R \left(\frac{\partial[R]}{\partial x}\right)_0 = 0 \qquad (2.63)$$

$$\left.\begin{array}{ll} 0 < t \leq \lambda & E = E_{initial} - \upsilon t \\ t > \lambda & E = E_{initial} - \upsilon\lambda + \upsilon(t - \lambda) \end{array}\right\} \qquad (2.64)$$

where λ is the value at which the potential is inverted/switched. Another boundary condition expresses the kinetic regime of the electrode reaction. [4,22]

- **Reversible Systems**

In the case of reversible systems the last boundary condition is the Nernst equation

$$\frac{[O]_*}{[R]_*} = exp\left[\frac{nF}{RT}\left(E - E_f\right)\right] \qquad (2.65)$$

The Laplace transformation of the diffusion equation and application of the boundary conditions leads to a result that, after being numerically solved, yields

$$i = -nFA[O]_\infty(\pi D_O \sigma)^{\frac{1}{2}}\chi(\sigma t) \qquad (2.66)$$

where

$$\sigma = \left(\frac{nF}{RT}\right)\upsilon \qquad (2.67)$$

$$\sigma t = \frac{nF}{RT}(E_{initial} - E) \qquad (2.68)$$

leading to the current being dependent on the square root of the scan rate. χ is a dimensionless variable.[3,4,22]

Values of the current functions $\pi^{1/2}\chi(\sigma t)$ have been determined and have a maximum value of 0.4463.[4,42] From equation (2.66) Randles[45] and Sevcik[46] obtained the peak current,

$$i_p = 0.4463\, nFAC\left(\frac{nFD\nu}{RT}\right)^{1/2} \qquad (2.69)$$

that at T=298K becomes

$$i_p = 2.69 \times 10^5 n^{3/2} A D^{1/2} C \nu^{1/2} \qquad (2.70)$$

Where

n – Number of electrons,

D – Diffusion coefficient ($cm^2\ s^{-1}$),

C – Bulk concentration of electroactive species ($mol\ cm^{-3}$),

ν – Scan rate ($V\ s^{-1}$),

A – Surface area of the working electrode (cm^2).

Other conclusions can be obtained from the values of current functions $\pi^{1/2}\chi(\sigma t)$, the anodic and cathodic peaks should have the same intensity, and the separation between the anodic and cathodic peaks is $^{57mV}/_{n}$ (at 298 K), with n being the number of electrons.[3,4,20,22]

Characteristic of cyclic voltammetry for reversible reactions is that the peak potential is independent of the scan rate, the formal potential, E_f^0, is centred between the anodic peak potential and the cathodic peak potential. [3,4,20,22]

In the case of reversible systems a typical voltammogram is shown in figure 2.26.

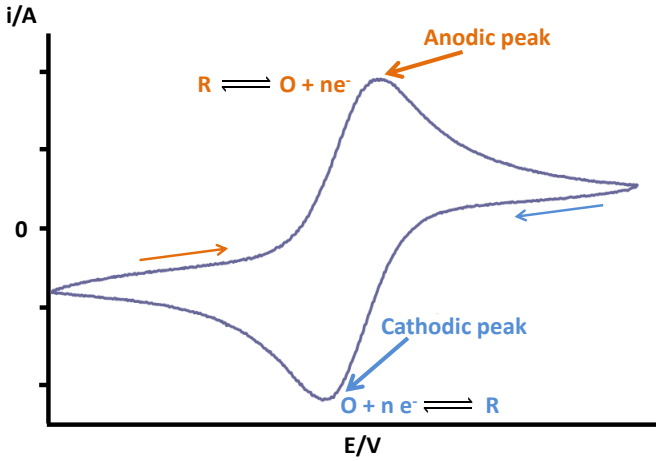

Figure 2.26 – Schematic representation of a cyclic voltammogram for a reversible system.

- **Irreversible Systems**

For irreversible systems the fifth boundary condition is

$$D_O \frac{\partial [O]_*}{\partial x} = k_c [O]_* = k_c' exp\{bt\}[O]_* \qquad (2.71)$$

for a reduction, where

$$k_c' = k_0 exp\left[\left(\frac{-\alpha_c n' F}{RT}\right)\left(E_{initial} - E_f\right)\right] \qquad (2.72)$$

and

$$b = \frac{\alpha_c n' F v}{RT} \qquad (2.73)$$

n' being the number of electrons transferred in the rate limiting step and k_c the rate constant for reduction.[4]

The solution to the diffusion equation is found the same way as it was for the case of reversible reactions and leads to

$$i = nFA[O]_* D_O^{1/2} v^{1/2} \left(\frac{\alpha_c n' F}{RT}\right)^{1/2} \pi^{1/2} \chi(bt) \qquad (2.74)$$

The current functions $\pi^{1/2}\chi(\sigma t)$ have a maximum value of 0.4958.[4,42] The peak current is described by

$$i_p = -2.99 \times 10^5 n(\alpha_c n')^{\frac{1}{2}} A[O]_\infty D_O^{\frac{1}{2}} v^{\frac{1}{2}} \qquad (2.75)$$

The peak potential can also be determined and is given by,

$$E_p = E_f - \frac{RT}{\alpha_c n' F}\left[0.780 + \ln \frac{D_O^{\frac{1}{2}}}{k_0} + \frac{1}{2}\ln b\right] \qquad (2.76)$$

Combining equations (2.75) and (2.76) the peak current is defined as,

$$i_p = -0.227nFA[O]_\infty k_0 \exp\left[\frac{-\alpha_c n' F}{RT}\left(E_p - E_f\right)\right] \qquad (2.77)$$

The cyclic voltammogram for an irreversible system shows only the reduction peak while in the reverse scan only the capacitive current is observable, figure 2.27.

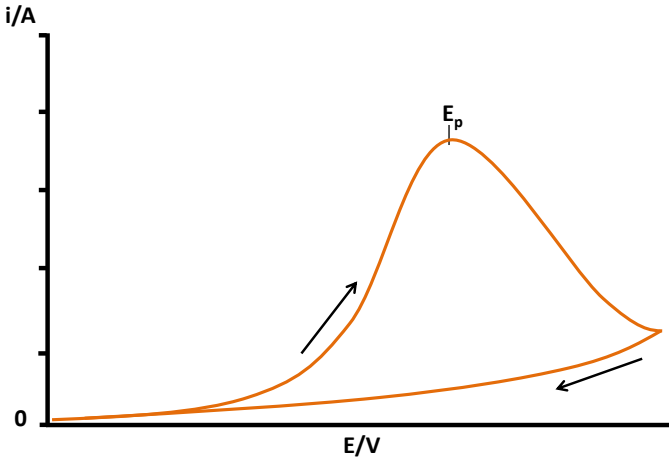

Figure 2.27 – Cyclic voltammogram for an irreversible system ($O + ne^- \rightarrow R$). In the reverse scan only the capacitive current is observed.

- **Quasi – Reversible Systems**

The two cases described above are the extreme cases; the quasi – reversible systems represent an intermediate case. In this intermediate kind of reaction the kinetics of oxidation and reduction have to be considered simultaneously. In the quasi – reversible systems the degree of irreversibility and the difference between the anodic and cathodic peaks increases with the increase of the scan rate while the peak current (correspondent to the reversible case) decreases, figure 2.28.[4,22]

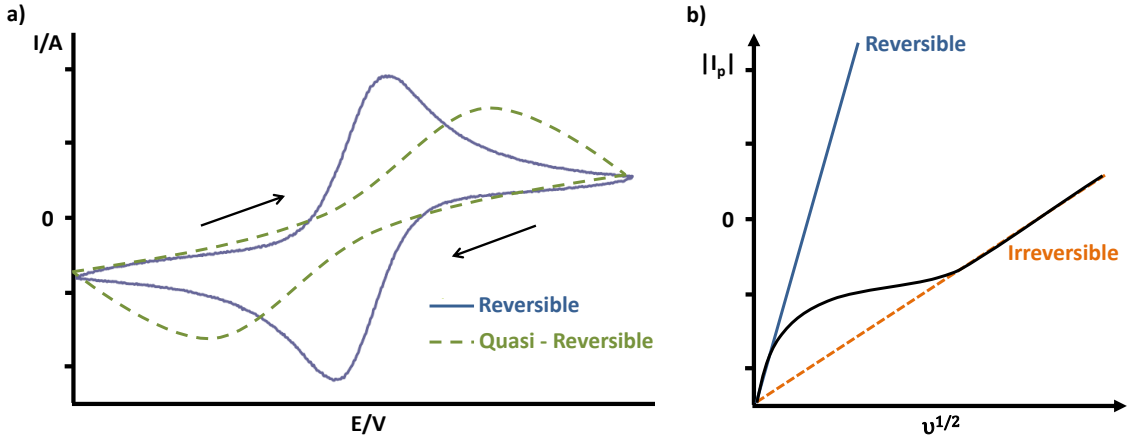

Figure 2.28 – a) Schematic representation for the increase of irreversibility on a quasi – reversible system. b) Transition from a reversible to an irreversible system with the increase in the scan rate.

The peak shape and associated parameters can be described by the ratio kinetics/transport, Λ, which is a quantitative measure of reversibility

$$\Lambda = \frac{k_0}{\left(D_O^{\alpha_a} D_R^{\alpha_c} \sigma\right)^{1/2}} = \frac{k_0}{\left(D_O^{(1-\alpha_c)} D_R^{\alpha_c} \sigma\right)^{1/2}} \qquad (2.78)$$

When $D_R = D_O$

$$\Lambda = k_0 D^{-1/2} \sigma^{-1/2} \qquad (2.79)$$

showing that small Λ corresponds to large scan rates $\left(\sigma = \left(\frac{nF}{RT}\right)\upsilon\right)$.[4]

For quasi – reversible systems, Matsuda and Ayabe[47] described Λ and k_0 as,

$$\left.\begin{array}{c} 10^{-2(1-\alpha)} < \Lambda < 15 \\ 2 \times 10^{-5} v^{1/2} < k_0 < 0.3 v^{1/2}\ cm\ s^{-1} \end{array}\right\} \qquad (2.80)$$

For $0.3 < \alpha < 0.7$, the peak potential is close to exclusively dependent on Λ and almost does not change with α.[4]

- **Adsorbed Species**

When species adsorb to the electrode surface the shape of the voltammogram changes. If the rate of reaction of the adsorbed species is much greater than that of the species in solution, the peak current is given by

$$i = \frac{-n^2F^2\upsilon A\Gamma_{O,i}}{4RT} \qquad (2.81)$$

where,

$\Gamma_{O,i}$ – surface concentration of adsorbed O,

A – Area of the electrode

if $(b_O/b_R)\theta=1$.[4]

$$\theta = \exp\left[\frac{nF}{RT}\left(E - E_f\right)\right] \qquad (2.82)$$

The peak potential is the same for the oxidation and for the reduction and is given by,

$$E_p = E_f - \frac{RT}{nF}\ln\left(\frac{b_O}{b_R}\right) \qquad (2.83)$$

If both O and R are adsorbed with the same strength, $E_p=E_f$.

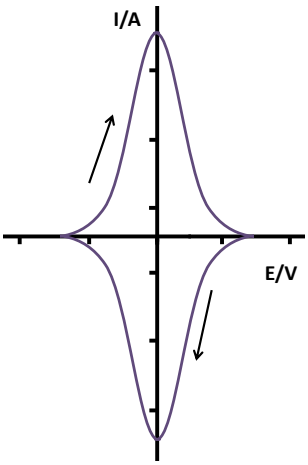

Figure 2.29 – Cyclic voltammogram for a reversible reaction of species adsorbed on the electrode.

2.8.1.2. Cyclic Voltammetry at Microdisc Electrodes

Although there is no consistency in the definition of microelectrode, there is a general agreement on the essential concept: the electrode is smaller than the scale of the diffusion layer.[3,40]

In the case of microdisc electrodes a typical voltammogram, at low scan rates, will present a sigmoidal shape (figure 2.30). This is due to radial diffusion and high mass transport rates. At high scan rates, a peak shaped voltammogram is obtained. The equation that defines the steady – state current (I_{ss}) is equation (2.41). To increase the current signal, but keeping all the characteristics of a microelectrode, often an array of microelectrodes is used. In that case equation (2.41) takes the form,

$$I = 4ZnFDC_{\infty}a \qquad (2.84)$$

with Z being the number of microelectrodes in the array.[3,4,40]

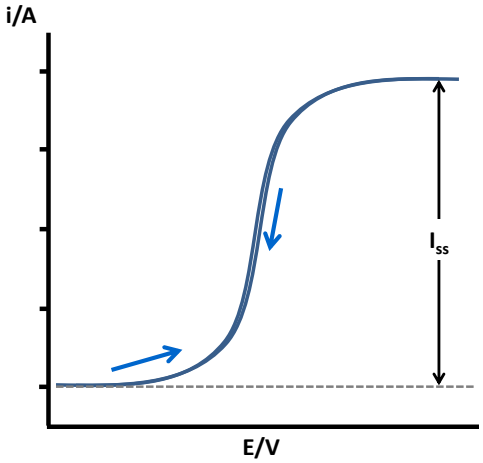

Figure 2.30 – Typical cyclic voltammogram for a microelectrode for a reversible reaction.

In the case of microelectrode arrays, the shape of the voltammogram is highly dependent on i) size of the individual diffusion zones, δ, vs. the size of the discs themselves, a, and ii) the size of the diffusion zones vs. the centre to centre separation, d.

Based on these two factors, the four categories to which an array can be assigned and summarises the cyclic voltammetric characteristics associated with each category are illustrated next.[48,49]

- **Individual small diffusion layers: linear diffusion**

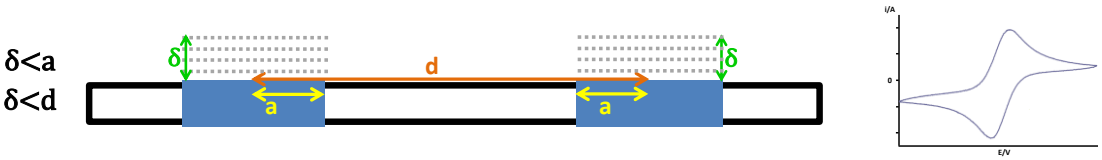

The cyclic voltammogram presents macroelectrode behaviour.

- **Individual diffusion layers: radial diffusion**

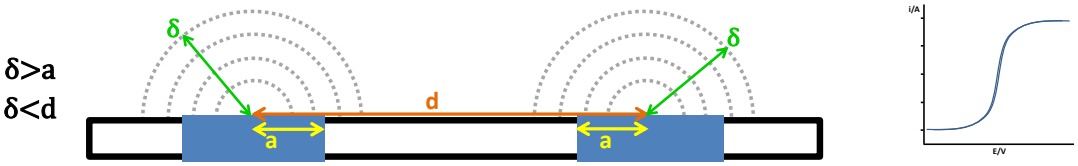

For certain scan rates, steady – state current is achieved; cyclic voltammetric behaviour of microelectrode.

- **Overlapping diffusion layers: mixed diffusion**

δ>a
δ>d

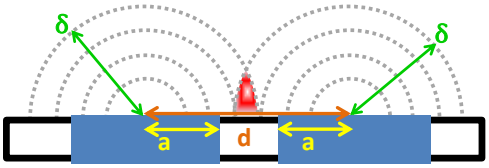

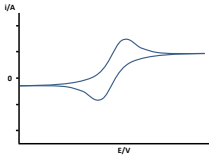

Cyclic voltammetric behaviour of quasi – microelectrode. This regime is difficult to analyse and should be avoided.

- **Heavy overlapping diffusion layers: linear diffusion**

δ>a
δ>>d

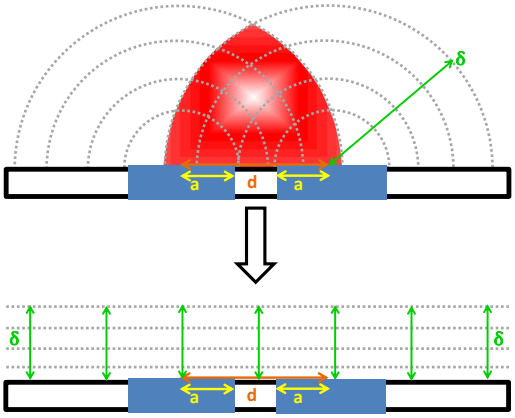

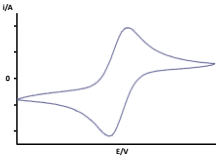

The heavy overlapping of the radial diffusion layers is equivalent to a linear diffusion layer. Cyclic voltammetric behaviour of macroelectrode.

2.8.2. Electrochemical Impedance Spectroscopy

Electrochemical impedance spectroscopy (EIS) can be used to study electrochemical systems. One advantage of impedance measurements is that these involve only a small perturbation to the equilibrium, while sweep or step techniques involve perturbations away from the equilibrium.[3,4,50]

Electrochemical impedance is based on electrical impedance which is similar to electrical resistance, and can be represented by an equation that is analogous to Ohm's law,

$$E = I.Z \qquad (2.85)$$

Where

E – AC potential (V),

I – current (A)

Z – impedance (Ω)

In EIS, usually, an AC potential is applied to the electrochemical cell in a sinusoidal form and the AC current is measured through the cell. Because the perturbation on the applied potential is small the response is pseudo – linear; this means that the response to the sinusoidal potential is current at the same frequency but shifted in phase, figure 2.31.[3,4,50,51]

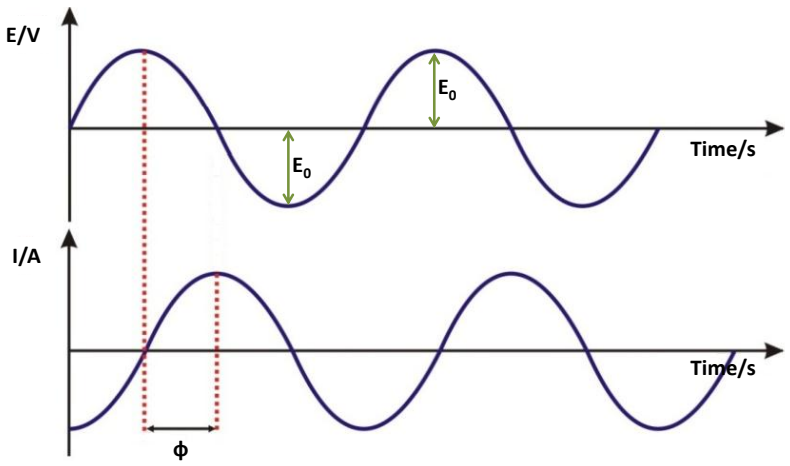

Figure 2.31 – Sinusoidal current response in a linear system. Φ is the phase shift. E_0 is the potential amplitude.

The potential applied can be expressed as a function of time

$$E(t) = E_0 \sin(\omega t) \qquad (2.86)$$

where

E(t) – potential at time t (V),

E_0 – potential amplitude (V),

ω – radial frequency (rad s^{-1}),

t – time (s)

the relationship between the radial frequency and frequency is

$$\omega = 2\pi f \qquad (2.87)$$

As said above, in a linear or pseudo – linear system, the response to the stimulus presents a phase shift, ϕ, and the amplitude is I_0

$$I(t) = I_0 \sin(\omega t + \phi) \qquad (2.88)$$

Replacing E and I in equation (2.85) for equations (2.86) and (2.88), respectively, yields

$$Z = \frac{E(t)}{I(t)} = \frac{E_0 \sin(\omega t)}{I_0 \sin(\omega t + \phi)} = Z_0 \frac{\sin(\omega t)}{\sin(\omega t + \phi)} \qquad (2.89)$$

The impedance is expressed as magnitude, Z_0, and phase shift, ϕ.[4]

The plot the current response, I(t), as a function of the applied potential, E(t), results in the Lissajous figure, figure 2.32.[4,50]

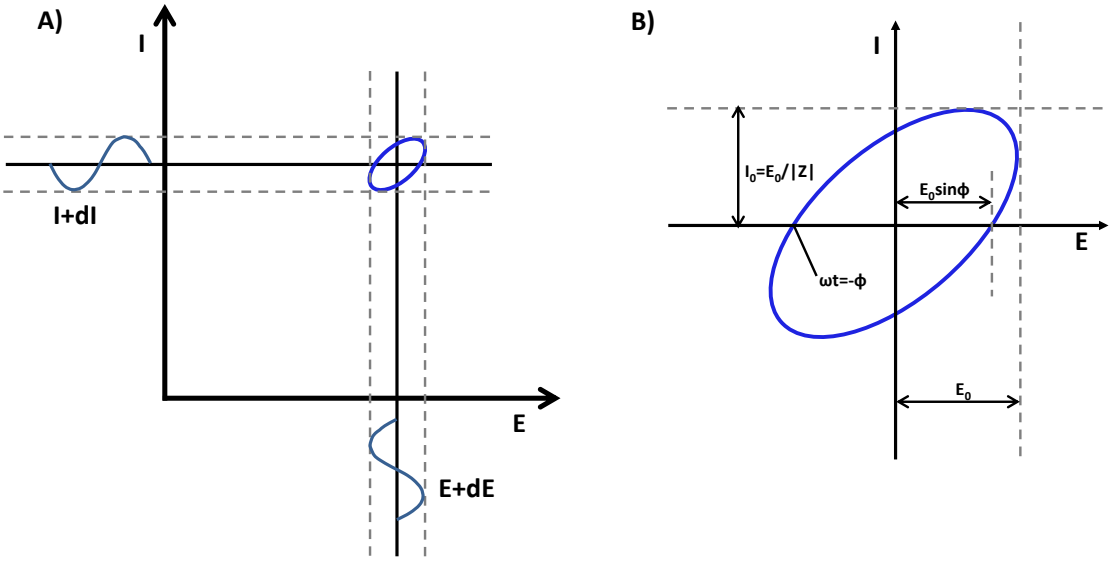

Figure 2.32 – A) plot of the current response, I(t), as a function of the applied potential, E(t), results in B) the Lissajous figure. |Z| represents the total impedance.

Using Eulers relationship,

$$\exp(j\phi) = cos\phi + jsin\phi \qquad (2.90)$$

the impedance can be expressed as a complex function; j is the imaginary number $\sqrt{-1}$. The potential is then described as,

$$E(t) = E_0 \exp(j\omega t) \qquad (2.91)$$

and the current as,

$$I(t) = I_0 \exp(j\omega t - \phi) \qquad (2.92)$$

Replacing E and I in equation (2.85) for equations (2.91) and (2.92), respectively, results in the impedance being represented as a complex number,

$$Z(\omega) = \frac{E}{I} = Z_0 \exp(j\phi) = Z_0(cos\phi + jsin\phi) \qquad (2.93)$$

That can be rewritten as,

$$Z(\omega) = Z' + jZ'' \qquad (2.94)$$

where Z' represents the real part of impedance and Z'' the complex (or imaginary) part.[3,4,50]

2.8.2.1. Equivalent Circuits

An electrochemical cell can be represented by an equivalent circuit containing resistors and capacitors. The most known equivalent circuit is the Randles equivalent circuit, figure 2.33.[4,52]

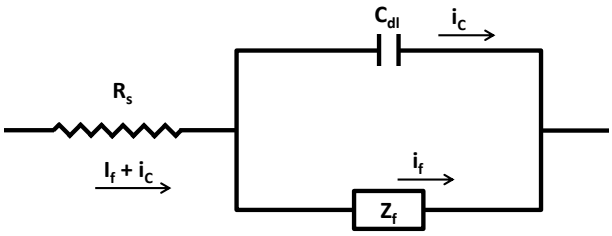

Figure 2.33 – Randles equivalent circuit of an electrochemical cell. See text for more details.

The solution resistance, R_s, comes from the fact that all the current passes through the solution. The parallel components in the Randles circuit come from the fact that the current in the working interface is the sum of the faradaic (i_f) and capacitive (i_c) currents. C_{dl} corresponds to the double – layer capacitance and Z_f is the faradaic impedance. The latter can be divided in two ways:[3,4]

1. The simplest way is to consider the faradaic impedance as a series combination which includes a resistance, R, and a pseudo – capacitance, Cs,

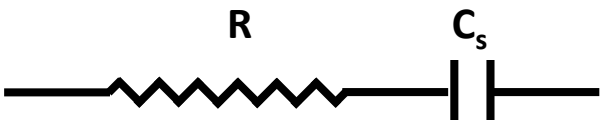

2. One other way is to separate it in a pure resistance, R_{ct} – charge transfer resistance, and the Warburg impedance, Z_w, which represents the resistance to mass transfer (models semi-infinite linear diffusion, that is, unrestricted diffusion to a large planar electrode)

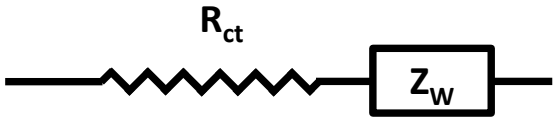

Unlike R_s and C_{dl}, which are almost ideal components, the components of the faradaic impedance are not ideal because they change with the frequency.[3]

In mass transfer controlled reactions $R_{ct} \rightarrow 0$ and Z_W predominates, for kinetically controlled reactions $R_{ct} \rightarrow \infty$ and R_{ct} predominates.[3,4]

The Randles circuit is based on simplest electrode processes; other elements may be inserted in the equivalent circuit to represent more complex electrochemical cells.[4]

One example of other elements that can be used is the constant phase element (CPE). The CPE represents an imperfect capacitor; its impedance is given by

$$\frac{1}{Z} = Q^0(j\omega)^n \qquad (2.95)$$

where Q^0 has the numerical value of admittance with (S s^n) as unit.

When n=1, the CPE behaves similarly to a pure capacitor but with ϕ less than 90^0; when n=0, the CPE behaves as an resistor. This element can be used to account for various situations such as the surface roughness, inhomogeneous reaction rates on the surface and varying thickness or composition of a coating on the electrode surface.[50]

2.8.2.2. Representation of EIS data

There are two ways of representing the data that is collected during an EIS experiment, Nyquist, figure 2.34 a), and Bode plots, figure 2.34 b).

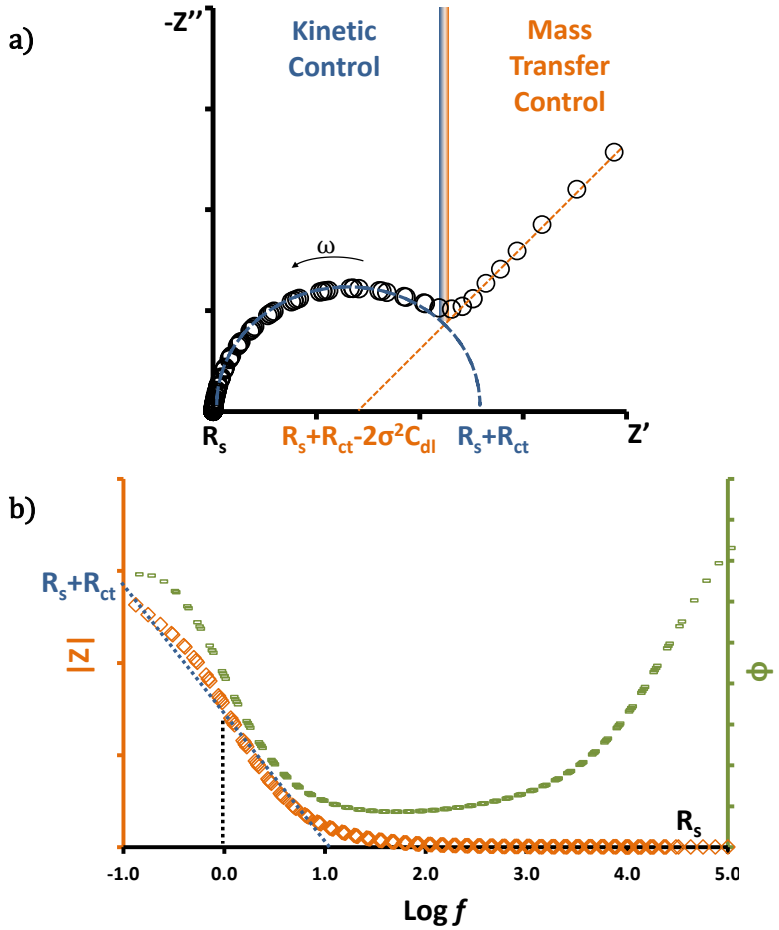

Figure 2.34 – a) Nyquist plot and b) Bode plot. $\sigma = \frac{RT}{n^2F^2A\sqrt{2}}\left(\frac{1}{D_O^{1/2}[O]_\infty}+\frac{1}{D_R^{1/2}[R]_\infty}\right)$

In the Nyquist plot the imaginary part of impedance (Z '') is plotted as a function of the real part of impedance (Z'). This type of plot is very useful but has the disadvantage of being difficult to compare two spectra when the charge transfer resistances are very different, also this plot does not indicate the frequency at which each measurement is made. The solution resistance, R_s, has the value of where the scan starts (R_s=Z' at the highest frequency of the measurement); R_{ct} is the intercept of the prolongation of the

semi – circle with Z'. The extrapolation of the low–frequency straight line allows the determination of C_{dl}. The straight line at low frequencies corresponds to a reaction controlled solely by diffusion – mass transfer control.[3,4] At high frequencies the control is purely kinetic, all the current is capacitive current and the only impedance is the ohmic resistance.[3,4]

In Bode plots both the total impedance, |Z|, and the phase shift, ϕ, are plotted as a function of the frequency.[4,50,52] One advantage of the Bode plot is that it shows features at high frequencies which are "hidden" in the Nyquist plot.[4] Extrapolation of the sloped line, where log (f)=0, to the y – axis gives the value of R_s+R_{ct}.[53] Analogous to the Nyquist plot, R_s has the value of |Z| at the highest frequency.

References

(1) Hibbert, D. B. *Introduction to electrochemistry*; Macmillan: London, 1993.
(2) Crow, D. R. *Principles and Applications of Electrochemistry*; Blackie Academic & Professional: London, 1994.
(3) Bard, A. J.; Faulkner, L. R. *Electrochemical methods: fundamentals and applications*; 2nd ed.; John Wiley & Sons: New York, 2001.
(4) Brett, A. M. O.; Brett, C. M. A. *Electroquimica - Principios, Metodos e Aplicacoes*; OUP, Livraria Almedina: Coimbra, 1996.
(5) Riley, T.; Tomlinson, C. *Principles of Electroanalytical Methods*; James, A. M., Ed.; Wiley-Blackwell, 1987.
(6) *Laboratory Techniques in Electroanalytical Chemistry*; Kissinger, P.; Heineman, W. R., Eds.; 2nd ed.; CRC Press, 1996.
(7) Wang, J. *Analytical electrochemistry*; John Wiley and Sons: New Jersey, 2006.
(8) Bott, A. W. *Curr. Sep.* **1997**, *16*, 79–83.
(9) Compton, R. G.; Sanders, G. H. W. *Electrode Potentials*; OUP Oxford, 1996.
(10) Brett, C.; Brett, A. M. O. *Electroanalysis*; OUP: Oxford, 1998.
(11) Bott, A. W. *Curr. Sep.* **1995**, *14*, 64–68.
(12) Trasatti, S. *Pure and Applied Chemistry* **1986**, *58*, 955–966.
(13) von Helmholtz, H. L. F. *Ann. Physik.* **1853**, *89*, 211–233.
(14) von Helmholtz, H. L. F. *Ann. Physik.* **1879**, *7*, 337–382.
(15) Guoy, G. *Compt. Rend.* **1910**, *149*, 654–657.
(16) Chapman, D. L. *Phil. Mag.* **1913**, *149*, 475–481.
(17) Stern, O. *Z. Elektrochem.* **1924**, *1947*, 508–516.
(18) Grahame, D. C. *Chem. Rev.* **1947**, *41*, 441–501.
(19) Bockris, J. O.; Devanathan, M. A. V.; Muller, K. *Proc. R. Soc. A* **1963**, *274*, 55 –79.
(20) Fisher, A. C. *Electrode Dynamics*; OUP Oxford, 1996.
(21) Girault, H. H. *Analytical and Physical Electrochemistry*; 1st ed.; EFPL Press, 2004.
(22) Compton, R. G.; Banks, C. E. *Understanding Voltammetry*; World Scientific Publishing: Singapore, 2007.
(23) Butler, J. A. V. *Trans. Faraday Soc.* **1924**, *19*, 729–733.
(24) Butler, J. A. V. *Trans. Faraday Soc.* **1924**, *19*, 734–739.
(25) Erdey-Grúz, T.; Volmer, M. *Z. Physic. Chem.* **1930**, *150A*, 203–213.
(26) Libby, W. F. *J. Phys. Chem.* **1952**, *56*, 863–868.
(27) Marcus, R. A. *J Chem Phys* **1956**, *24*, 966–978.
(28) Marcus, R. A. *Electrochim Acta* **1968**, *13*, 995–1004.
(29) Hush, N. S. *J Chem Phys* **1958**, *28*, 962–972.
(30) Hush, N. S. *Electrochim Acta* **1968**, *13*, 1005–1023.
(31) Levich, V. G. *Adv. Electrochem. Electrochem. Engr.* **1966**, *4*, 249–371.
(32) Dogonadze, R. R. *Reactions of molecules at electrodes*; Hush, N. S., Ed.; Wiley-Interscience, 1971.
(33) Taube, H.; Myers, H.; Rich, R. L. *J. Am. Chem. Soc.* **1953**, *75*, 4118–4119.
(34) Weaver, M. J.; Anson, F. C. *J. Am. Chem. Soc.* **1975**, *97*, 4403–4405.
(35) Bard, A. J. *J. Am. Chem. Soc.* **2010**, *132*, 7559–7567.
(36) Marcus, R. A. *Annu. Rev. Phys. Chem.* **1964**, *15*, 155–196.
(37) Hush, N. S. *Prog. Inorg. Chem.* **1961**, *8*, 391–444.
(38) Marcus, R. A. In *Nobel Lecture*; 1992.
(39) *Handbook of Electrochemistry*; Zoski, C. G., Ed.; Elsevier Science, 2006.

(40) *Microelectrodes: Theory and Applications (NATO Science Series E:*; Montenegro, I.; Queirós, M. A.; Daschbach, J. L., Eds.; Springer, 1991.
(41) Nernst, W. *Z. Physik Chem.* **1904**, *47*, 52–55.
(42) Nicholson, R. S.; Shain, I. *Anal. Chem.* **1964**, *36*, 706–723.
(43) Nicholson, R. S. *Anal. Chem.* **1965**, *37*, 1351–1355.
(44) Heinze, J. *Angew. Chem. Int. Ed. Engl.* **1984**, *23*, 831–847.
(45) Randles, J. E. B. *Trans. Faraday Soc.* **1948**, *44*, 327–338.
(46) Sevcik, A. *Collect. Czech. Chem. Commun.* **1948**, *13*, 349–377.
(47) Matsuda, H.; Ayabe, Y. *Z. Elektrochem.* **1955**, *59*, 494–503.
(48) Davies, T. J.; Ward-Jones, S.; Banks, C. E.; del Campo, J.; Mas, R.; Muñoz, F. X.; Compton, R. G. *J Electroanal Chem* **2005**, *585*, 51–62.
(49) Davies, T. J.; Compton, R. G. *J Electroanal Chem* **2005**, *585*, 63–82.
(50) Orazem, M. E.; Tribollet, B. *Electrochemical Impedance Spectroscopy*; 1st ed.; Wiley-Interscience, 2008.
(51) Lasia, A. In *Modern Aspects of Electrochemistry*; Kluwer Academic/Plenum Publishers: New York, 1999; Vol. 32, pp. 143–248.
(52) Park, S.-M.; Yoo, J.-S. *Anal. Chem.* **2003**, *75*, 455 A–461 A.
(53) Ha, J.; Henry, C. S.; Fritsch, I. *Langmuir* **1998**, *14*, 5850–5857.

3. Experimental Methods

In this chapter are reported all the methods and materials used to produce the work that is presented in this thesis. For the reagents and chemicals is indicated the supplier and for the instruments is indicated the manufacturer. It is reported how the substrates were prepared prior to modification. The method used in the preparation of vesicles is described. It is also described how, and in which conditions, each of the techniques was performed.

3.1. Reagents and Chemicals

Potassium ferrocyanide ($K_4Fe(CN)_6$), potassium ferricyanide ($K_3Fe(CN)_6$), hexaammineruthenium (III) chloride ($Ru(NH_3)_6Cl_3$), hexaammineruthenium (II) chloride ($Ru(NH_3)_6Cl_2$), L-α-phosphatidylcholine (EggPC), β-Nicotinamide adenine dinucleotide reduced disodium salt hydrate (NADH), β-Nicotinamide adenine dinucleotide hydrate (NAD^+), 4-(2-Hydroxyethyl)piperazine-1-ethanesulfonic acid (HEPES), 1 – dodecanethiol (DDT), 1 – heptanethiol (HPT), potassium nitrate (KNO_3), avidin (egg white), potassium phosphate monobasic (KH_2PO_4), potassium phosphate dibasic (K_2HPO_4), (±)-α-tocopherol (VitE), ubiquinone-10 (UQ_{10}), methylene blue (MB) and n-decane were purchased from Sigma-Aldrich, UK. 1,2-dipalmitoyl-sn-glycero-phosphothioethanol (DPPTE) and 1,2-dioleoyl-*sn*-glycero-3-phosphoethanolamine-N-(biotinyl) (sodium salt) (DOPE(B)) were purchased from Avanti Polar Lipids, USA. Hydrogen peroxide and sulphuric acid were obtained from Acros Organics and Fluka, respectively. Solvents were

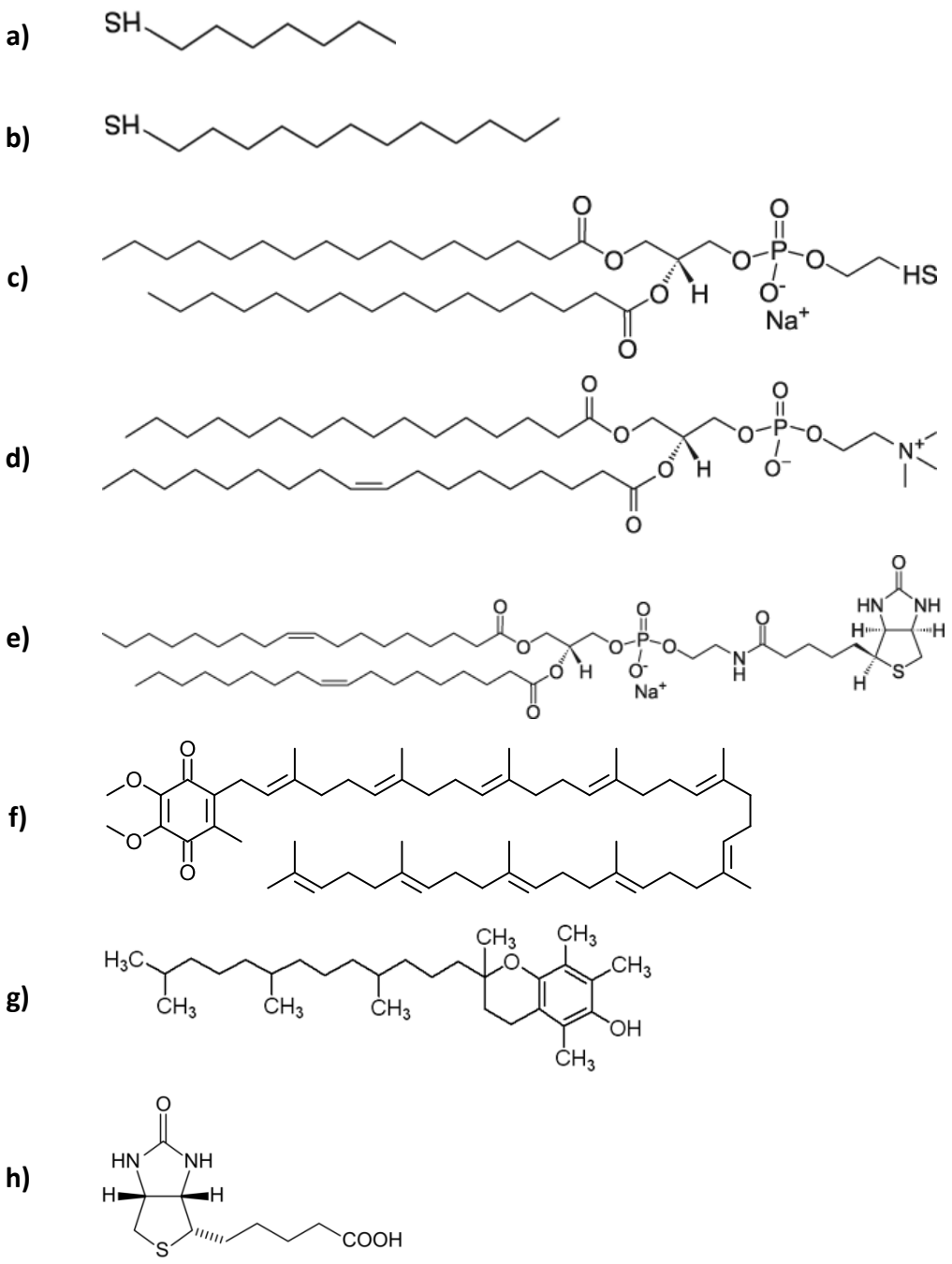

Figure 3.1 – Chemical structure of a) HPT, b) DDT, c) DPPTE, d) EggPC, e) DOPE(B), f) UQ_{10}, g) VitE and h) biotin.

used without further purification. All buffers were prepared using deionised water (Sartorius Arium 611 ultrapure water system (resistivity of not less than 18.2 MΩ cm)).

The dialysis tubes (Spectra/Por® CE Float –A – Lyser® G2, molecular weight cut off: 8 – 10 kDa) were purchased from Spectrum labs.

3.2. Instrumentation

A Potentiostat-Galvanostat Model PGSTAT12 (Autolab) interfaced with a personal computer was used for the electrochemical and for the electrochemical impedance spectroscopy (EIS) measurements; for the work presented in chapter 4 a Potentiostat-Galvanostat Model 283 (Princeton Applied Research) was used for electrochemical measurements and the electrochemical impedance spectroscopy (EIS) measurements were performed using a Solartron 1260 Impedance/Gain-Phase Analyzer connected with a PAR model 283 potentiostat interfaced with a personal computer. The ZPlot software was used to interpret the raw impedance data. A three-electrode cell containing Ag/AgCl (KCl 3.5M), Pt foil (A=1 cm^2) and either bare electrode, SAM or BLM electrodes were employed as reference, auxiliary and working electrodes, respectively. The cell was placed in a Faraday cage to eliminate external interference. All potentials in this work are reported with respect to Ag/AgCl (KCl 3.5 M). All measurements were carried out at room temperature. The Nyquist and Bode plots were fitted, according to literature precedent[1,2], using a modified Randles circuit which takes into account a frequency dependent constant phase element (CPE) instead of the double layer capacitance to account for topological imperfections of the bare electrode.

The dinamic light scattering (DLS) measurements were performed in a Zeta Plus Zeta Potential Analyser by Brookhaven Instruments Coorporation and the UV – Vis measurements were made in a HR2000LG – UV – NIR spectrophotometer, from Ocean Optics, interfaced with a personal computer.

3.3. Substrate Preparation

The formation of a monolayer on gold is strongly dependent on the cleanliness and structure of the gold prior to modification.[3,4] Polycrystalline gold electrodes were used rather than single crystal Au electrodes as they are more readily available and previous literature has shown that properly prepared surfaces are adequate for these studies provided the constant phase element is close to unity.[5] Gold is a soft metal and is readily contaminated by organic and inorganic species. Therefore, prior to monolayer preparation, the gold substrates were well cleaned in order to remove the contaminants on the surface which affect the integrity of the SAM formation. In this work, polycrystalline gold disk electrodes (Au(111)) (BASi, area 0.020 cm^2) were polished for 60 s in a figure-eight pattern on Buhler Microcloth with successively finer grades (15, 6, 3 and 1 μm) of diamond polish slurries and alumina slurry (0.05 μm) followed by sonication in ethanol and water for 10 min. Immediately before use, polycrystalline gold electrodes were cleaned by soaking in piranha solution (3:1 (v/v) 98% H_2SO_4 / 30%H_2O_2) for 20 min, rinsed with water and finally dried under Argon. (Caution: Piranha solution is a vigorous oxidant and should be handled very carefully.) Platinum electrodes (CH instruments, 0.031 cm^2) were prepared using the same method that was used for gold electrodes.

3.4. Preparation of Organic Solution of Lipids

DPPTE was received as powder, so a stock solution, 20 mg mL^{-1}, was made by dissolving the lipid in chloroform to prevent oxidation.[6] EggPC was received in chloroform solution.

To prepare the working solution, the chloroform solution of lipid (DPPTE, EggPC or a mixture of both) was placed in a glass vial and dried under a slow stream of Argon. The thin lipid film formed was dissolved in the appropriate solvent (ethanol for the work presented in chapter 4 and n-decane for the work presented in chapter 5).

3.5. Formation of Self – Assembled Monolayers

3.5.1. Self – Assembled Monolayers on Au(111)

SAMs were formed on the gold electrode by storing the substrate in a solution of the thiolated molecule – HPT, DDT, DPPTE or DPPTE+EggPC – (1 mM in ethanol) for 24 h at room temperature. Loosely bound thiol molecules were removed from the surface by rinsing successively with ethanol and water.

3.5.2. Bilayer Lipid Membranes Modified with Bio - Electroactive Molecules

SAMs were formed by dipping the gold electrode in a n-decane solution of 1mM DPPTE and 0.5mM of EggPC, or lipids and UQ_{10} (0.02 mM) and/or VitE (0. 02 mM)[7–9], for 24 hours at room temperature.[4,10–13] DPPTE molecules chemisorb to the gold surface via the thiol group. EggPC was used to fill possible gaps between the DPPTE molecules, leading to a better quality SAM.[10] The SAM produced serves as the lower leaflet of the BLM.

After SAM formation the electrodes were rinsed with n-decane and water to remove weakly attached lipids and dried using Argon.

3.5.3. Bilayer Lipid Membranes Based on the Avidin – Biotin Interaction

SAMs of avidin were deposited by immersing the Pt electrodes in avidin solution (10 mg mL^{-1} in PBS) and applying 200 V s^{-1} of an alternating potential with triangular waveform from -0.5 to +2.1 V (*vs*. Ag/AgCl, KCl 3.5 M) for 10 minutes. The electrode was then rinsed with PBS to remove weakly attached avidin.[14–17]

3.6. Preparation of Vesicles

3.6.1. Bilayer Lipid Membranes Modified with Bio – Electroactive Molecules

A chloroform solution of EggPC, or lipid with UQ_{10} and/or VitE, was dried in a glass vial under a slow stream of Argon to yield a thin lipid film. The vial was placed in vacuum overnight to ensure that all solvent had been removed. The dried lipid was hydrated at room temperature using HEPES buffer solution resulting in multilamellar vesicles. To obtain unilamellar vesicles the hydrated lipid was sonicated for 20 min.[4,10,18–20]

3.6.2. Bilayer Lipid Membranes Based on the Avidin – Biotin Interaction

A chloroform solution of DOPE(B) (4% molar ratio) and EggPC was dried in a glass vial under a slow stream of Argon to yield a thin lipid film. The vial was placed in vacuum overnight to ensure that all solvent had been removed. The dried lipid was hydrated at room temperature using 1 mM MB in 100 mM PBS resulting in multilamellar vesicles. To obtain small unilamellar vesicles the hydrated lipid was extruded 21 times through a membrane with 100 μm of pore diameter.

The vesicles solution was then placed in a dialysis tube (Spectra/Por® CE Float –A-Lyser® G2), the dialysis tube was then placed in a 100 mM PBS solution for 24 hours (replacing the PBS solution every 4 hours) to remove the external MB. This results in a vesicles solution that had MB inside the vesicles but not on the outside solution.

3.7. Formation of BLMs

3.7.1. Bilayer Lipid Membranes Modified with Bio – Electroactive Molecules

3.7.1.1. Tethered Bilayer Lipid Membranes

After SAM formation the electrodes were dipped in a 1 mg mL^{-1} solution of vesicles. The vesicles fuse and the bilayer is formed within a few hours. The driving force for the fusion of the vesicles is the hydrophobic interaction with the SAM.[21]

3.7.1.2. BLM Between Two Aqueous Solutions

The bilayer between two aqueous solutions (psBLM) was formed on a micropore array that consisted of 8 micropores with a diameter of 50±3 μm (Figure 4.1).[22] The psBLM was obtained by placing 20 μL of a 1 mg mL^{-1} n-decane solution of EggPC, or lipid with UQ_{10} (0.02 mM) and/or VitE (0.02 mM), on the micropore array. After drying, an additional 20 μL of the same solution was placed on the other side of the micropore array. The psBLM was formed when both sides of the micropore array came into contact with an aqueous solution.[23] The measurements were performed in a normal three electrode system, with the working electrode (Au, 0.020 cm^2) being placed in one side of the psBLM and the reference (Ag/AgCl, 3.5 M KCl) and counter (Pt flag, 1 cm^2) being placed on the other side of the psBLM (Figure 3.2). Both chambers were filled with the same working solution which contained HEPES buffer solution as background solution.

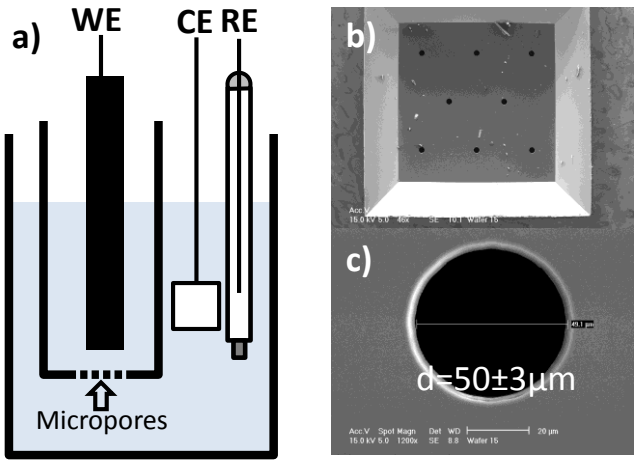

Figure 3.2 – a) Schematic representation of the experimental set-up for the psBLM. The psBLM was deposited on the micropores and it was between the working and the reference and counter electrodes. b) top view of the micropore array; the 8 pores are arranged in a hexagonal pattern. c) one of the pores of the array. The diameter is 50±3 µm.

3.7.2. Bilayer Lipid Membranes Based on the Avidin – Biotin Interaction

After the deposition of the avidin SAM the electrode was immersed in a solution 2 mg mL^{-1} of vesicles. Because of the small size of the vesicles and the lack of hydrophobic interaction, the vesicles do not burst without external interference. A potential of +0.7 V (*vs.* Ag/AgCl, KCl 3.5 M) was applied to the solution, using a second WE – figure 3.3. The BLM is formed when the vesicles burst.

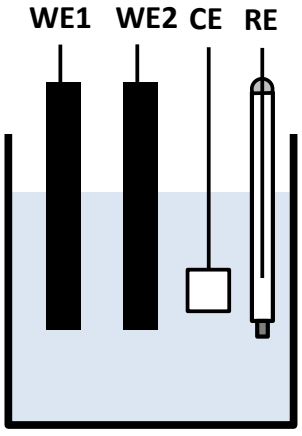

Figure 3.3 – Experimental set-up to burst the vesicles. The +0.7 V (*vs.* Ag/AgCl, KCl 3.5 M) is applied between WE2 and RE. The SAM of avidin was previously deposited in WE1 and the vesicle fusion occurs in WE1.

References

(1) Shon, Y.-S.; Colorado, R.; Williams, C. T.; Bain, C. D.; Lee, T. R. *Langmuir* **2000**, *16*, 541-548.
(2) Xing, Y. F.; Li, S. F. Y.; Lau, A. K. H.; O'Shea, S. J. *J. Electroanal. Chem.* **2005**, *583*, 124-132.
(3) Yang, M.; Zhang, Z. *Electrochim. Acta* **2004**, *49*, 5089-5095.
(4) Vockenroth, I. K.; Fine, D.; Dodobalapur, A.; Jenkins, A. T. A.; Köper, I. *Electrochem. Commun.* **2008**, *10*, 323-328.
(5) Guo, L.-H.; Facci, J. S.; McLendon, G.; Mosher, R. *Langmuir* **1994**, *10*, 4588-4593.
(6) Naumowicz, M.; Figaszewski, Z. *Bioelectrochemistry* **2003**, *61*, 21-27.
(7) Gordillo, G. J.; Schiffrin, D. J. *Faraday Discuss.* **2000**, *116*, 89-107.
(8) Cheng, Y.; Cunnane, V. J.; Kontturi, A.-K.; Kontturi, K.; Schiffrin, D. J. *J. Phys. Chem.* **1996**, *100*, 15470-15477.
(9) Moncelli, M. R.; Herrero, R.; Becucci, L.; Guidelli, R. *Biochim. Biophys. Acta, Bioenerg.* **1998**, *1364*, 373-384.
(10) Jadhav, S. R.; Sui, D.; Garavito, R. M.; Worden, R. M. *J. Colloid Interface Sci.* **2008**, *322*, 465-472.
(11) Forouzan, F.; Bard, A. J.; Mirkin, M. V. *Isr. J. Chem.* **1997**, *37*, 155-163.
(12) Schiller, S. M.; Naumann, R.; Lovejoy, K.; Kunz, H.; Knoll, W. *Angew. Chem. Int. Ed.* **2003**, *42*, 208-211.
(13) Vockenroth, I. K.; Atanasova, P. P.; Long, J. R.; Jenkins, A. T. A.; Knoll, W.; Köper, I. *Biochim. Biophys. Acta, Biomembr.* **2007**, *1768*, 1114-1120.
(14) Anzai, J.-ichi; Hoshi, T.; Osa, T. *Chem. Lett.* **1993**, *22*, 1231-1234.
(15) Anzai, J.-ichi; Hoshi, T.; Lee, S.; Osa, T. *Sens. Actuators, B* **1993**, *13*, 73-75.
(16) Hoshi, T.; Anzai, J.-ichi; Osa, T. *Anal. Chim. Acta* **1994**, *289*, 321-327.
(17) Hoshi, T.; Hiwatashi, Y.; Anzai, J.-I. *ITE Lett Batter New Technol Med* **2004**, *5*, 552-555.
(18) Barenholz, Y.; Gibbes, D.; Litman, B. J.; Goll, J.; Thompson, T. E.; Carlson, F. D. *Biochemistry* **1977**, *16*, 2806-2810.
(19) Plant, A. L. *Langmuir* **1993**, *9*, 2764-2767.
(20) Knoll, W.; Köper, I.; Naumann, R.; Sinner, E.-K. *Electrochim. Acta* **2008**, *53*, 6680-6689.
(21) He, L.; Robertson, J. W. F.; Li, J.; Kärcher, I.; Schiller, S. M.; Knoll, W.; Naumann, R. *Langmuir* **2005**, *21*, 11666-11672.
(22) Zazpe, R.; Hibert, C.; O'Brien, J.; Lanyon, Y. H.; Arrigan, D. W. M. *Lab Chip* **2007**, *7*, 1732-1737.
(23) Steinem, C.; Janshoff, A.; Ulrich, W.-P.; Sieber, M.; Galla, H.-J. *Biochim. Biophys. Acta, Biomembr.* **1996**, *1279*, 169-180.

4. Self-Assembled Monolayers on Au (111)

Self-assembled monolayers (SAMs) have received increased attention throughout the decades due to their wide range of application. In this chapter a comparison between SAMs of alkanethiols (1-heptanethiol and 1-dodecanethiol) and SAMs of thiolipids (1,2-dipalmitoyl-*sn*-glycero-phosphothioethanol (DPPTE) and a mixture of DPPTE and L-α-phosphatidylcholine (EggPC)) is made. Characterisation of the SAMs was made using cyclic voltammetry and electrochemical impedance spectroscopy (EIS); the kinetic parameters of the SAMs were determined based on the EIS measurements. Both DPPTE and DPPTE+EggPC SAMs are of good quality although the later presents better kinetic parameters. The comparison between the DPPTE and DPPTE+EggPC SAM is made to evaluate which should be used to produce tethered bilayer lipid membranes.

4.1. Introduction

The origins of self-assembled monolayers can be dated back to 1st century AD when Pliny the Elder observed that the sailing of a ship was different when greasy material was spread on the water surface.[1,2] Benjamin Franklin observed the same in 1757 when he was travelling to London.[3] After that he did experiments by dropping oil on water, he observed that the oil spreads itself and that the waves are influenced by the oil. He said that the size of the molecules could be determined if the layer formed by the oil is a

monolayer with the thickness of a molecule.[1] In 1890, Lord Rayleigh repeated Franklin's oil experiment and calculated the thickness of the oil layer.[4] Around the same time he helped Agnes Pockels to publish her pioneering surface tension measurements in *Nature*.[5]

The work developed by Agnes Pockels was the basis for the studies done by Irwing Langmuir on films and surface adsorption. In 1917 he introduced the concept of monolayer and the 2D physics that described a surface. His work in surface chemistry was the reason why he was awarded with the Nobel Prize in 1932.[6] In the work that leads to Langmuir's Nobel Prize he was assisted by Katherine Blodgett. This collaboration gave origin to the well-known Langmuir-Blodgett trough.

In 1946, monomolecular layers of surfactants on a metal substrate were prepared by Zisman et al. leading to the concept of self-assembled monolayer (SAM). They reported that eicosyl alcohol ($C_{20}H_{41}OH$) formed hydrophobic surfaces on platinum, nickel, copper, gold and other metals.[7] This has received more interest in the last 30 years mainly due to the work of Nuzzo and Allara at Bell Laboratoires; they showed that monolayers of *n*-disulphides could be prepared on gold by spontaneous adsorption.[8]

Self-assembled monolayers consist on a spontaneous organization of amphiphilic molecules based in the interactions between the substrate and the molecules[9]; this is a thermodynamically driven process resulting in stable structures in ambient conditions.[10] The interaction between the substrate and the molecules can be i) covalent – silane monolayers in oxide surfaces; ii) electrostatic – fatty acids on silver; or iii) chemisorption – thiols on gold.[2]

Figure 4.1 is the schematic representation of the interactions between a molecule and the substrate. The molecule consists of a head group attached to the substrate, an alkyl chain

as interior group which provides cohesive interactions and a terminal group which interacts with the ambient.[2]

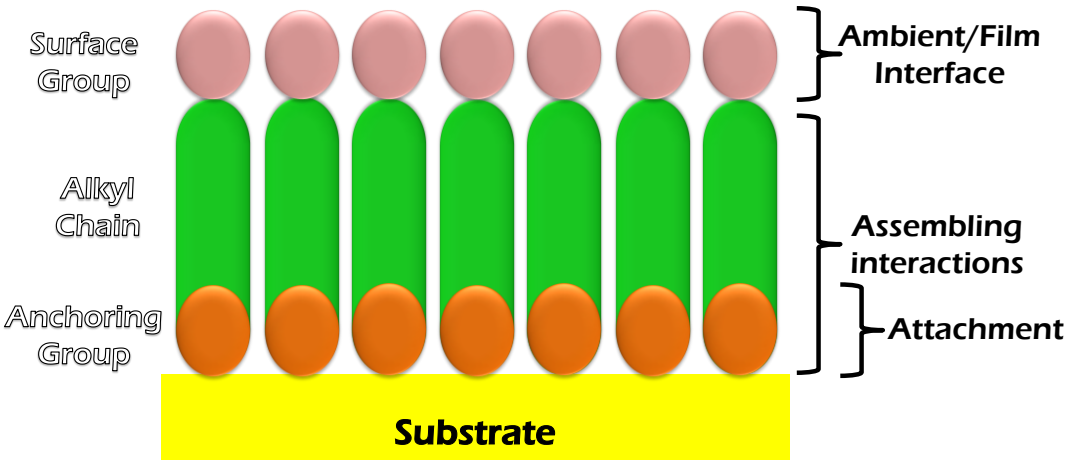

Figure 4.1 – Schematic view of the self-assembling of an amphiphilic molecule on a substrate.

The interaction between the molecule and the substrate can be analysed from the energetic point of view. In the case of thiols on gold, the chemisorption of the sulphur group to the gold, covalent bond, represents around 50 kcal mol^{-1}; the interactions among the alkyl chain, van der Waals and hydrophobic forces, 1–2 kcal mol^{-1} per methylene unit; the terminal group interacts with the ambient, and in the case of a simple alkyl chain the terminal methyl group (CH_3) provides a hydrophobic surface, and contributes with only a few kT*.[10–12]

4.1.1. General aspects of thiol SAMs on gold

Self-assembled monolayer of thiols on gold can be prepared using many molecules. In figure 4.2 are some of the most used molecules to prepare this type of monolayer. This type of structure has been widely used in the last three decades mainly due to their wide range of application; these structures can be used in nano and microfabrication,

* 1 T (Talbot)= 1.464 mJ (@555 nm)

nanodevices and molecular electronics, wetting, molecular recognition and biomimetic systems.[12]

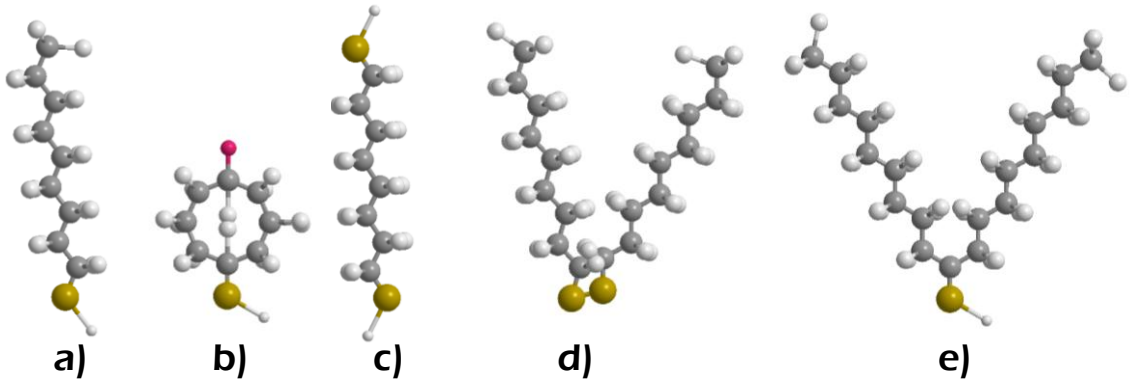

Figure 4.2 – Some examples of molecules that form self-assembled monolayers on gold. a) alkanethiol, b) arenethiol, c) alkanedithiol, d) dialkyldisulfide, e) dialkylsulfide. Yellow: S atom, grey: C atom, white: H atom, Pink: indicates possible modification.

Gold is one of the most used substrates to prepare SAMs because of its inertness, the tendency to form oxide is not strong and the interaction between gold and sulphur is strong.[11,13] This interaction can be seen as an oxidative addition of the S–H bond to the gold surface:[13,14]

$$R - S - H + Au_n^0 \longrightarrow R - S^- Au^+ + {}^1/_2\, H_2$$

What happens to the H of the S–H bond is still undetermined. The most likely fate, in solution, is that it is lost in the form of H_2. Another possibility is that the presence of oxygen in the reaction medium might lead to its oxidative conversion to water.[11]

Ulman and co-workers[15] used simulations to determine the orientation and packing of alkanethiol monolayers on gold surfaces. They suggested that the S···S spacing, 4.97Å, previously reported by Strong and Whitesides[16] may result from S–Au interfacial interactions and from neighbour–neighbour interactions energy in the hexagonal assembly of the alkyl chain. They also suggested that there is no free rotation in the tilted

alkanethiol chain, because when the monolayer is closely packed the chains encounter an energy barrier for rotation. From the molecular dynamics simulations they reported that the tilt angle is ca. 30° and furthermore, that this angle has specific values determined by the spacing and orientation of the head groups.

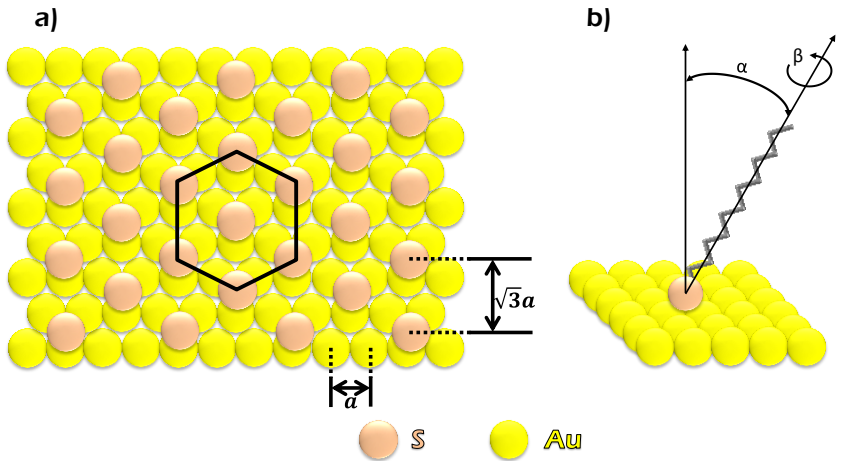

Figure 4.3 – Schematic representation of the arrangement of alkanethiols on an Au (111) surface. a) Top view of the structure of SAMs of alkanethiols on Au (111) lattice when maximum coverage is attained. The arrangement shown is a (√3x√3)R30° structure where the sulphur atoms (orange circles) are positioned in the 3-fold hollows of the gold lattice (yellow circles, a=2.88 Å). The alternating orientation of the alkane chains defines the c(4x2) structure. The hexagonal (√3x√3)R30° is highlighted. b) Stand up configuration, the typical angles are: α = 30° and β = 55°. β is the twist angle which defines the rotation of the carbon chain backbone about the chain axis with respect to the plane defined by the chain axis and the surface.

Electron diffraction, STM, helium diffraction and AFM studies showed that the symmetry of sulphur atoms is hexagonal, it forms a (√3x√3)R30° overlayer with a c(4x2) superlattice on Au(111) as shown in figure 4.3 a).[13,17–19]

4.1.2. The self-assembly process

The self-assembly processes consists on the assembly without external interference. Because SAMs represent a path to link inorganic, organic and biological materials, they

have been used in bottom-up fabrication technologies. Hence, the understanding of self-assembly from the kinetic and the structural points of view is relevant.[12]

Self-assembly of thiols on gold, mainly Au (111), has been studied for many years and is well understood. One very important characteristic of the SAMs is that they have to be compact enough so that electrochemical processes will be suppressed.[20] To form a compact monolayer the alkyl chain should have, at least, 9 carbons, otherwise pinholes may be observed and the surface is not hydrophobic enough to block electron transfer between the medium and the gold substrate.[21–23] Ultrahigh vacuum STM studies reported that SAMs of alkanethiols with less than 8 carbons present a two-dimensional (2D) liquid phase. This liquid phase was not observed in alkanethiols with 8 or more carbons.[13]

The adsorption of alkanethiols on Au (111) is a very fast process, although the structure formed is not well ordered or compact. A good SAM usually takes 12-24 h to form. This process can be divided in 4 steps as illustrated in figure 4.4. The initial adsorption (Steps 1 and 2) covers ~80% of the substrate.[11,24] The molecules then stand-up and organize themselves to lower the overall surface energy, leading to the creation of a good quality SAM (steps 3 and 4).[11]

Ethanol, because it solvates a variety of alkanethiols and is available in high purity, is the most commonly used solvent for alkanethiols. Other solvents can be used and the effect of the solvent on the self-assembling process is complex and poorly understood. It has been shown that lower chain solvents present a higher initial adsorption rate.[11] However, it has been suggested that the use non-polar solvents, e.g. heptane or hexane, might lead to a faster SAM formation but the structure formed is less organized.[11,25,26]

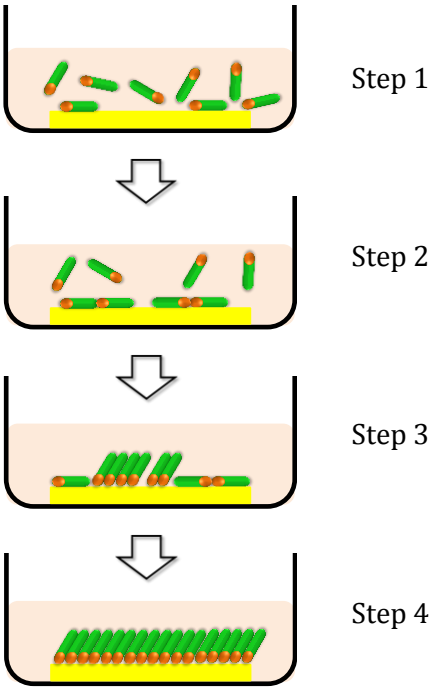

Figure 4.4 – Scheme of the formation of a SAM of alkanethiol in Au (111).

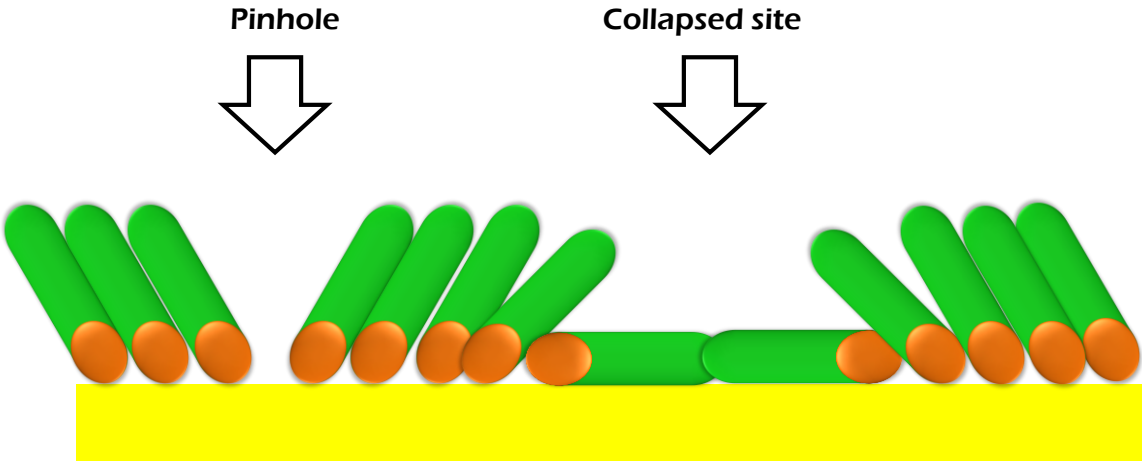

Figure 4.5 – Schematic representation of anomalies that might occur in SAM formation. A pinhole is formed when there is a part of the substrate that is not covered by the alkanethiol, defects are formed when the alkanethiol do not stay in the upright position.

As previously mentioned, monolayers of alkanethiols on gold are characterised by their high structure order, compactness and stability.[27] However there is the possibility of

formation of pinholes and/or defects, figure 4.5. Pinholes can be attributed to the roughness of the substrate.[27,28]

4.1.3. Characterisation and application of SAMs

Electrochemical studies of heterogeneous electron transfer through SAMs were pioneered by Porter et al.[29] and Finklea et al.[20,30] Porter and co-workers used alkanethiols with different chain lengths ($CH_3(CH_2)_nSH$ with n=1, 3, 5, 7, 9, 11, 15, 17 and 21) and concluded that for n>11 the SAMs were adequate to study electron transfer, ion transport and double-layer phenomena. They concluded that only long chain alkanethiols were adequate to these studies because they form pinhole free organized films, short chain alkanethiols do not form organized films in the electrode surface. Finklea and co-workers showed the presence of pinholes and collapsed sites in SAMs of long hydrocarbon chains (C_{12} to C_{18}).[20] Later, using CV and ac impedance spectroscopy in SAMs of octadecanethiol, the pinholes were analysed in terms of resembling the behaviour of a microelectrode array.[30] One point in which the authors agree is that the cleanliness of the substrate and mode of preparation has an influence in the quality of the films produced.[20,29,30]

Cyclic voltammetry and electrochemical impedance spectroscopy form the "perfect couple" for electrochemical SAM characterisation. Because in EIS only very small sinusoidal potential sweeps are applied, over a range of frequencies, this makes it a less disturbing technique than CV. Using redox couples as probe molecules, a conjugation of CV and EIS evaluates the presence of pinholes and/or defects in the SAM. This allows the determination of kinetic parameters and surface coverage.[21–23,30–33]

In the studies of electron transfer done by Porter and Finklea the electroactive species was in the electrolyte solution, another way to do this type of studies is with the

electroactive species attached to the monolayer. Examples of this type of work are monolayers of ferrocene terminated alkanethiols.[34,35]

The study of electron transfer through SAMs has attracted much interest because they provide a model to study electron transfer of more complex structures. SAMs are stable and structurally well-defined and with the possibility to tune characteristics such as thickness and function they provide a model to study more complex structures, e.g. the study of long-range electron transfer has particular interest for biological systems.[36,37]

Self-assembled monolayers of alkanethiols have also been used as lower leaf in tethered bilayer lipid membranes.[27,38,39] In this chapter we compare SAMs of a thiolipid, 1,2-dipalmitoyl-*sn*-glycero-phosphothioethanol (DPPTE) and SAMs of a thiolipid mixed a phosphatidylcholine lipid, DPPTE+L-α-phosphatidylcholine (DPPTE+EggPC), with two alkanethiols, 1-dodecanethiol (DDT) and 1-heptanethiol(HPT) (figure 4.6 a) to d), respectively).

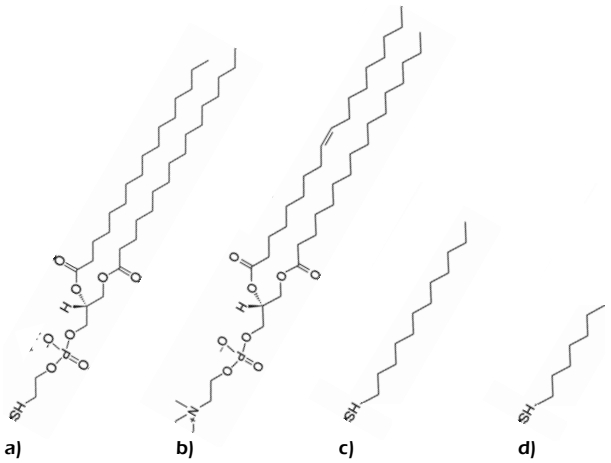

Figure 4.6 – Molecules used to produce the SAMs studied in this chapter. a) DPPTE, b) EggPC, c) DDT and d) HPT. In the case of the thiolipid SAM a mixture 2:1 of DPPTE:EggPC was used. The EggPC is used to fill possible gaps between the DPPTE molecules, leading to a better quality SAM.[40]

4.2. Discussion

Cyclic voltammetry and electrochemical impedance spectroscopy were used to characterise the blocking properties of the SAM modified gold electrodes. The SAMs were characterised in solutions containing 0.5 mM $Fe(CN)_6^{3-}$ + 0.5 mM $Fe(CN)_6^{4-}$, using KNO_3 as background electrolyte, over a potential range of -0.2 to +0.7 V (vs. Ag/AgCl, KCl 3.5 M). All measurements were made in degassed solutions and at room temperature.

4.2.1. Cyclic Voltammetry

Figure 4.7 shows the typical cyclic voltammogram for the bare electrode. The electron transfer is very facile, thus the peak shape observed. HPT is a short chain alkanethiol and its SAM does not completely supress the redox reaction on the electrode surface. The behaviour presented in figure 4.8 is similar to that of a microelectrode, cyclic voltammogram with sigmoidal shape rather than with the peak shape observed for the bare electrode (figure 4.7).

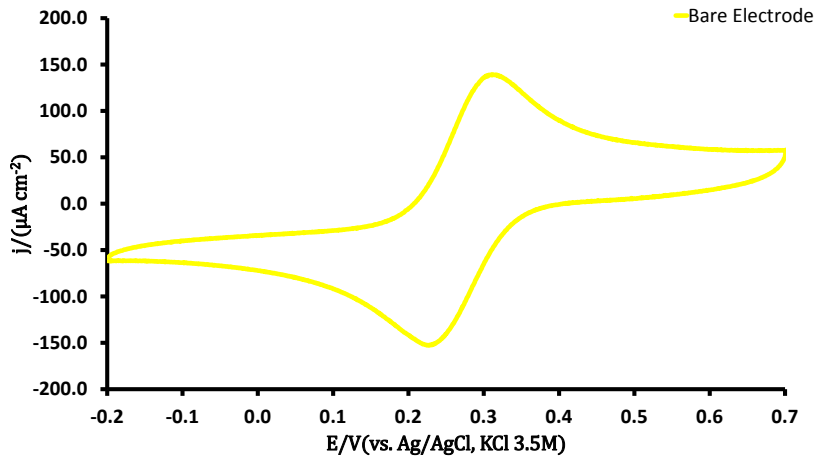

Figure 4.7 – CV of bare Au(111) electrode in 0.5 mM $Fe(CN)_6^{3-}$ + 0.5 mM $Fe(CN)_6^{4-}$, with 100 mM KNO_3 as background electrolyte, obtained for scans between -0.2 to +0.7V (vs. Ag/AgCl, KCl 3.5M) at 50 mV s^{-1}.

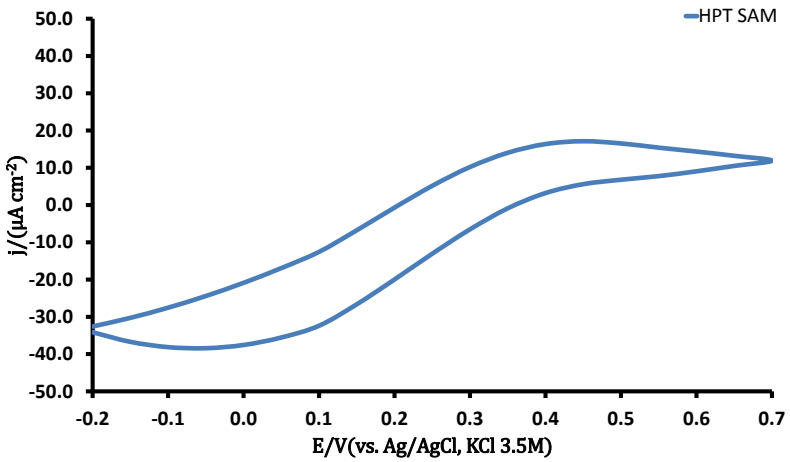

Figure 4.8 – CV of HPT SAM in 0.5 mM $Fe(CN)_6^{3-}$ + 0.5 mM $Fe(CN)_6^{4-}$, with 10 mM KNO_3 as background electrolyte, obtained for scans between -0.2 to +0.7 V (vs. Ag/AgCl, KCl 3.5 M) at 50 mV s^{-1}.

The voltammogram shown in figure 4.8 indicates the existence of pinholes in the SAM. The shape of the voltammogram indicates a quasi – microelectrode behaviour; the pinholes are small but not separted enough so their diffusion layers overlap. The electron transfer takes place by diffusion of the electroactive species through the pinholes formed; the electroactive species approaches the electrode surface through the pinholes, followed by electron transfer, thus presenting radial diffusion of the redox species and not linear diffusion as in the case of the bare electrode. If the pinholes were big or if the diffusion layers were heavily overlapping the voltammogram should clearly show the oxidation and reduction peaks, on the other hand if the pinholes were separated enough so that there was no diffusion layer overlapping the voltammogram should show a behaviour similar to that of a microelectrode.[41–43]

In contrast, the absence of any peak in the CVs of DDT (figure 4.9), DPPTE (figure 4.10) and DPPTE+EggPC (figure 4.11) indicates that the redox reaction is completely inhibited, implying the formation of a pinhole free monolayer.

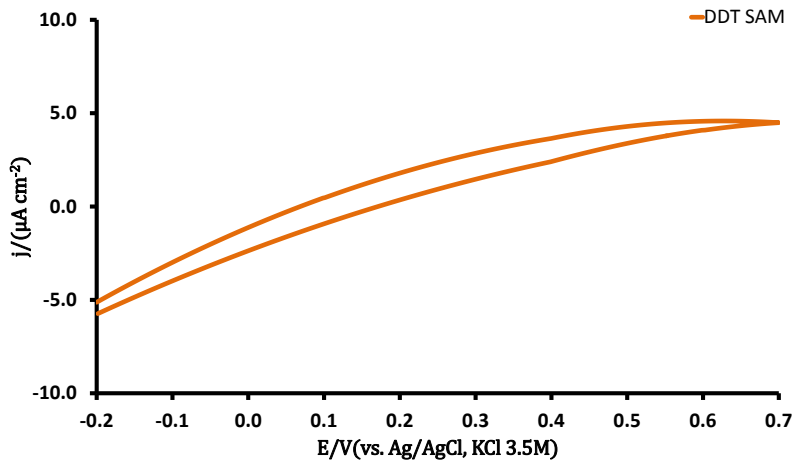

Figure 4.9 – CV of DDT SAM in 0.5 mM $Fe(CN)_6^{3-}$ + 0.5 mM $Fe(CN)_6^{4-}$, with 100 mM KNO_3 as background electrolyte, obtained for scans between -0.2 to +0.7 V (vs. Ag/AgCl, KCl 3.5 M) at 50 mV s^{-1}.

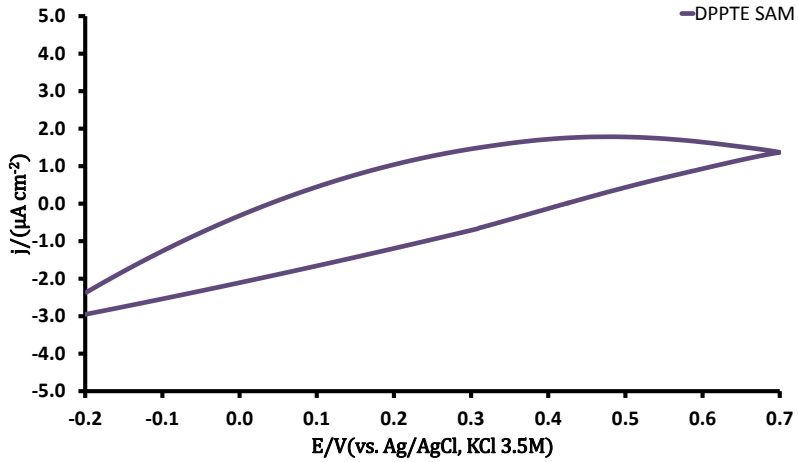

Figure 4.10 – CV of DPPTE SAM in 0.5 mM $Fe(CN)_6^{3-}$ + 0.5 mM $Fe(CN)_6^{4-}$, with 100 mM KNO_3 as background electrolyte, obtained for scans between -0.2 to +0.7 V (vs. Ag/AgCl, KCl 3.5 M) at 50 mV s^{-1}.

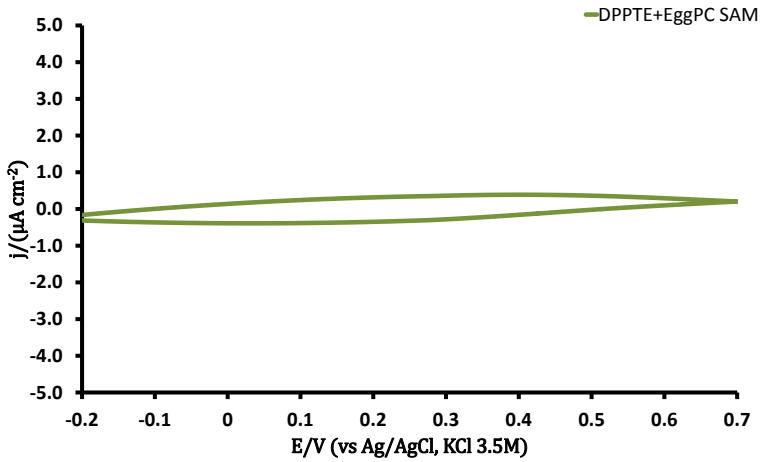

Figure 4.11 – CV of DPPTE+EggPC SAM in 0.5 mM $Fe(CN)_6^{3-}$ + 0.5 mM $Fe(CN)_6^{4-}$, with 100 mM KNO_3 as background electrolyte, obtained for scans between -0.2 to +0.7 V (vs. Ag/AgCl, KCl 3.5 M) at 50 mV s^{-1}.

Although the redox peaks are completely suppressed that does not implicate that the film formed does not have defects. CV does not give information about possible defects in the film. As previously mentioned, Finklea and co-workers[20] have suggested that monolayers may contain both defects and collapsed sites (figure 4.5), resulting in the redox molecule approaching the electrode surface in the defective areas but not come in direct contact with the electrode surface. They attributed these sites as an explanation to the anomalous low Tafel slopes observed in the case of monolayers that behave like microelectrode arrays.

To analyse the quality of the films formed and the possibility of electron tunnelling, electrochemical impedance spectroscopy measurements were performed.

4.2.2. Electrochemical Impedance Spectroscopy

Electrochemical impedance spectroscopy is a powerful tool for estimating the structural integrity of a monolayer. Impedance measurements were made at the equilibrium potential of the redox couple, $Fe(CN)_6^{3-/4-}$ ($E^{0'}$=+0.225 V vs. SCE), at a wide range of frequencies from 1.0×10^5 to 1 Hz, with a perturbation of 10 mV in the potential. The

electrolyte solution contained 0.5 mM $Fe(CN)_6^{3-}$ + 0.5 mM $Fe(CN)_6^{4-}$, and 0.1 M KNO_3, background.

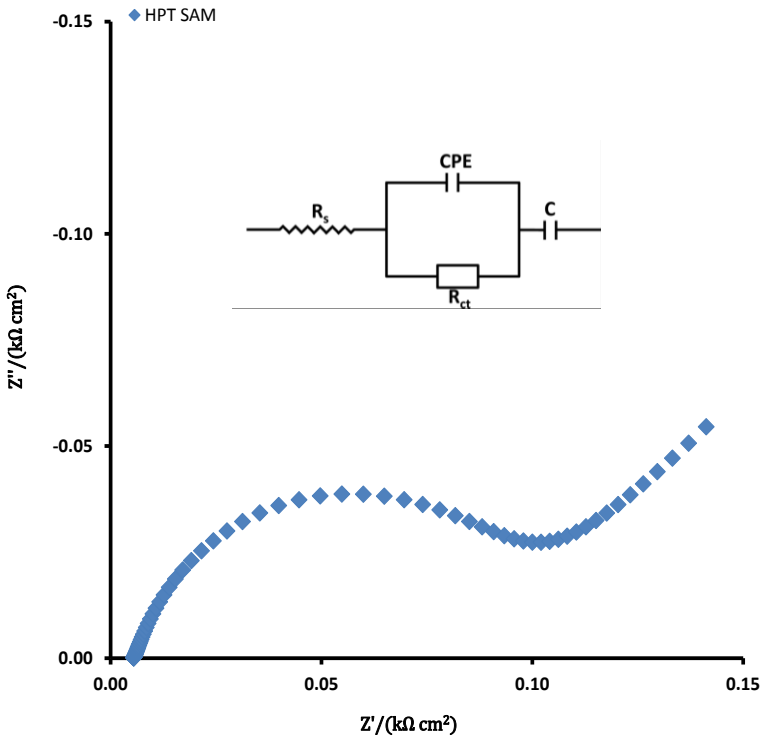

Figure 4.12 – Nyquist plot of HPT SAM in 0.5 mM $Fe(CN)_6^{3-}$ + 0.5 mM $Fe(CN)_6^{4-}$, with 100 mM KNO_3 as background electrolyte, measurement at open circuit potential obtained for frequencies between 1.0×10^5 to 1 Hz. The inset represents the equivalent circuit used to fit the experimental data.

The Nyquist plot for the HPT SAM (figure 4.12) shows a semi-elliptical shape at the high frequency region and a straight line at the low frequency region, implying a poor blocking ability of the monolayer, which supports the observations made using cyclic voltammetry. A semi-elliptical shape at the high frequency region, described by a resistance (charge transfer control) in parallel with a capacitor (electrode/SAM double layer) indicates the redox reaction is kinetically controlled, and a 45° straight line at the low frequency region represents the Warburg region of semi-infinite and mass-transfer controlled electron transfer.

In the case of the DDT SAM (figure 4.13), DPPTE (figure 4.14) and DPPTE+EggPC SAM (figure 4.15) the impedance spectra show a semielliptical shape in the entire frequency range, indicating complete charge transfer control for the redox reactions. This behaviour is representative of a well assembled and pinhole free monolayer.

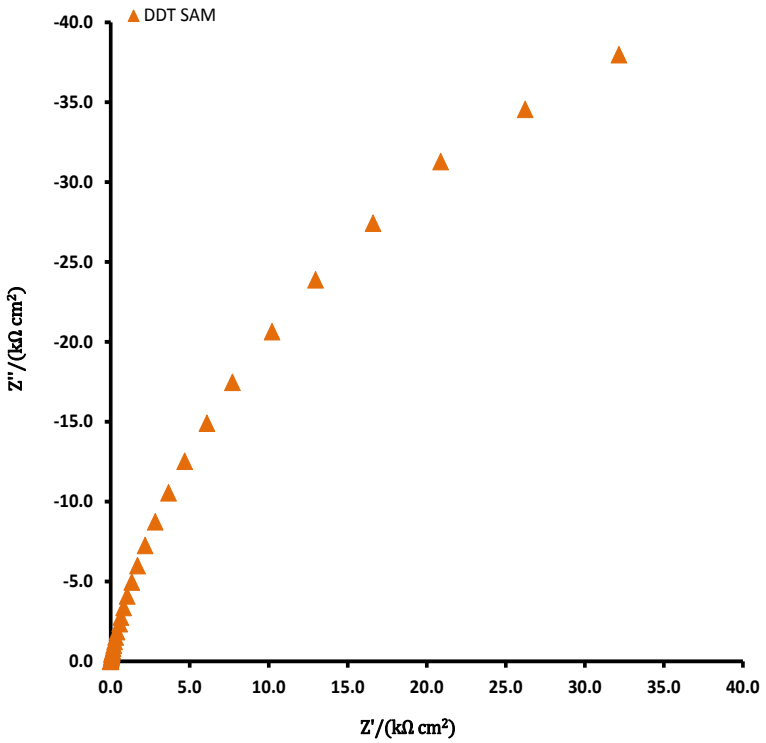

Figure 4.13 – Nyquist plot of DDT SAM in 0.5 mM $Fe(CN)_6^{3-}$ + 0.5 mM $Fe(CN)_6^{4-}$, with 100 mM KNO_3 as background electrolyte, measurement at open circuit potential obtained for frequencies between 1.0×10^5 to 1 Hz.

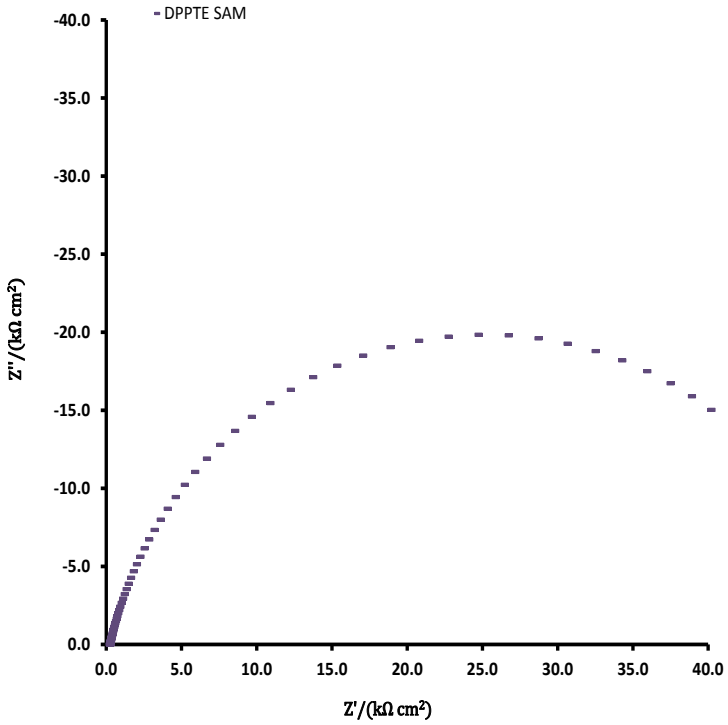

Figure 4.14 – Nyquist plot of DPPTE SAM in 0.5 mM $Fe(CN)_6^{3-}$ + 0.5 mM $Fe(CN)_6^{4-}$, with 100 mM KNO_3 as background electrolyte, measurement at open circuit potential obtained for frequencies between 1.0×10^5 to 1 Hz.

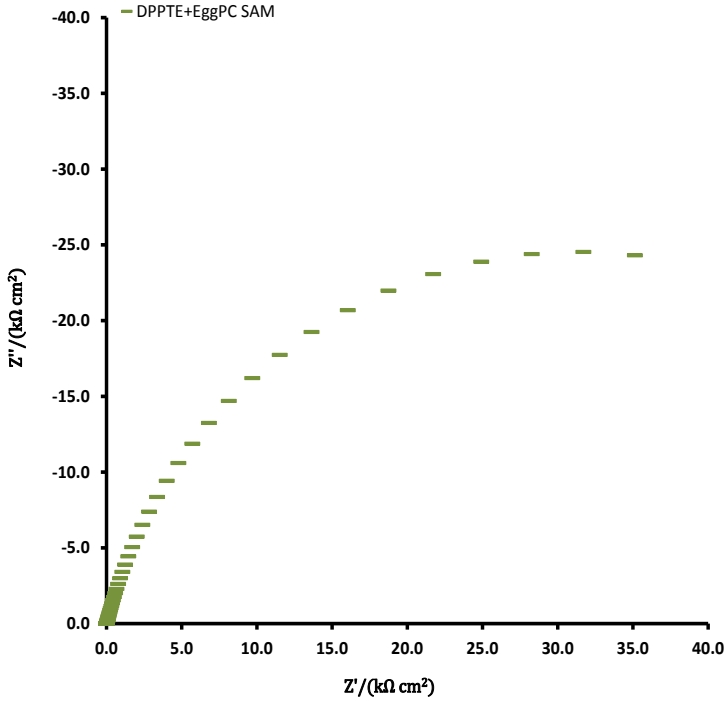

Figure 4.15 – Nyquist plot of DPPTE+EggPC SAM in 0.5 mM $Fe(CN)_6^{3-}$ + 0.5 mM $Fe(CN)_6^{4-}$, with 100 mM KNO_3 as background electrolyte, measurement at open circuit potential obtained for frequencies between 1.0×10^5 to 1 Hz.

4.2.3. Electron Transfer Kinetics

Cyclic voltammetry and EIS measurements have shown the presence of pinholes in the HPT SAM. However the existence of defects/collapsed sites in all the SAMs formed needs to be probed further as these influence the electron transfer kinetics. A comparison of Marcus theory and experimental data is used to investigate this phenomenon.[44–46]

If there are no pinholes in the SAM the mechanism for electron transfer is tunnelling across the film.[44–46] In this case the Faradaic current should, at any potential, decrease exponentially with the film thickness according to the equation[47]

$$\mathrm{i} = \mathrm{i}_\mathrm{b}^0 \exp(-\beta \mathrm{d}) \qquad (4.1)$$

where i_b^0 is the current measured at bare electrode, d is the thickness of the film and β is the potential independent electron tunnelling coefficient. The parameter β is a measure of the magnitude of current lost per unit length of each molecule, which can vary from approximately 0 Å^{-1} for metals to 3.5 Å^{-1} close to vacuum.[45,48,49] In the work here presented the values of β used were 0.87 Å^{-1} for the alkanethiols[50] and 0.72 Å^{-1} for the lipids.[51]

When the electrochemical reaction is at equilibrium and the concentrations of oxidised and reduce species are equal, the exchange current (i_b^0) and the standard electron transfer rate constant (k_b^0) at a bare electrode, can be written as:

$$i_b^0 = nFAk_b^0 c \qquad (4.2)$$

where c is the concentration of the redox couple in the bulk electrolyte. Using equations 4.1 and 4.2, the exchange current due to tunnelling in the presence of a monolayer (i_t^0) is given by:[45,52]

$$\mathrm{i}_\mathrm{t}^0 = \mathrm{nFAk}_\mathrm{b}^0 \mathrm{cexp}(-\beta \mathrm{d}) \qquad (4.3)$$

Assuming that all the defects act independently and that θ_m represents the fractional coverage of defects in a film with thickness d_m, the tunnelling exchange current at the defects, $i^0_{t,m}$, can be represented as:

$$i^0_{t,m} = nF\theta_m Ak^0_b c\exp(-\beta d_m) \qquad (4.4)$$

$$1 \leq m \leq d_0$$

where d_0 is the film thickness of a well formed monolayer.

Based on the assumption that there is no concentration polarisation at the defects, Diao and co-workers[45,52] proposed that the apparent exchange current observed at modified electrodes (i^0_{app}) is the sum of all the tunnelling currents at defects with different film thickness. However, the fractional coverage of each type of defect is hardly measurable. It is therefore necessary to use a concept of average fractional coverage to obtain the equation:

$$i^0_{app} = nFAk^0_{app} c \qquad (4.5)$$

where k^0_{app} is the apparent electron transfer rate constant taking into consideration the fact that only an apparent exchange current is measurable

$$i^0_{app} = i^0_1 + i^0_2 + \cdots + i^0_m + \cdots + i^0_{d_0} \qquad (4.6)$$

Inserting equations 4.4 and 4.5 into equation 4.6, for n=1, gives:

$$\theta_1 \exp(-\beta d_1) + \theta_2 \exp(-\beta d_2) + \cdots + \theta_m \exp(-\beta d_m) + \cdots$$

$$+ \theta_0 \exp(-\beta d_0) = \frac{k^0_{app}}{k^0_b} \qquad (4.7)$$

$$\theta_1 + \theta_2 + \cdots + \theta_m + \cdots + \theta_0 = 1 \qquad (4.8)$$

giving

$$k_{app}^{0} = k_{b}^{0}\left[\theta_a \exp(-\beta d_a) + \sum_{i=0}^{i=m} \theta_i \exp(-\beta d_0)\right] \qquad (4.9)$$

where,

θ_a is the fractional coverage of a monolayer,

d_a is the average film thickness of a monolayer,

θ_i is the fractional coverage for defects with film thickness d_i,

d_0 is the ideal film thickness.

Equation 4.7 can be rewritten as:

$$\theta_a \exp(-\beta d_a) + \theta_0 \exp(-\beta d_0) = \frac{k_{app}^{0}}{k_b^{0}} \qquad (4.10)$$

with

$$\theta_0 = 1 - \theta_a \qquad (4.11)$$

Simplifying:

$$\theta_a = \frac{\left(\frac{k_{app}^{0}}{k_b^{0}} - \exp(-\beta d_0\right)}{(\exp(-\beta d_a) - \exp(-\beta d_0))} \qquad (4.12)$$

The value of the fractional coverage, θ_a, gives an estimate of the presence of defects in the film. When $\theta_a = 1$, d_a represents the average film thickness of the whole monolayer (ATWM). An ATWM value close to d_0 imply a well-assembled, defect free monolayer.

Under equilibrium conditions[45] and with the reorganization energy being independent of the distance[53], the theoretical standard tunnelling rate constant, k_{th}^{0}, can be written as:

$$k_{th}^{0} = k_{b}^{0} \exp(-\beta d) \qquad (4.13)$$

If all the current is due to tunnelling, the theoretical electron transfer rate for a SAM can be determined applying equation 4.13. Where k_b^0 is the standard electron transfer rate constant (0.031 cm s^{-1} for the redox couple $Fe(CN)_6^{3-/4-}$). [45]

The value of d used in equations 4.1 and 4.13 can be given by[51,54]

$$d = \frac{\varepsilon \varepsilon_r}{C_{layer\ ocp}} \qquad (4.14)$$

where ε is the vacuum permittivity (8.85E-14 F cm^{-1}), ε_r is the relative dielectric constant within the hydrocarbon region of the film (values of around 2 are usually used[54]), $C_{layer\ ocp}$ is the normalised membrane capacitance.

Electrochemical methods, in which large overpotentials are applied to the SAM coated electrode, were previously[20,55] applied in the determination of k_{app}^0 (which represents the effect of defects on the apparent electron transfer rate). Finklea and co-workers[20] reported that current due to defects was only significant at low overpotentials while Becka and Miller[55] did not observed perturbation, due to defects, on the kinetic measurements with ω-hydroxy thiol monolayers. Diao and co-workers[45] took a different a approach and used EIS measurements at open circuit potential to study the effect of defects on the SAM, this is the same approach that is used in the work here presented. Using this method, the apparent electron rate transfer can be obtained by the following equation:[45,56]

$$k_{app}^{0} = \frac{RT}{n^2 F^2 c R_{ct} A} \qquad (4.15)$$

where R is the gas constant, T is the temperature, F is the Faraday constant, c is the concentration of the redox couple, R_{ct} is the charge-transfer resistance and A the geometric area of the electrode.

The charge-transfer resistance (R_{ct}) and capacitance (C_{layer}) for the SAM electrodes were extracted by fitting an equivalent circuit to the EIS data. In the equivalent circuit a constant phase element (CPE) was used instead of a capacitor to account for the imperfections on the substrate surface.

A comparison between the experimental and theoretical electron transfer rate constants (table 4.1) shows a difference of two orders of magnitude for HPT. This confirms the presence of pinholes in the SAM as shown by CV (figure 4.8) and EIS (figure 4.12). For DDT, DPPTE and DPPTE+EggPC SAMs the difference is much smaller and can be attributed to the presence of defects in the films.

Table 4.1 – Normalized capacitance, thickness, theoretical standard tunnelling rate constant, normalized charge transfer resistance and apparent electron rate transfer for the different SAMs in 0.5 mM $Fe(CN)_6^{3-}$ + 0.5 mM $Fe(CN)_6^{4-}$, with 100 mM KNO_3 as background electrolyte, measurements at open circuit potential.

	$C_{layer\ ocp}$/(μF cm^{-2})	d/nm[a]	k_{th}^0/(cm s^{-1})[b]	R_{ct}/(KΩ cm^2)	k_{app}^0/(cm s^{-1})[c]
HPT	2.18±0.20	0.84±0.10	(1.99±0.17)x10^{-5}	0.10±0.01	(2.59±0.15)x10^{-3}
DDT	1.27±0.12	1.45±0.12	(1.05±0.10)x10^{-7}	86.54±4.20	(3.08±0.15)x10^{-6}
DPPTE	1.23±0.16	1.50±0.13	(6.32±0.55)x10^{-7}	50.05±3.90	(5.24±0.52)x10^{-6}
DPPTE+EggPC	1.12±0.10	1.70±0.14	(1.45±0.15)x10^{-7}	60.51±4.01	(4.13±0.32)x10^{-6}

[a] – calculated using equation 4.14 [b] – calculated using equation 4.13 [c] – calculated using equation 4.15

One other way to evaluate the quality of the films formed is using equation 4.12. Assuming $\theta_a = 1$, if d_a is close to d_0 that means that the film is quasi defect free.[45] From figure 4.16 and table 4.2 can be concluded that DDT, DPPTE and DPPTE+EggPC form good monolayers while HPT forms a poor quality SAM. The presence of pinholes in the HPT

monolayer is confirmed by the fact that Θ_a is > zero even when $d_a = 0$. The closer k^0_{app} is to k^0_{th}, the closer the maximum average thickness to the ideal value.

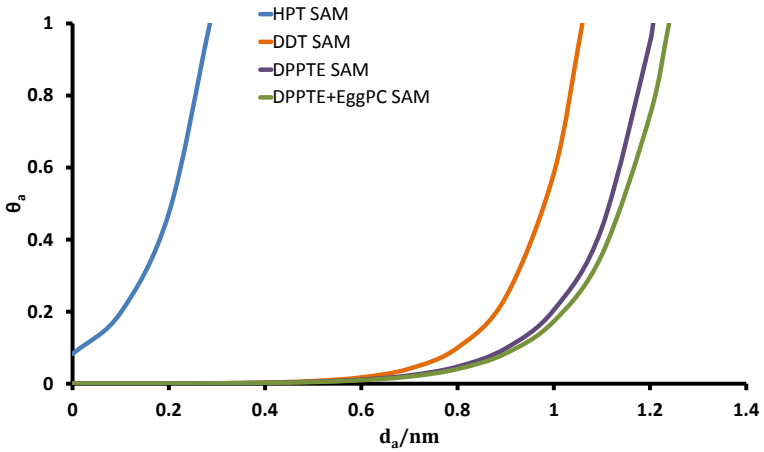

Figure 4.16 – Θ_a vs d_a plots of SAMs of HPT, DDT, DPPTE and DPPTE+EggPC on gold electrodes using equation 4.12.

Table 4.2 – Comparison between d_0 and d_a for the different SAMs formed.

	d_0/nm	d_a/nm
HPT	0.84±0.10	0.29±0.02
DDT	1.45±0.12	1.06±0.10
DPPTE	1.50±0.13	1.21±0.11
DPPTE+EggPC	1.70±0.14	1.24±0.11

4.2.4. Influence of the Applied Potential

From CV and EIS measurements and from the determination of electron transfer kinetics has been established that DDT, DPPTE and DPPTE+EggPC SAMs are pinhole free and quasi defects free. On bare electrodes, EIS measurements away from the OCP of the redox couple result in either the oxidised or the reduced species becoming very dilute making EIS measurements difficult to interpret. However, in the presence of a well assembled film, electron transfer rates are much slower. Consequently, the variations in the

concentration of the redox species are minimised, allowing meaningful EIS measurements.[57]

EIS measurements were made while superimposing a DC potential over the range of -0.2 V to +0.7 V (*vs.* Ag/AgCl, KCl 3.5 M). These results revealed that, although the monolayer capacitance remained approximately constant, the charge transfer resistance changed with potential (figures 4.17 to 4.19), this may be due to conformational changes which allow ion penetration.[57,58] The experimental data was fitted to the following equation

$$R_{ct} = R_{ct\,ocp} \exp\left[-\gamma\left(E_{app} - E_{ocp}\right)\right] \qquad (4.16)$$

where R_{ct} is the charge transfer resistance at the applied potential (E_{app}), $R_{ct\ ocp}$ is the charge transfer resistance at open circuit potential (E_{ocp}) and γ is the growth factor (negative overpotentials) or the decay factor (positive overpotentials). When overpotentials were applied the growth factor was 2.7 V^{-1}, 2.1 V^{-1} and 6.4 V^{-1} for DDT, DPPTE and DPPTE+EggPC SAMs, respectively; the decay factor was, in the same order, 2.5 V^{-1}, 1.6 V^{-1} and 4.9 V^{-1}.

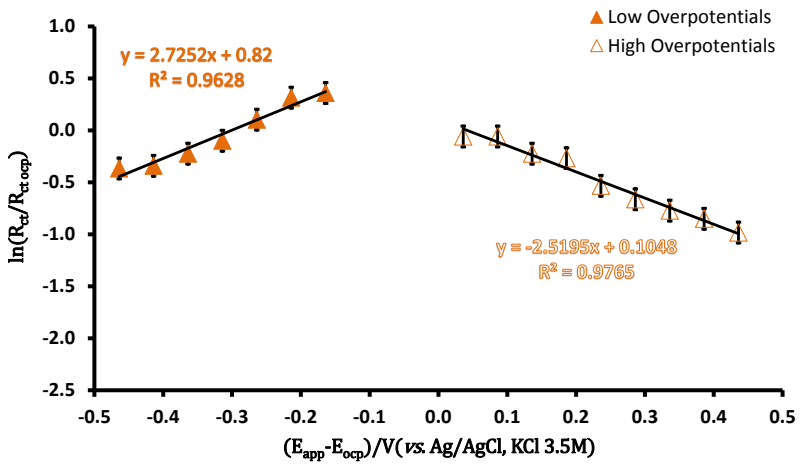

Figure 4.17 – Variation of the charge transfer resistance of the DDT SAM at different applied overpotentials. The solid marker is for negative overpotentials and the empty marker is for positive overpotentials. DDT SAM presents a growth factor of 2.7 V^{-1} and a decay factor of 2.5 V^{-1}, according to equation 4.16.

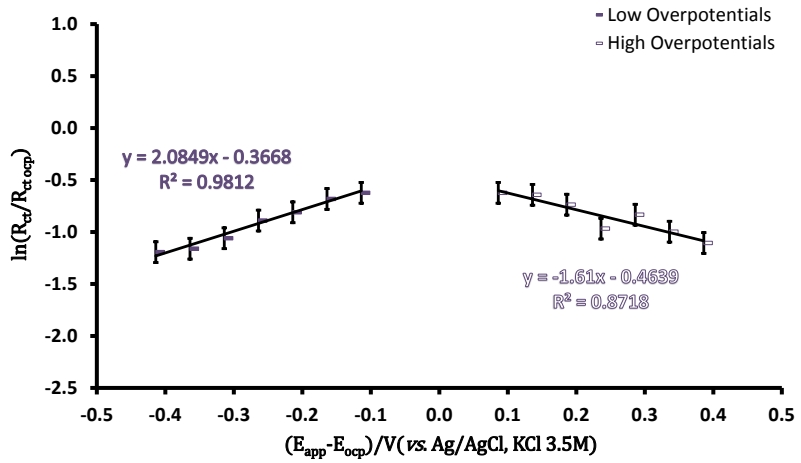

Figure 4.18 – Variation of the charge transfer resistance of the DPPTE SAM at different applied overpotentials. The solid marker is for negative overpotentials and the empty marker is for positive overpotentials. DPPTE SAM presents a growth factor of 2.1 V^{-1} and a decay factor of 1.6 V^{-1}, according to equation 4.16.

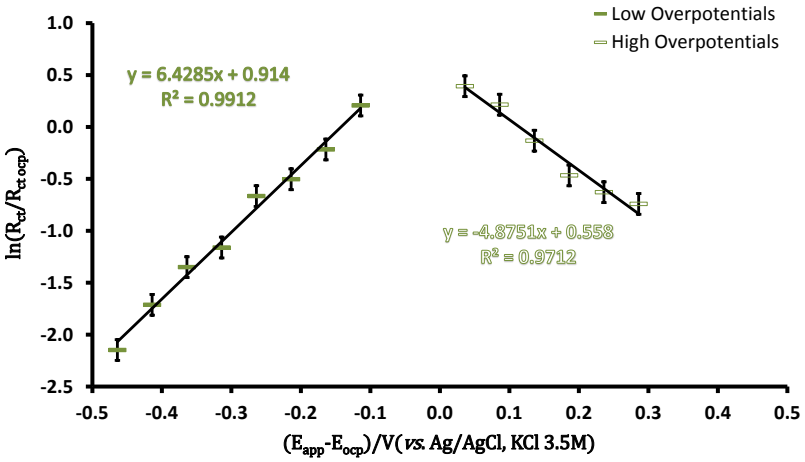

Figure 4.19 – Variation of the charge transfer resistance of the DPPTE+EggPC SAM at different applied overpotentials. The solid marker is for negative overpotentials and the empty marker is for positive overpotentials. DPPTE+EggPC SAM presents a growth factor of 6.4 V^{-1} and a decay factor of 4.9 V^{-1}, according to equation 4.16.

The relationship between the electron transfer rate and potential is usually described by the Butler – Volmer equation:

$$I_{(t)} = nFA\left[k_a^0 c_{R,(0,t)} \exp\left(\alpha n f \eta_{(t)}\right) - k_c^0 c_{O,(0,t)} \exp\left(-(1-\alpha) n f \eta_{(t)}\right)\right] \qquad 4.17$$

where $f = \frac{F}{RT}$, α is the charge transfer coefficient, A the geometrical area of the electrode, η is the overpotential and the other parameters have the same meaning has before.[59–61]

When there are no mass transfer effects, at large overpotentials, the Butler – Volmer equation takes the form

$$I = I_0 \exp(\alpha f \eta) \qquad 4.18$$

According to the Marcus theory of density of states model (DOS), in presence of double layer effects, α is dependent on η.[61,62] Equation 4.18, at a large overpotential and for small changes in overpotential, can lead to

$$R_{ct} = R_{ct\,ocp} \frac{\exp(\alpha n f \eta)}{\alpha} \qquad 4.19$$

or

$$\ln\left(\frac{R_{ct}}{R_{ct\,ocp}}\right) = \alpha n f \eta - \ln\alpha \qquad 4.20$$

Comparing equations 4.16 and 4.20, one arrives to the conclusion that

$$-\gamma = \alpha n f \qquad 4.21$$

The values of α at negative overpotentials for the different SAMs can be obtained from plots of $\ln\left(\frac{R_{ct}}{R_{ct\,ocp}}\right)$ *vs.* η, figures 4.17 to 4.19, and are shown in table 4.3. Differentiation of equation 4.17 with respect to potential, for a steady value of potential, one obtains equation 4.22. Knowing α for each negative overpotential is possible to determine k_{app}^0 for each negative overpotential (table 4.3) using equation 4.22.[60]

$$R_{ct}^{-1} = n^2 FfA \left[\overbrace{\alpha\, k^0_{app(a)}\, c_{R,(0)}\, \exp(\alpha n \eta f)}^{negative\ overpotentials} + \underbrace{(1-\alpha)\, k^0_{app(c)}\, c_{O,(0)}\, \exp((1-\alpha) n \eta f)}_{positive\ overpotentials} \right] \qquad 4.22$$

Table 4.3 – α and k^0_{app} for the different SAMs formed, at negative overpotentials.

η/V	DDT			DPPTE			DPPTE+EggPC		
	$\ln(R_{ct}/R_{ct\,ocp})$	α	k^0_{app}/(cm s^{-1})	$\ln(R_{ct}/R_{ct\,ocp})$	α	k^0_{app}/(cm s^{-1})	$\ln(R_{ct}/R_{ct\,ocp})$	α	k^0_{app}/(cm s^{-1})
-0.464	-3.66×10^{-1}	0.131	3.68×10^{-4}	-1.16	0.162	2.02×10^{-3}	-2.14	0.203	7.59×10^{-3}
-0.414	-3.40×10^{-1}	0.140	3.03×10^{-4}	-6.25×10^{-1}	0.153	7.82×10^{-4}	-1.71	0.202	3.23×10^{-3}
-0.364	-2.24×10^{-1}	0.148	2.16×10^{-4}	5.92×10^{-1}	0.166	6.22×10^{-4}	-1.34	0.204	1.53×10^{-3}
-0.314	-9.88×10^{-2}	0.157	1.50×10^{-4}	-4.91×10^{-1}	0.178	4.40×10^{-4}	-1.15	0.216	9.33×10^{-4}
-0.264	1.04×10^{-1}	0.163	9.21×10^{-5}	-3.21×10^{-1}	0.190	2.76×10^{-4}	-6.59×10^{-1}	0.212	3.61×10^{-4}
-0.214	3.15×10^{-1}	0.171	5.50×10^{-5}	-2.42×10^{-1}	0.212	1.89×10^{-4}	-4.97×10^{-1}	0.231	2.18×10^{-4}
-0.164	3.60×10^{-1}	0.196	3.84×10^{-5}	-1.13×10^{-1}	0.238	1.15×10^{-4}	-2.11×10^{-1}	0.248	1.08×10^{-4}
-0.114	1.47×10^{-1}	0.263	3.26×10^{-5}	-5.44×10^{-2}	0.288	7.03×10^{-5}	2.13×10^{-1}	0.255	4.33×10^{-5}
-0.064	-6.61×10^{-2}	0.394	2.23×10^{-5}	-3.56×10^{-2}	0.388	3.73×10^{-5}	3.72×10^{-1}	0.312	2.11×10^{-5}
-0.014	-1.17×10^{-1}	0.744	6.90×10^{-6}	-2.32×10^{-6}	0.696	1.13×10^{-5}	4.23×10^{-1}	0.497	7.51×10^{-6}

The values of α decrease with increasing overpotentials, in agreement with the Marcus DOS model. At the less negative overpotential (-0.014 V), the value for k^0_{app} for the three SAMs approach the values obtained using equation 4.15 (Table 4.1).[61]

4.3. Conclusion

Combined cyclic voltammetry and EIS studies were used for the evaluation of theoretical and experimental electron transfer rate constants of SAMs of a thiolipid and a mixture of the thiolipid with a phosphocholine lipid. Θ_a *vs.* d_a plots give an indication of the defects in the monolayers. The high deviations from the theoretical values observed in the case of the HPT SAM show the presence of pinholes and indicate the existance of mixed electron

transfer through tunneling and pinhole defects. The diferences between the theoretical and experimental values are much smaller in the case of the DDT, DPPTE and DPPTE+EggPC SAMs indicating that electron transfer occurs, probably, through tunneling. At negative overpotentials, the electron transfer kinetics could be probed using EIS, showing the potential dependency according to Marcus DOS theory.

Although both DPPTE and DPPTE+EggPC SAMs were of good quality, the later seems to be even better, so this is the monolayer that will be used to produce tethered bilayer lipid membranes.

References

(1) Franklin, B.; Brownrigg, W.; Farish, M. *Phil. Trans.* **1774**, *64*, 445 –460.
(2) Subramanian, S.; Sampath, S. *J. Ind. Inst. Science* **2009**, *89*, 1–7.
(3) Morgan, R. J. Pouring Oil on the Water http://www.robertjmorgan.com/journal/blog/archives/1621 (accessed Oct 7, 2011).
(4) Rayleigh, Lord *Philos. Mag.* **1899**, *48*, 321–337.
(5) Pockels, A. *Nature* **1891**, *43*, 437–439.
(6) *Nobel Lectures, Chemistry 1922 -1941*; Elsevier Publishing Company: Amsterdam, 1966.
(7) Bigelow, W. C.; Pickett, D. L.; Zisman, W. A. *J. Coll. Sci.* **1946**, *1*, 513–538.
(8) Nuzzo, R. G.; Allara, D. L. *J. Am. Chem. Soc.* **1983**, *105*, 4481–4483.
(9) Swalen, J. D.; Allara, D. L.; Andrade, J. D.; Chandross, E. A.; Garoff, S.; Israelachvili, J.; McCarthy, T. J.; Murray, R.; Pease, R. F.; et al. *Langmuir* **1987**, *3*, 932–950.
(10) Dubois, L. H.; Nuzzo, R. G. *Annu. Rev. Phys. Chem.* **1992**, *43*, 437–463.
(11) Love, J. C.; Estroff, L. A.; Kriebel, J. K.; Nuzzo, R. G.; Whitesides, G. M. *Chem. Rev.* **2005**, *105*, 1103–1170.
(12) Vericat, C.; Vela, M. E.; Benitez, G.; Carro, P.; Salvarezza, R. C. *Chem. Soc. Rev.* **2010**, *39*, 1805–1834.
(13) Ulman, A. *Chem. Rev.* **1996**, *96*, 1533–1554.
(14) Vallejo, A. E.; Gervasi, C. A. *Bioelectrochemistry* **2002**, *57*, 1–7.
(15) Ulman, A.; Eilers, J. E.; Tillman, N. *Langmuir* **1989**, *5*, 1147–1152.
(16) Strong, L.; Whitesides, G. M. *Langmuir* **1988**, *4*, 546–558.
(17) Bucher, J.-P.; Santesson, L.; Kern, K. *Langmuir* **1994**, *10*, 979–983.
(18) Chidsey, C. E. D.; Liu, G.-Y.; Rowntree, P.; Scoles, G. *J. Chem. Phys.* **1989**, *91*, 4421–4423.
(19) Alves, C. A.; Smith, E. L.; Porter, M. D. *J. Am. Chem. Soc.* **1992**, *114*, 1222–1227.
(20) Finklea, H. O.; Avery, S.; Lynch, M.; Furtsch, T. *Langmuir* **1987**, *3*, 409–413.
(21) Bain, C. D.; Troughton, E. B.; Tao, Y. T.; Evall, J.; Whitesides, G. M.; Nuzzo, R. G. *J. Am. Chem. Soc.* **1989**, *111*, 321–335.
(22) Shen, H.; Mark, J. E.; Seliskar, C. J.; Mark Jr., H. B.; Heineman, W. R. *J. Solid State Electrochem.* **1997**, *1*, 148–154.
(23) Yang, M.; Zhang, Z. *Electrochim. Acta* **2004**, *49*, 5089–5095.
(24) Schreiber, F. *Prog.Surf. Sci.* **2000**, *65*, 151–257.
(25) Peterlinz, K. A.; Georgiadis, R. *Langmuir* **1996**, *12*, 4731–4740.
(26) Dannenberger, O.; Wolff, J. J.; Buck, M. *Langmuir* **1998**, *14*, 4679–4682.
(27) Diao, P.; Jiang, D.; Cui, X.; Gu, D.; Tong, R.; Zhong, B. *Bioelectrochem. Bioenerg.* **1999**, *48*, 469–475.
(28) Lin, X.; Gong, J. *Anal. Chim. Acta* **2004**, *507*, 255–261.
(29) Porter, M. D.; Bright, T. B.; Allara, D. L.; Chidsey, C. E. D. *J. Am. Chem. Soc.* **1987**, *109*, 3559–3568.
(30) Finklea, H. O.; Snider, D. A.; Fedyk, J.; Sabatani, E.; Gafni, Y.; Rubinstein, I. *Langmuir* **1993**, *9*, 3660–3667.
(31) Sabatani, E.; Rubinstein, I.; Maoz, R.; Sagiv, J. *J. Electroanal. Chem. Interfacial Electrochem.* **1987**, *219*, 365–371.
(32) Xing, Y. F.; Li, S. F. Y.; Lau, A. K. H.; O'Shea, S. J. *J. Electroanal. Chem.* **2005**, *583*, 124–132.
(33) Mandler, D.; Turyan, I. *Electroanal.* **1996**, *8*, 207–213.
(34) Chidsey, C. E. D.; Bertozzi, C. R.; Putvinski, T. M.; Mujsce, A. M. *J. Am. Chem. Soc.* **1990**, *112*, 4301–4306.

(35) Smalley, J. F.; Feldberg, S. W.; Chidsey, C. E. D.; Linford, M. R.; Newton, M. D.; Liu, Y.-P. *J. Phys. Chem.* **1995**, *99*, 13141–13149.
(36) Hong, H.-G.; Park, W. *Bull. Korean Chem. Soc.* **2005**, *583*, 1885 – 1888.
(37) Arikuma, Y.; Nakayama, H.; Morita, T.; Kimura, S. *Langmuir* **2010**, *27*, 1530–1535.
(38) Plant, A. L.; Gueguetchkeri, M.; Yap, W. *Biophys. J.* **1994**, *67*, 1126–1133.
(39) Jenkins, A. T. A.; Boden, N.; Bushby, R. J.; Evans, S. D.; Knowles, P. F.; Miles, R. E.; Ogier, S. D.; Schönherr, H.; Vancso, G. J. *J. Am. Chem. Soc.* **1999**, *121*, 5274–5280.
(40) Jadhav, S. R.; Sui, D.; Garavito, R. M.; Worden, R. M. *J. Colloid Interface Sci.* **2008**, *322*, 465–472.
(41) Davies, T. J.; Ward-Jones, S.; Banks, C. E.; del Campo, J.; Mas, R.; Muñoz, F. X.; Compton, R. G. *J Electroanal Chem* **2005**, *585*, 51–62.
(42) Davies, T. J.; Compton, R. G. *J Electroanal Chem* **2005**, *585*, 63–82.
(43) Amatore, C.; Savéant, J. M.; Tessier, D. *J. Electroanal. Chem.* **1983**, *147*, 39–51.
(44) Evans, S. D.; Freeman, T. L.; Flynn, T. M.; Batchelder, D. N.; Ulman, A. *Thin Solid Films* **1994**, *244*, 778–783.
(45) Diao, P.; Guo, M.; Jiang, D.; Jia, Z.; Cui, X.; Gu, D.; Tong, R.; Zhong, B. *J. Electroanal. Chem.* **2000**, *480*, 59–63.
(46) Protsailo, L. V.; Fawcett, W. R. *Electrochim. Acta* **2000**, *45*, 3497–3505.
(47) Marcus, R. A.; Sutin, N. *Biochim. Biophys. Acta, Rev. Bioenerg.* **1985**, *811*, 265–322.
(48) Edwards, P. P.; Gray, H. B.; Lodge, M. T. J.; Williams, R. J. P. *Angew. Chem. Int. Ed.* **2008**, *47*, 6758–6765.
(49) James, D. K.; Tour, J. M. *Chem. Mater.* **2004**, *16*, 4423–4435.
(50) Rampi, M. A.; Whitesides, G. M. *Chem. Phys.* **2002**, *281*, 373–391.
(51) Diao, P.; Jiang, D.; Cui, X.; Gu, D.; Tong, R.; Zhong, B. *Bioelectrochem. Bioenerg.* **1998**, *45*, 173–179.
(52) Diao, P.; Jiang, D.; Cui, X.; Gu, D.; Tong, R.; Zhong, B. *J. Electroanal. Chem.* **1999**, *464*, 61–67.
(53) Closs, G. L.; Miller, J. R. *Science* **1988**, *240*, 440–447.
(54) Fettiplace, R.; Andrews, D. M.; Haydon, D. A. *J. Membr. Biol.* **1971**, *5*, 277–296.
(55) Becka, A. M.; Miller, C. J. *J. Phys. Chem.* **1992**, *96*, 2657–2668.
(56) Sabatani, E.; Rubinstein, I. *J. Phys. Chem.* **1987**, *91*, 6663–6669.
(57) Sahalov, H.; O'Brien, B.; Stebe, K. J.; Hristova, K.; Searson, P. C. *Langmuir* **2007**, *23*, 9681–9685.
(58) Sachs, S. B.; Dudek, S. P.; Hsung, R. P.; Sita, L. R.; Smalley, J. F.; Newton, M. D.; Feldberg, S. W.; Chidsey, C. E. D. *J. Am. Chem. Soc.* **1997**, *119*, 10563–10564.
(59) Bard, A. J.; Faulkner, L. R. *Electrochemical methods: fundamentals and applications*; 2nd ed.; John Wiley & Sons: New York, 2001.
(60) Girault, H. H. *Analytical and Physical Electrochemistry*; 1st ed.; EFPL Press, 2004.
(61) Xing, Y. F.; O'Shea, S. J.; Li, S. F. Y. *J. Electroanal. Chem.* **2003**, *542*, 7–11.
(62) Finklea, H. O. *J. Electroanal. Chem.* **2001**, *495*, 79–86.

5. Bilayer Lipid Membranes Modified with Bio – Electroactive Molecules

Tethered bilayers lipid membranes (tBLMs) are commonly used as model membranes. However in biophysical studies free-standing membranes or 'black' lipid membranes are more realistic models of cellular processes. In this chapter is discussed the rates of electron transfer in both types of bilayer lipid membranes. These BLMs were then modified using two very important mitochondrial membrane associated molecules – ubiquinone-10 (UQ_{10}) and α-tocopherol (VitE). The electron transfer rates in the unmodified films were studied with three redox couples, $Fe(CN)_6^{3-/4-}$, $Ru(NH_3)_6^{3+/2+}$ and NAD^+/NADH, using electrochemical impedance spectroscopy (EIS) and cyclic voltammetry (CV). The rate of electron transfer in the modified films was studied using the biologically relevant NAD^+/NADH electroactive couple, using the same methods.

It is shown that when the BLMs are modified with only UQ_{10} it is possible to observe electron transfer. However, when the antioxidant VitE is added to the modification the

electron transfer provided by UQ_{10} is inhibited. Following initial studies using CV, a comparison of electron transfer theory and data was used to investigate this phenomenon in more detail, using EIS data. The standard rate constant caused by electron tunnelling across the film, k_{th}^0, depends on the value of β used. Two different values of the potential independent electron tunnelling coefficient, β, were fitted and it is shown that a β value half of those usually reported in literature gives better agreement between the theory and the experimental results. The unmodified films present k_{th}^0 values in the order of 10^{-15} cm s^{-1} when β=0.72$Å^{-1}$ and k_{th}^0 values in the order of 10^{-9} cm s^{-1} when β=0.38$Å^{-1}$, for the modified films the values of k_{th}^0 are in the order of 10^{-15} cm s^{-1} when β=0.72$Å^{-1}$ and 10^{-9} cm s^{-1} for β=0.38$Å^{-1}$. The experimental electron transfer rate constant, k_{app}^0, is in the order of 10^{-8} cm s^{-1} for unmodified and modified (with (i)UQ_{10}, (ii)VitE and (iii)UQ_{10}+VitE) films.

5.1. Introduction

Bilayer lipid membranes (BLMs) are widely used to mimic the cell membrane[1–5] and are used to study transport phenomena and other forms of cell signal transduction.[6–8] There are many ways of preparing BLMs each one with its advantages and disadvantages; whilst tethered BLMs (tBLMs, figure 1a)) are very robust and stable[2–4,6,9], the main advantage of black lipid membranes (also known as free standing BLMs between two aqueous solutions) is that the membrane is formed between two aqueous solutions which makes it a better mimic of the cell membrane.[1,4] In black lipid membranes electrodes are inserted in two aqueous phases separated by the BLM, which allows the measurement of the membrane potential and the rate of electron transport, figure 1b).[10–12]

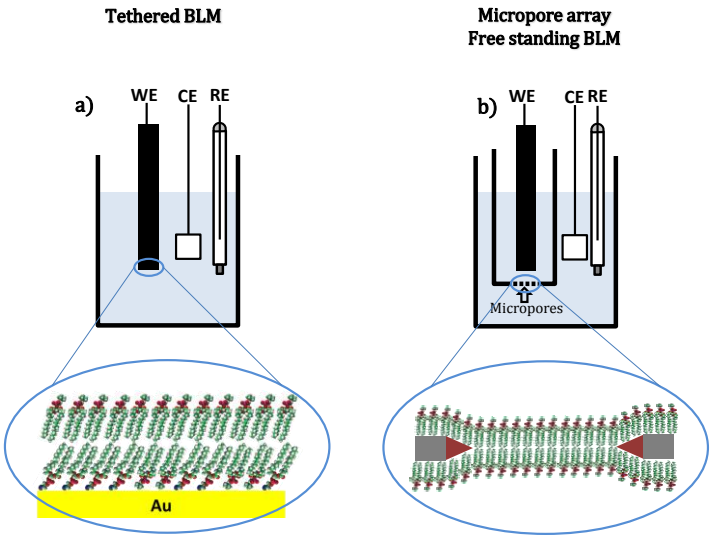

Figure 5.1 – Schematic representation of a) tethered BLM and b) free standing BLM.

In the tBLMs the lower leaflet (self-assembled monolayer) is formed by chemisorption of the thiolipid or alkanethiol on a gold surface.[13–15] These chemisorbed structures provide considerable interest in electrochemistry because of their potential for testing the Marcus model of electron transfer[16,17]; and for the study of electron transfer in BLMs.[16,18] In order to understand the various electron transport mechanisms, the self-assembled monolayers (SAMs) need to be sufficiently compact so that electrochemical processes occurring directly at the gold-solution interface are suppressed.[17,19] In addition, the quality of the BLM is dependent on the quality of the SAM.[17,20]

In previous reports, black lipid membranes have been used to study electron transport[10,21], ion transport[11,12,22] and have been incorporated in microfluidic devices.[23,24] In electron transport studies, Shiba et al[10] modified psBLMs with 7,7,8,8 – tetracyanoquinodimethane and decamethyl ferrocene, and studied the electron transfer between $[Fe(CN)_6]^{4-}$ in one phase and $[Fe(CN)_6]^{3-}$ in the other. They concluded that the electron transport can occur by two distinct mechanisms, either by an electron hopping mechanism where electron transport is facilitated by the redox species in the BLM or it is controlled by mass transfer of the redox species. Cliffel and co-workers[21] used SECM to

measure mass transport of $Ru(NH_3)_6Cl_3$ in phosphatidylcholine bilayer lipid membranes modified with alamethicin pores. In relevant ion transport studies, Ozaki and co-workers demonstrated that an uncoupler, carbonylcyanide p-trifluoromethoxyphenylhydrazone, inserted in a black lipid membrane can induce pH dependent transport of H^+ and Na^+ in the absence of ion channels or ion carriers.[12] The transport of Li^+, Na^+, K^+ and NH_4^+ has been studied using different ion channels and ion carriers, where is shown a dependence of ion transport with the amount of ion channel/ion carrier.[11]

Proof of principle for the formation of black lipid membranes suitable for incorporation in microfluidic devices has reported by several groups. However, these publications do not report any mechanistic studies.

This chapter focuses on the study the effects on electron transport rates of two very important mitochondrial membrane associated molecules, Ubiquinone-10 (UQ_{10}) and α-tocopherol (VitE), using both tBLMS and black lipid membranes (in our case the membrane support is a micropore array, and therefore termed pore suspended BLMs - psBLMs) using three redox couples, $Fe(CN)_6^{3-/4-}$, $Ru(NH_3)_6^{3+/2+}$ and NAD^+/NADH. The most important role of mitochondria is to produce adenosine triphosphate (ATP) through respiration and to regulate cellular metabolism in the Kreb's cycle.[25] Within the mitochondria UQ_{10} is particularly interesting due to its central role in the electron transfer chain.[26–28] UQ_{10} has a 10 unit isoprenoid (5 nm) semi-rigid chain and because of this its most likely position within the lipid bilayer is in the membrane midplane, figure 5.2.[26,29,30]

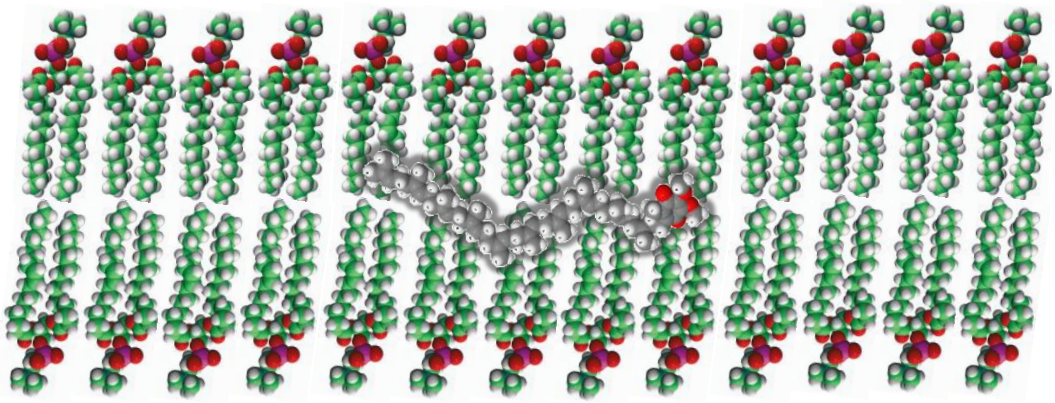

Figure 5.2 – Schematic representation of the position of UQ_{10} within the lipid bilayer. Due to its 10 unit isoprenoid semi-rigid chain, UQ_{10} most likely position within the lipid bilayer is in the membrane midplane.

α-tocopherol (VitE) is the most likely vitamin to react with UQ_{10} because they both are redox active, lipophilic compounds present in the membrane and both have antioxidant properties.[31] VitE consists of a chroman head and a phytyl tail[32], its positions in the bilayer is not completely clear and three positions have been suggested, i) the tail is well within the hydrophobic domain of the bilayer but the chroman head is placed near the water-lipid interface, ii) the chroman head is around 1nm away from the interface, and iii) the molecule is well within the hydrophobic region of the membrane bilayer, figure 5.3.[30]

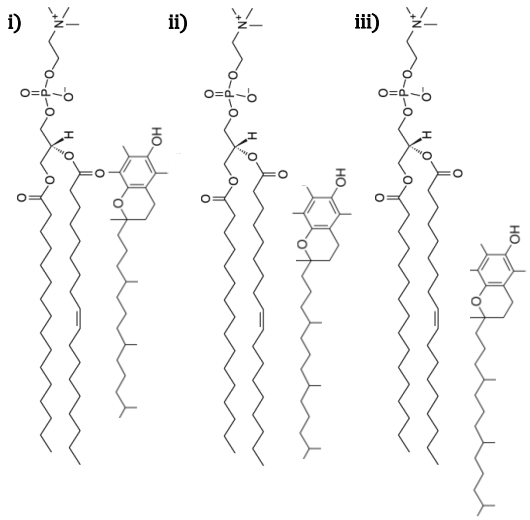

Figure 5.3 – Schematic representation of the location of VitE within the BLMs. See text for more detail.

UQ_{10} protects cell membranes from oxidation by reacting with lipid radicals produced in the lipid peroxidation chain reaction. The reduced form of UQ_{10} can react with the oxidized VitE reactivating its redox active capabilities.[28,33,34] VitE scavenges peroxide free radicals and converts them to less toxic lipid hydroperoxides. The phenoxyl radical of VitE reacts with ubiquinol to reactivate its antioxidant properties (Figure 5.4).[35–40]

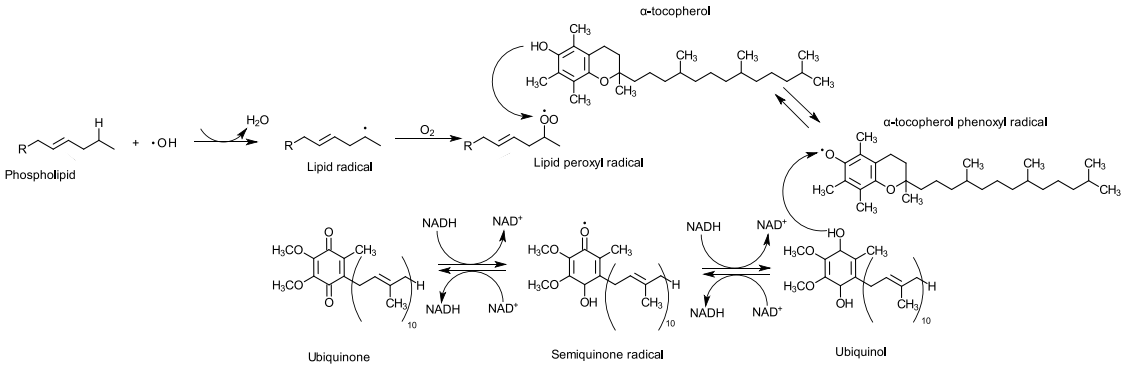

Figure 5.4 – Interaction between the lipids, VitE and UQ_{10}.[35–40]

In previous work Schiffrin and co-workers studied self-assembled monolayers on mercury electrodes[26], confirming that the phospholipid monolayer modified with UQ_{10} showed redox chemistry. The redox process was shown to be dependent on the position of the quinone headgroup; and for pH > 7 the incorporation of UQ_{10} in the monolayer made its reduction very irreversible. At pH < 7 the reaction followed a disproportionation route involving the ubiquinone radical. Contradictory to this report, Marchal and co-workers[41] studied laterally supported dimyristoyl phosphatidylcholine BLMs inserted with UQ_{10} on a microporous electrode and found that below pH 12, the two electrons-two protons electrochemical process at the gold electrode appeared under kinetic control and they based all their thermodynamic deductions in the observed reversibility of the quinone/hydroquinol anion transformation at pH > 13. Schiffrin et al[27] also studied transmembrane electron transfer across phospholipid bilayer membranes (BLMs) mediated by ubiquinone, using patch clamp micropipettes. They used Fe(II)/Fe(III)

citrate solutions to control redox potentials and reported a transfer coefficient of 0.5. They concluded that the rate-determining step is the transfer of the semiubiquinone radical anion, instead of charge transfer reactions at the membrane/electrolyte solution boundaries.

The stepwise electron and proton transfer was questioned by Haddox and Finklea[42] when studying proton coupled electron transfer of galvinol (molecule that can be seen as a model for the study of phenol-like redox centres – hydroquinones and catechols) in SAMs. Both the thermodynamic and the kinetic behaviour of the galvinol system were studied in a wide range of pHs (from 2 to 14); while thermodynamically the system behaves accordingly to the model, kinetically the system only follows the model at pH>7. At low pHs the system shows values of $\log k_{app}$ higher than those predicted theoretically, based on that observation the authors suggested that the assumption of the stepwise proton/electron transfer was invalid even when the rate of electron transfer is much slower than the predicted rate of proton transfer.

Transmembrane electron transfer reactions have been studied by Hurst et al.[43,44] and by Hammarström et al.[45,46] Hurst's group studied the electron transfer across bilayer membranes of dihexadecyl phosphate (DHP) in small unilamellar vesicles containing viologen (N,N'-dialkyl-4,4'-bipyridinium). They observed that violgen radicals inserted in the membrane phase could mediate electron transfer. They concluded that short chain (<12 C units) viologens act as mobile relays, whereas long chain viologens transfer electrons mainly by electron tunnelling. However, using phosphatidylcholine vesicles with viologen radicals as external electron donor and $Fe(CN)_6^{3-}$ as the internal electron acceptor, Hammarström and co-workers have shown that the transfer through the phospholipid membrane is preceded by disproportionation of the viologen radical to the neutral form, the mechanism for electron transfer is transport and not tunnelling.

In the work presented in this chapter all the measurements were made at pH 7.4 to mimic the physiological conditions. NAD^+/NADH was used as electron mediators for mimicking biological systems. The redox reaction of NAD^+/NADH involves the transfer of two electrons and has been used to study biological phenomena, processes involving chemical transformation and/or energy conversion and enzymatic reactions.[47]

5.2. Discussion

5.2.1. Unmodified films

5.2.1.1. Cyclic Voltammetry

The blocking properties of the modified electrodes were examined using cyclic voltammetry. The measurements were performed in HEPES buffer solutions (pH 7.4)[48] containing one of the following electroactive couples: $Fe(CN)_6^{3-/4-}$, $Ru(NH_3)_6^{3+/2+}$ and NAD^+/NADH. The measurements involving the tBLMs were made in degassed solutions, all the measurements were made at room temperature.

For both types of bilayer and for the three electroactive species under study, the redox reaction is completely inhibited indicating that the film formed is well organized and pinhole free, figures 5.5 to 5.10. Some residual current is observed in the CVs, this may be indicative of electron tunnelling current which allows the kinetics of electron transport. This phenomenon will be studied using EIS.

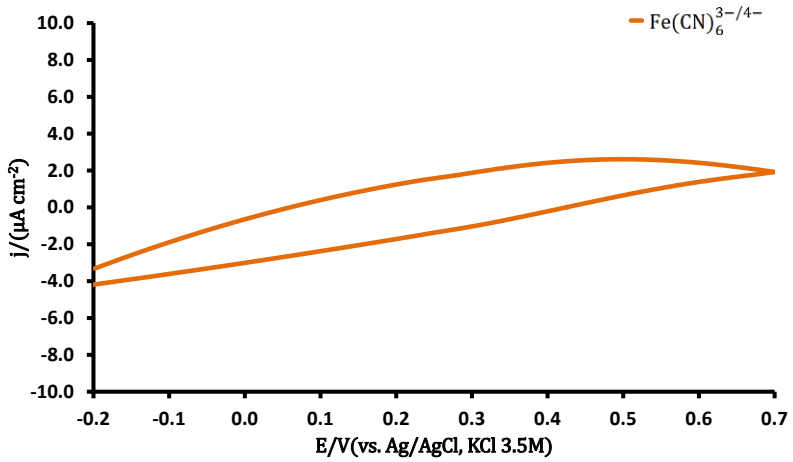

Figure 5.5 – CV of tBLM in 0.5 mM $Fe(CN)_6^{3-}$ + 0.5 mM $Fe(CN)_6^{4-}$, using HEPES buffer (pH 7.4) as background, obtained for scans between -0.2 to +0.7 V (*vs.* Ag/AgCl, KCl 3.5 M) at 50 mV s^{-1}.

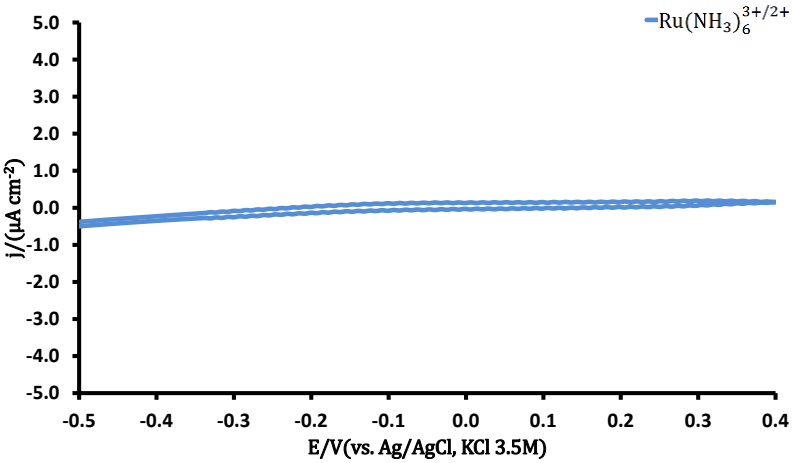

Figure 5.6 – CV of tBLM in 0.5 mM $Ru(NH_3)_6^{3+}$+ 0.5 mM $Ru(NH_3)_6^{2+}$, using HEPES buffer (pH 7.4) as background, obtained for scans between -0.5 to +0.4 V (*vs.* Ag/AgCl, KCl 3.5 M) at 50 mV s^{-1}.

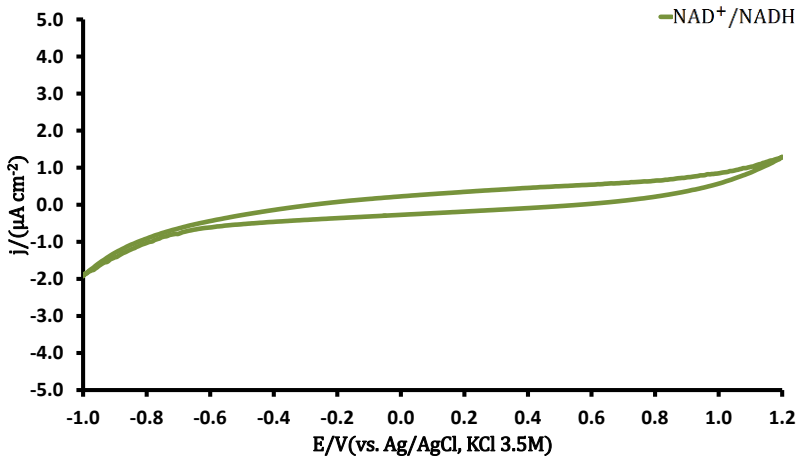

Figure 5.7 – CV of tBLM in 0.25 mM NAD^+ + 0.25 mM NADH, using HEPES buffer (pH 7.4) as background, obtained for scans between -1.0 to +1.2 V (*vs.* Ag/AgCl, KCl 3.5M) at 50 mV s^{-1}.

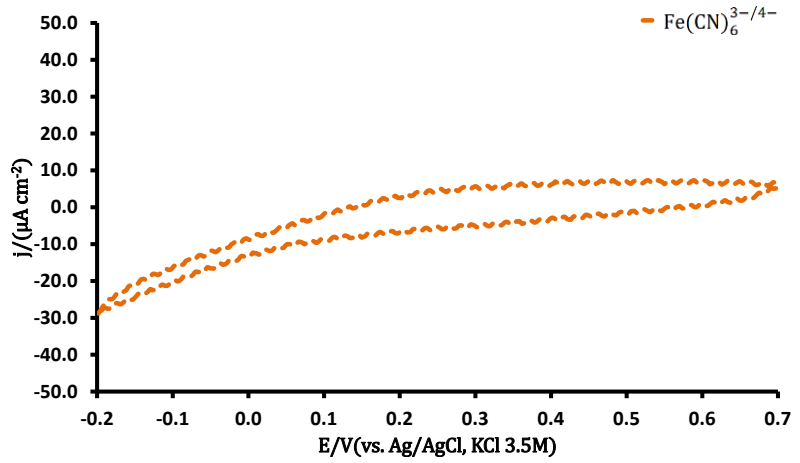

Figure 5.8 – CV of psBLM in 0.5 mM $Fe(CN)_6^{3-}$ + 0.5 mM $Fe(CN)_6^{4-}$, using HEPES buffer (pH 7.4) as background, obtained for scans between -0.2 to +0.7 V (*vs.* Ag/AgCl, KCl 3.5 M) at 50 mV s^{-1}.

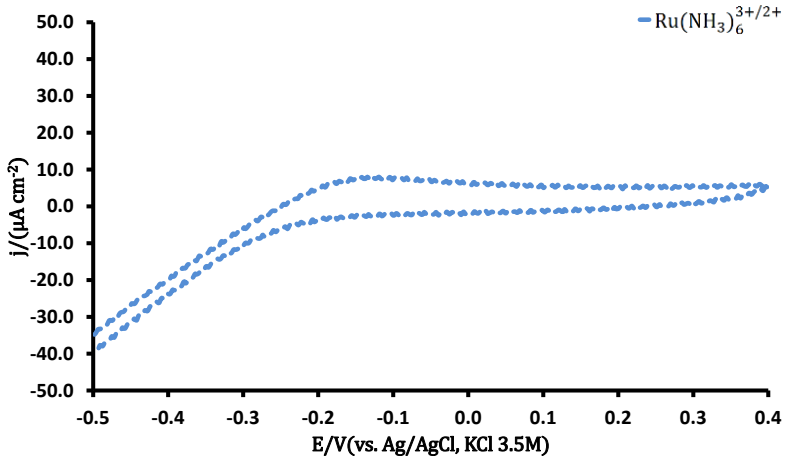

Figure 5.9 – CV of psBLM in 0.5 mM $Ru(NH_3)_6^{3+}$ + 0.5 mM $Ru(NH_3)_6^{2+}$, using HEPES buffer (pH 7.4) as background, obtained for scans between -0.5 to +0.4 V (*vs.* Ag/AgCl, KCl 3.5 M) at 50 mV s^{-1}.

In figure 5.10 the peaks observed correspond to the adsorption of NAD^+/NADH to the electrode surface[49], this adsorption occurs via both the adenine and pyridine moieties as adsorption sites, it is strong and irreversible.[50–52] Figure 5.11 shows the relationship between the peak current and the scan rate, the linear dependence confirms the adsorption process.

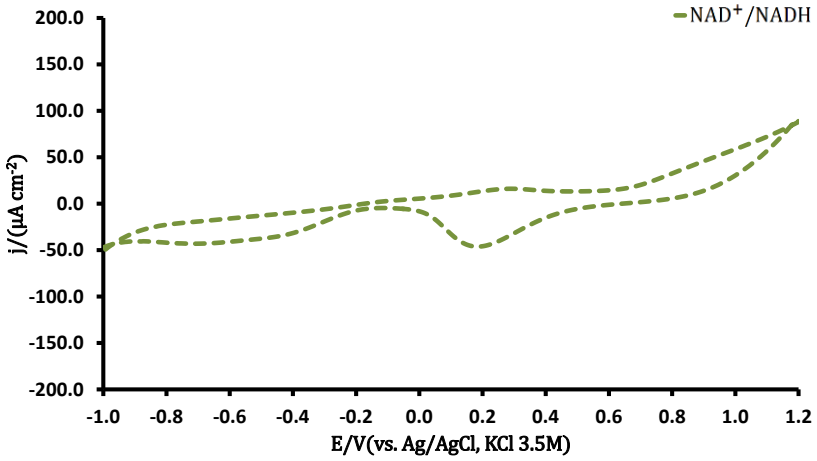

Figure 5.10 – CV of psBLM in 0.25 mM NAD^+ + 0.25 mM NADH, using HEPES buffer (pH 7.4) as background, obtained for scans between -1.0 to +1.2 V (*vs.* Ag/AgCl, KCl 3.5 M) at 50 mV s^{-1}.

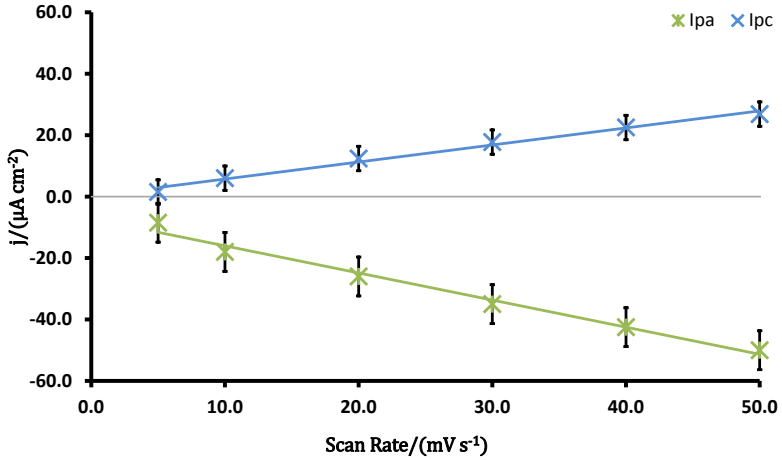

Figure 5.11 – Dependence of the peak current with the scan rate for the psBLM using NAD^+/NADH as electroactive couple. Error bars represent the standard deviation of three measurements.

5.2.1.2. Electrochemical Impedance Spectroscopy

Impedance measurements were made at the equilibrium potential of the redox couples, $Fe(CN)_6^{3-/4-}$ ($E^{0'}$=+0.225 V vs. SCE), $Ru(NH_3)_6^{3+/2+}$ ($E^{0'}$=-0.180 V vs. SCE) or NAD^+/NADH ($E^{0'}$=-0.560 V vs. SCE), at a wide range of frequencies from 1.0×10^5 to 0.1 Hz, with a perturbation of 10 mV in the potential. The electrolyte solution contained 0.5 mM $Fe(CN)_6^{3-}$ + 0.5 mM $Fe(CN)_6^{4-}$, 0.5 mM $Ru(NH_3)_6^{3+}$ + 0.5 mM $Ru(NH_3)_6^{2+}$ or 0.25 mM NAD^+ + 0.25 mM NADH and HEPES buffer solution, background.

The formation of the BLMs was determined by its charge transfer resistance and capacitance values. These values were obtained by fitting the Nyquist plots shown in figures 5.12 to 5.17 with a modified Randles circuit, which takes into account a frequency dependent constant phase element (CPE).

Previous reports indicate that a pin-hole free tBLM should present a capacitance in the range 0.4-0.8 μF cm^{-2} [18,27,53–55] and its charge transfer resistance should be in the range 10^5-10^7 Ω cm^2 [9,55–59], a bare gold electrode presents values of capacitance above 100 μF cm^{-2} and a resistance of charge transfer in the range of 1-10 Ω cm^2.[60,61]

In these studies tBLMs showed a normalized capacitance of 0.41-0.44±0.03 μF cm^{-2} and the charge transfer resistance values are in the MΩ cm^2 region (Table 5.1).

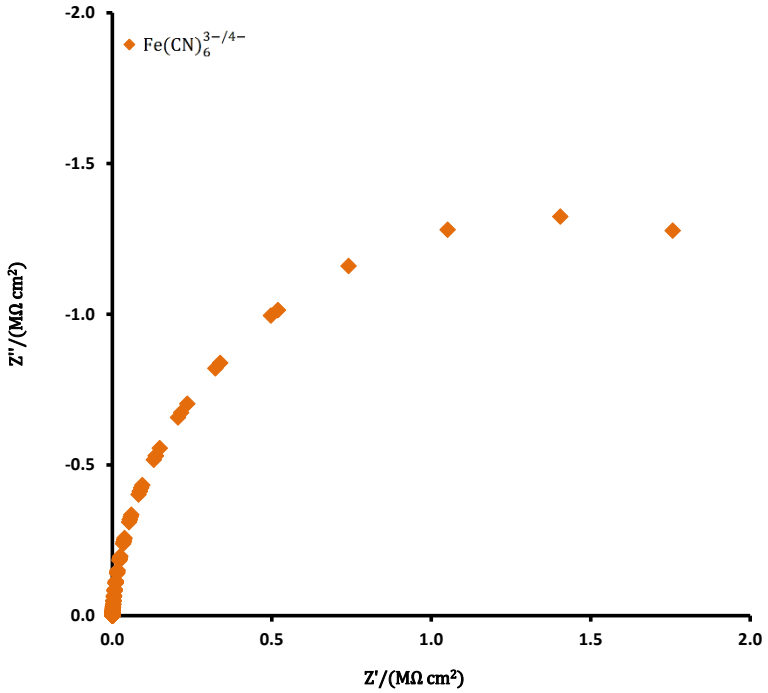

Figure 5.12 – Nyquist plots for the tBLM in 0.5 mM $Fe(CN)_6^{3-}$ + 0.5 mM $Fe(CN)_6^{4-}$, using HEPES buffer (pH 7.4) as background. The semi-ellipse in the entire frequency range indicates that the electron transfer reaction is completely inhibited.

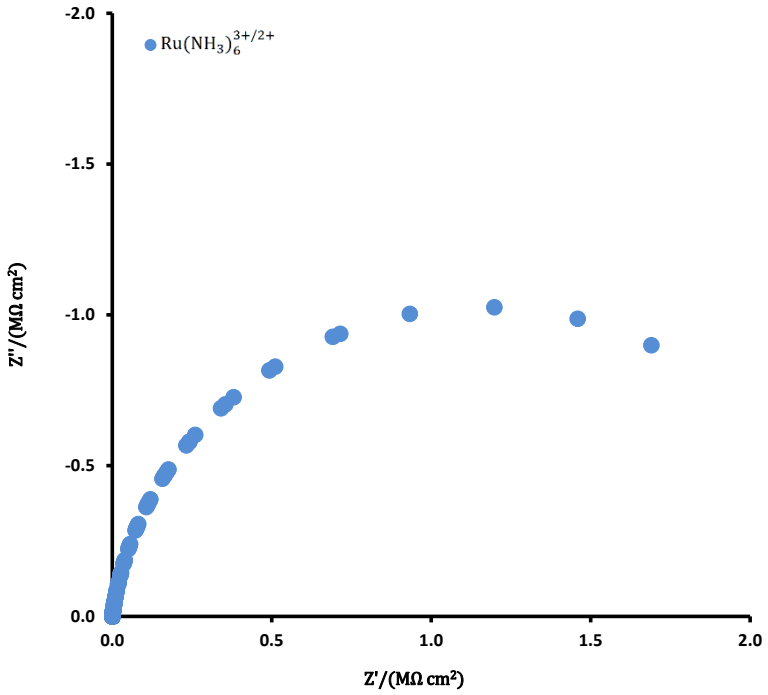

Figure 5.13 – Nyquist plots for the tBLM in 0.5 mM $Ru(NH_3)_6^{3+}$ + 0.5 mM $Ru(NH_3)_6^{2+}$, using HEPES buffer (pH 7.4) as background. The semi-ellipse in the entire frequency range indicates that the electron transfer reaction is completely inhibited.

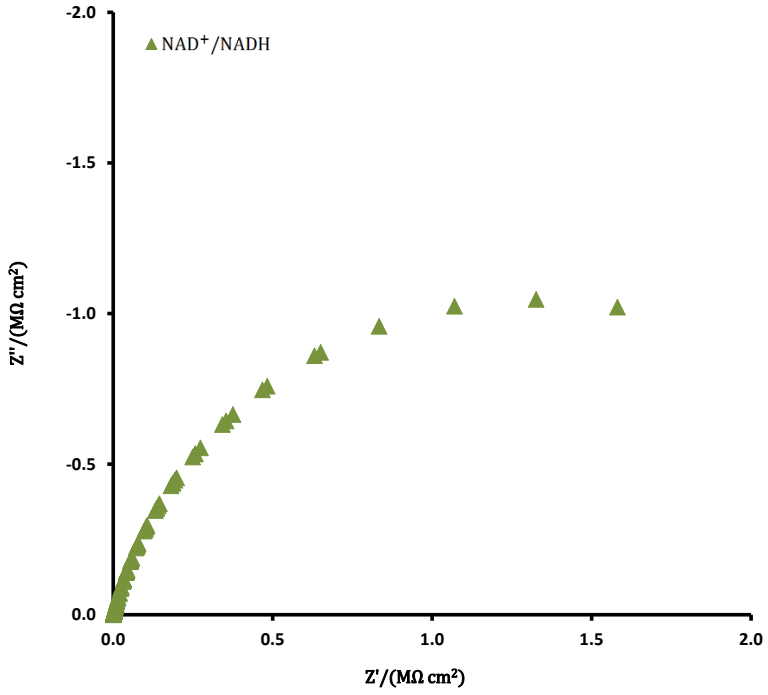

Figure 5.14 – Nyquist plots for the tBLM in 0.25 mM NAD^+ + 0.25 mM NADH, using HEPES buffer (pH 7.4) as background. The semi-ellipse in the entire frequency range indicates that the electron transfer reaction is completely inhibited.

In the case of the psBLM the capacitance values were found to be 0.43±0.03 μF cm^{-2} for $Fe(CN)_6^{3-/4-}$, 0.41±0.03μF cm^{-2} for $Ru(NH_3)_6^{3+/2+}$ and 0.47±0.03 μF cm^{-2} for NAD^+/NADH, which is in agreement with previously reported values[58,59], also the resistance values are in good agreement with the values present in the literature[54,55], being in the range 3-9 MΩ cm^2 (Table 5.1).

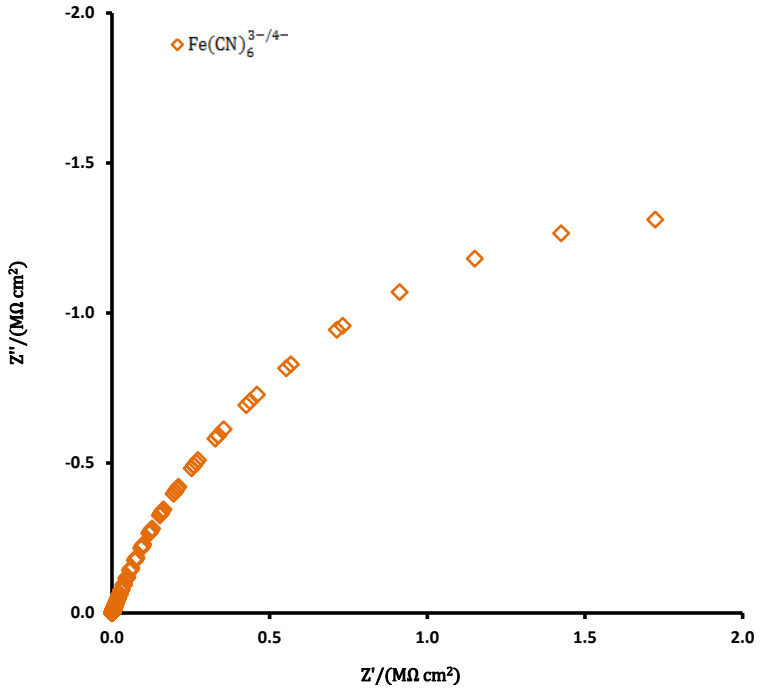

Figure 5.15 – Nyquist plots for the psBLM in 0.5 mM $Fe(CN)_6^{3-}$ + 0.5 mM $Fe(CN)_6^{4-}$, using HEPES buffer (pH 7.4) as background. The semi-ellipse in the entire frequency range indicates that the electron transfer reaction is completely inhibited.

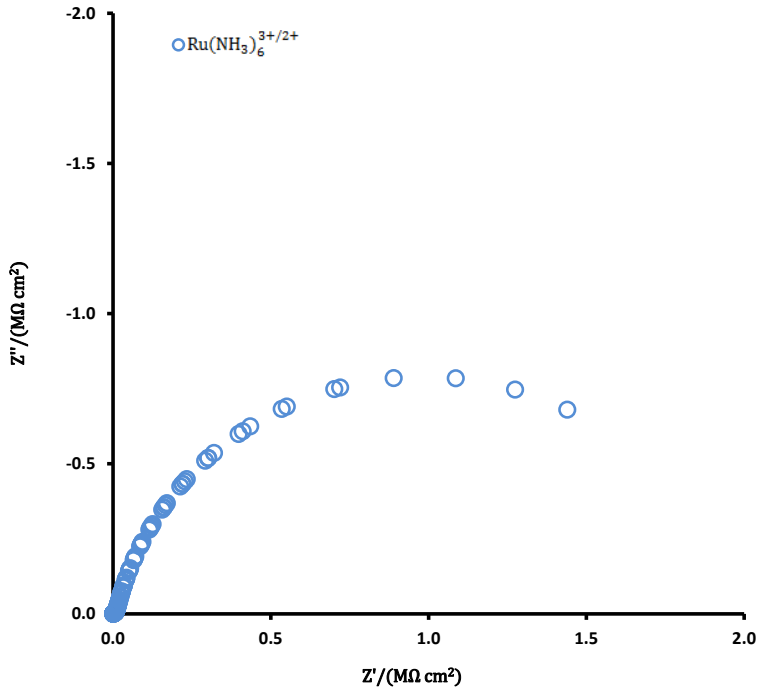

Figure 5.16 – Nyquist plots for the psBLM in 0.5 mM $Ru(NH_3)_6^{3+}$ + 0.5 mM $Ru(NH_3)_6^{2+}$, using HEPES buffer (pH 7.4) as background. The semi-ellipse in the entire frequency range indicates that the electron transfer reaction is completely inhibited.

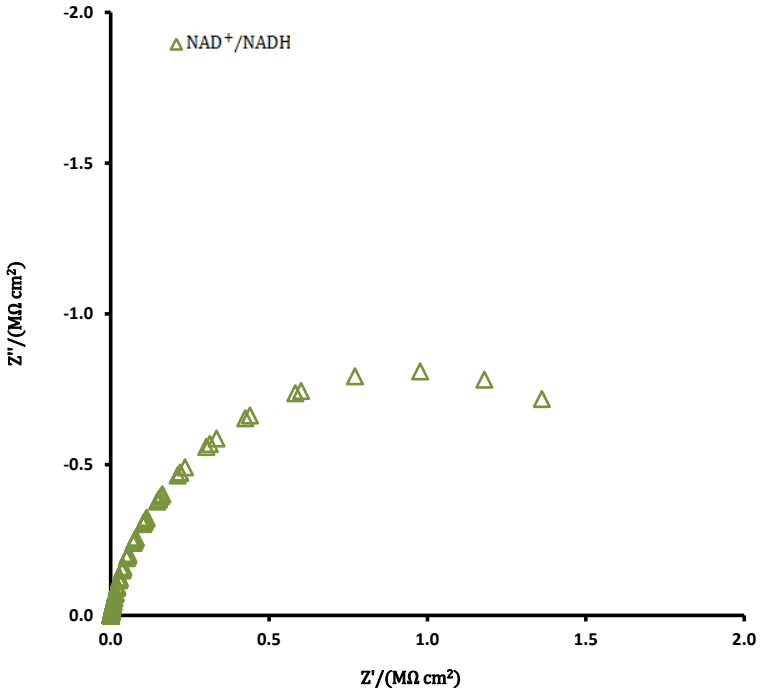

Figure 5.17 – Nyquist plots for the psBLM in 0.25 mM NAD^+ + 0.25 mM NADH, using HEPES buffer (pH 7.4) as background. The semi-ellipse in the entire frequency range indicates that the electron transfer reaction is completely inhibited.

Table 5.1 – Normalized capacitance and charge transfer resistance of the unmodified films formed in this work. The values here presented indicate that the structures formed are bilayers.

		$C_{layer\ ocp}$/(μF cm^{-2})	R_{ct}/(MΩ cm^2)
$Fe(CN)_6^{3-/4-}$	tBLM	0.43±0.03	2.80±0.22
	psBLM	0.43±0.03	3.74±0.32
$Ru(NH_3)_6^{2+/3+}$	tBLM	0.41±0.03	2.32±0.20
	psBLM	0.41±0.03	1.95±0.18
NAD^+/NADH	tBLM	0.44±0.03	2.22±0.17
	psBLM	0.47±0.04	1.90±0.17

5.2.1.3. Rates of Electron Transfer

Electron transfer kinetics was analysed the same way as in chapter 4.

When calculating k_{th}^0 [‡] two different values of β were used. In the first set of calculations a value of β=0.72Å^{-1} was used. This same value was used by Diao and co-workers for probing electron transfer on Pt-BLMs[18] using $K_3Fe(CN)_6$ as probe molecule, although the value is never explicitly shown or mentioned. When using this value of β it yields values of k_{th}^0 in the order of 10^{-15} cm s^{-1} for the bilayers which, when compared to k_{app}^0 [§], gives differences of over six orders of magnitude (Table 5.2), which are clearly incorrect.

Using a different approach, the value of β used is based on the conclusions that Mirkin and co-workers reached when studying electron transfer through lipid monolayers at a liquid/liquid interface.[62] They have shown that, due to penetration of $ZnPor^+$ into the lipid monolayer, β is about one-half of that usually reported. Assuming that in the work here presented there is also penetration of the redox couple into the lipid bilayer, the value of β

[‡] $k_{th}^0 = k_b^0 \exp(-\beta d)$

[§] $k_{app}^0 = \frac{RT}{n^2F^2cR_{ct}A}$

used was 0.38Å^{-1}. Using this β, the difference between k^0_{th} and k^0_{app} is reduced to less than two orders of magnitude (tables 5.2).

The differences between k^0_{th} and k^0_{app} can only be explained assuming that the electroactive couple ions diffuse through defects in the structure formed; electron transfer occurs via a tunnelling process across a relative thin film.[17] The diffusion through the thin film is the rate limiting step, otherwise the Nyquist plots would not show only a semi-ellipse for the Faradaic charge transfer.[17]

Table 5.2 – Thickness, apparent electron transfer rate constant and standard rate constant caused by tunnelling for the different unmodified films. The thickness of the films is around 4.5 nm.

		d/nm	k_{th}^0/(cm s^{-1})		k_{app}^0/(cm s^{-1})
			β=0.72Å^{-1}	β=0.38Å^{-1}	
$Fe(CN)_6^{3-/4-}$	tBLM	4.3±0.4	(8.56±0.85)x10^{-16}	(2.16±0.20)x10^{-9}	(9.36±0.18)x10^{-8}
	psBLM	4.3±0.4	(1.05±0.10)x10^{-15}	(2.42±0.25)x10^{-9}	(6.99±0.14)x10^{-8}
$Ru(NH_3)_6^{2+/3+}$	tBLM	4.9±0.5	(2.64±0.25)x10^{-16}	(3.89±0.40)x10^{-9}	(1.13±0.13)x10^{-7}
	psBLM	4.4±0.4	(5.26±0.50)x10^{-15}	(1.89±0.17)x10^{-8}	(1.34±0.14)x10^{-7}
NAD^+/NADH	tBLM	4.2±0.4	(9.88±1.00)x10^{-15}	(1.37±0.14)x10^{-8}	(5.91±0.60)x10^{-8}
	psBLM	4.0±0.4	(4.43±0.40)x10^{-14}	(3.02±0.30)x10^{-8}	(6.89±0.70)x10^{-8}

The quality of the bilayers formed was also evaluated by the average fractional film coverage, θ_a[**], that gives an estimate of the presence of defects in the film. The closer d_a is to d_0 the better the quality of the film. A comparison between d_0 (presented in table 5.2) and d_a (shown in figures 5.18 to 5.21) reveals a range of differences of 2.0 – 2.3 nm for β=0.72 Å^{-1} and around 0.4 nm when β=0.38 Å^{-1}.

[**] $\theta_a = \frac{\left(\frac{k^0_{app}}{k^0_b} - \exp(-\beta d_0)\right)}{(\exp(-\beta d_a) - \exp(-\beta d_0))}$

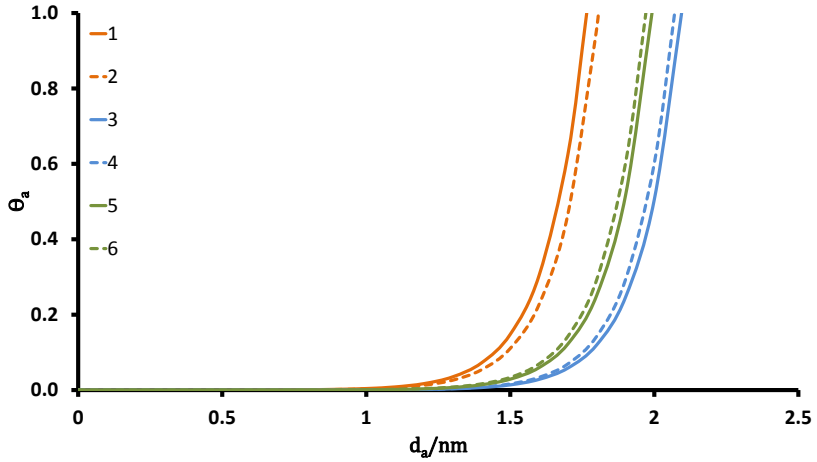

Figure 5.18 – Θ_a vs d_a plots for both types of bilayer in the different electroactive species, using equation 4.12, with β=0.72 Å^{-1}. The full lines are for tBLMs (1, 3 and 5) and the dotted lines are for the psBLMs (2, 4 and 6). Orange: 0.5 mM $Fe(CN)_6^{3-}$ + 0.5 mM $Fe(CN)_6^{4-}$, Blue: 0.5 mM $Ru(NH_3)_6^{3+}$+ 0.5 mM $Ru(NH_3)_6^{2+}$ and Green: 0.25 mM NAD^+ + 0.25 mM NADH.

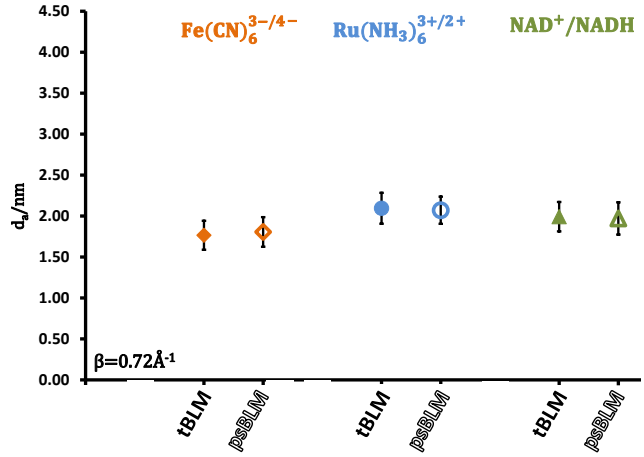

Figure 5.19 – Representation of d_a for the different films, for θ_a=1, using β=0.72 Å^{-1}.

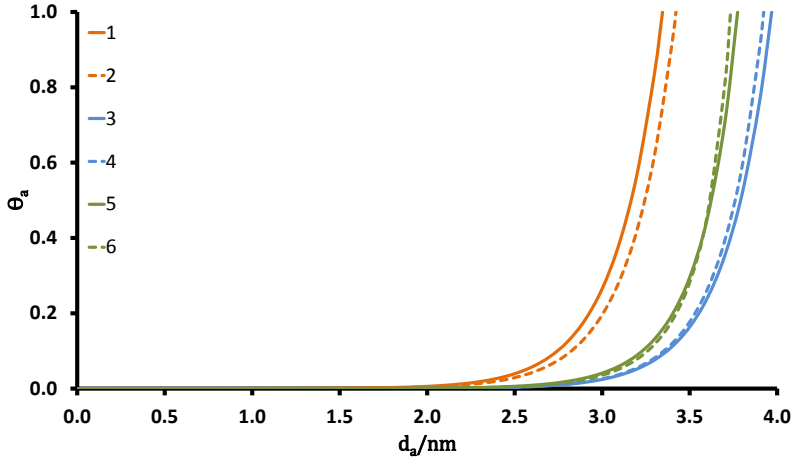

Figure 5.20 – θ_a vs d_a plots for both types of bilayer in the different electroactive species, using equation 4.12, with β=0.38Å^{-1}. The full lines are for tBLMs (1, 3 and 5) and the dotted lines are for the psBLMs (2, 4 and 6). Orange: 0.5 mM $Fe(CN)_6^{3-}$ + 0.5 mM $Fe(CN)_6^{4-}$, Blue: 0.5 mM $Ru(NH_3)_6^{3+}$+ 0.5 mM $Ru(NH_3)_6^{2+}$ and Green: 0.25 mM NAD^+ + 0.25 mM NADH.

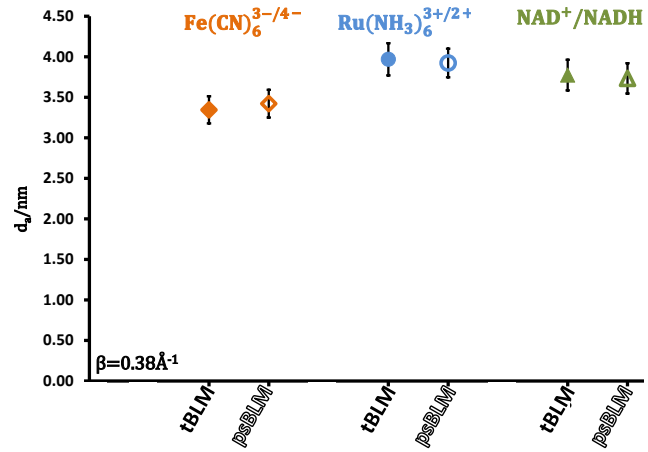

Figure 5.21 – Representation of d_a for the different films, for θ_a=1, using β=0.38 Å^{-1}.

5.2.1.4. Influence of Applied Potential

The study of the influence of the applied potential was made for the tBLMs and for the psBLMs using 0.5 mM $Fe(CN)_6^{3-}$ + 0.5 mM $Fe(CN)_6^{4-}$ and 0.5 mM $Ru(NH_3)_6^{3+}$+ 0.5 mM $Ru(NH_3)_6^{2+}$, with HEPES buffer (pH 7.4) as background. These studies were performed by superimposing a DC potential over the range of the potential window of the electroactive specie in solution (-0.2 V to +0.7 V in the case of $Fe(CN)_6^{3-/4-}$ and -0.5 V to +0.4 V in the

case of $Ru(NH_3)_6^{3+/2+}$, all potentials *vs.* Ag/AgCl, KCl 3.5 M). Like in the case of the SAMs (chapter 4), the capacitance of the films remained approximately constant but the charge transfer resistance changed with the applied potential (figures 5.22 to 5.25). The experimental data was fitted with equation 4.16[††] and yielded growth factors of 4.2 V^{-1} and 1.6 V^{-1} for the tBLMs in $Fe(CN)_6^{3-/4-}$ and $Ru(NH_3)_6^{3+/2+}$, respectively, while the decay factors were 4.9 V^{-1} and 2.0 V^{-1}, in the same order. In case of the psBLMs in $Fe(CN)_6^{3-/4-}$ the growth factor was 1.9 V^{-1} and the decay factor 2.2 V^{-1}, while when a solution of $Ru(NH_3)_6^{3+/2+}$ was studied the growth and decay factors were, respectively, 1.4 V^{-1} and 2.1 V^{-1}.

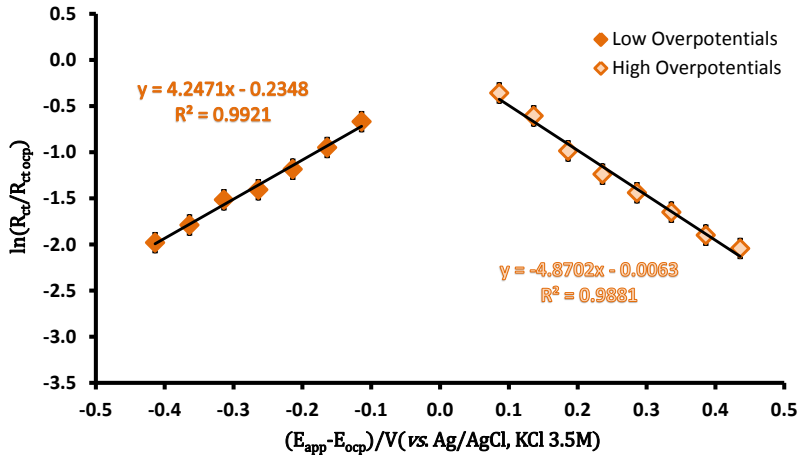

Figure 5.22 – Variation of the charge transfer resistance of the tBLM at different applied overpotentials, in a solution of 0.5 mM $Fe(CN)_6^{3-}$ + 0.5 mM $Fe(CN)_6^{4-}$. The tBLM in $Fe(CN)_6^{3-/4-}$ presents a growth factor of 4.2 V^{-1} and a decay factor of 4.9 V^{-1}, according to equation 4.16.

[††] $R_{ct} = R_{ct\,ocp}\exp[-\gamma(E_{app} - E_{ocp})]$

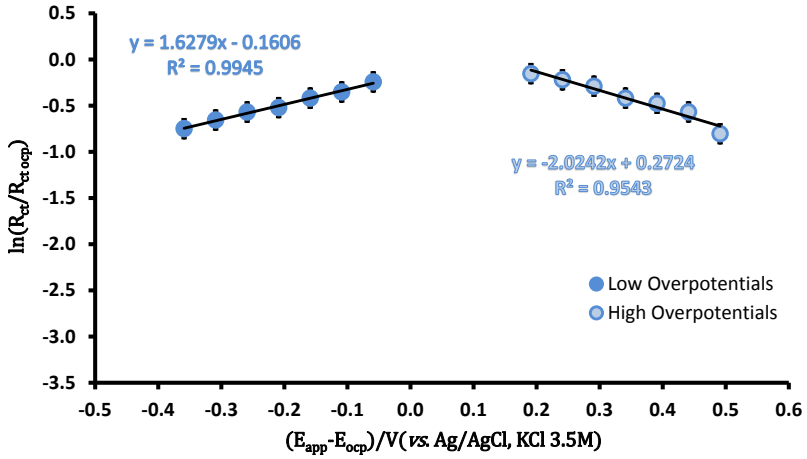

Figure 5.23 – Variation of the charge transfer resistance of the tBLM at different applied overpotentials, in a solution of 0.5 mM $Ru(NH_3)_6^{3+}$ + 0.5 mM $Ru(NH_3)_6^{2+}$. The tBLM in $Ru(NH_3)_6^{3+/2+}$ presents a growth factor of 1.6 V^{-1} and a decay factor of 2.0 V^{-1}, according to equation 4.16.

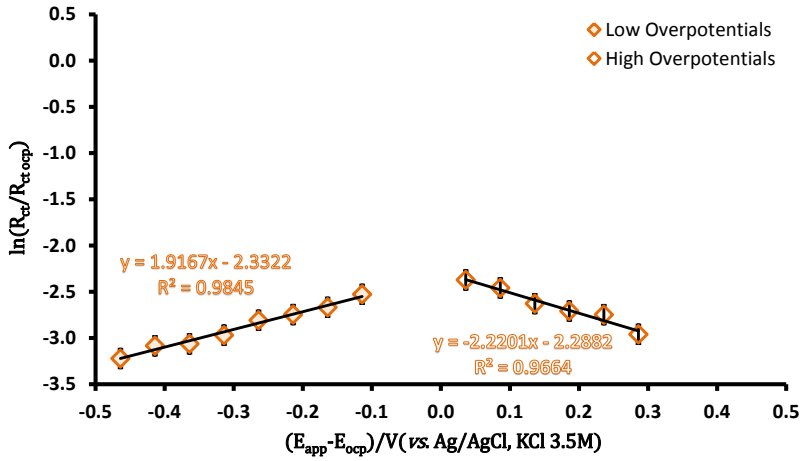

Figure 5.24 – Variation of the charge transfer resistance of the psBLM at different applied overpotentials, in a solution of 0.5 mM $Fe(CN)_6^{3-}$ + 0.5 mM $Fe(CN)_6^{4-}$. The psBLM in $Fe(CN)_6^{3-/4-}$ presents a growth factor of 1.9 V^{-1} and a decay factor of 2.2 V^{-1}, according to equation 4.16.

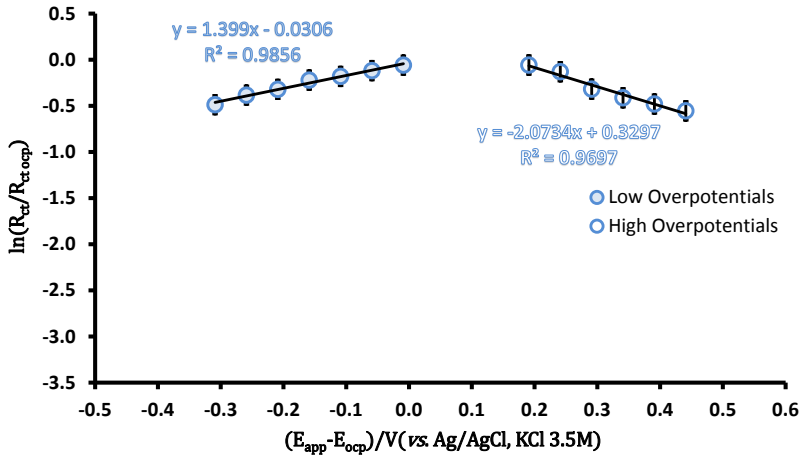

Figure 5.25 – Variation of the charge transfer resistance of the psBLM at different applied overpotentials, in a solution of 0.5 mM $Ru(NH_3)_6^{3+}$ + 0.5 mM $Ru(NH_3)_6^{2+}$. The psBLM in $Ru(NH_3)_6^{3+/2+}$ presents a growth factor of 1.4 V^{-1} and a decay factor of 2.1 V^{-1}, according to equation 4.16.

As shown in chapter 4, the values of the charge transfer coefficient, α, at negative overpotentials can be obtained from the plots of $\ln\left(\frac{R_{ct}}{R_{ct\,ocp}}\right)$ *vs.* η, figures 5.22 to 5.25, and are shown in tables 5.3 and 5.4. k^0_{app} for the negative overpotentials was calculated using equation 4.22[‡‡].

The values of α decrease with increasing overpotentials, in agreement with the Marcus DOS model. At the less negative overpotential (-0.014V for $Fe(CN)_6^{3-/4-}$ and -0.009V for $Ru(NH_3)_6^{3+/2+}$), the k^0_{app} values approach the values presented in table 5.2.[63]

[‡‡] $R_{ct}^{-1} = n^2FfA\left[\overbrace{\alpha\, k^0_{app(a)}\, c_{R,(0)}\, \exp(\alpha n\eta f)}^{negative\ overpotentials} + \underbrace{(1-\alpha)\, k^0_{app(c)}\, c_{O,(0)}\, \exp((1-\alpha)n\eta f)}_{positive\ overpotentials}\right]$

Table 5.3 – α and k^0_{app} for the BLMs, at negative overpotentials, in 0.5 mM $Fe(CN)_6^{3-}$ + 0.5 mM $Fe(CN)_6^{4-}$.

η/V	tBLM			psBLM		
	$\ln(R_{ct}/R_{ct\,ocp})$	α	k^0_{app}/(cm s^{-1})	$\ln(R_{ct}/R_{ct\,ocp})$	α	k^0_{app}/(cm s^{-1})
-0.464	-2.43	0.216	2.59×10^{-4}	-3.22	0.251	7.35×10^{-6}
-0.414	-1.98	0.215	1.06×10^{-4}	-3.08	0.268	4.86×10^{-6}
-0.364	-1.79	0.227	6.50×10^{-5}	-3.06	0.297	3.81×10^{-6}
-0.314	-1.52	0.238	3.44×10^{-5}	-2.97	0.328	2.59×10^{-6}
-0.264	-1.41	0.263	2.26×10^{-5}	-2.81	0.365	1.52×10^{-6}
-0.214	-1.18	0.287	1.21×10^{-5}	-2.75	0.425	9.90×10^{-5}
-0.164	-9.49×10^{-1}	0.321	6.05×10^{-6}	-2.67	0.514	5.80×10^{-5}
-0.114	-6.68×10^{-1}	0.369	2.61×10^{-6}	-2.53	0.655	2.70×10^{-5}
-0.064	-2.73×10^{-1}	0.436	8.50×10^{-7}	-2.42	0.968	9.92×10^{-6}
-0.014	-2.54×10^{-1}	0.819	2.32×10^{-7}	-2.31	2.509	1.19×10^{-6}

Table 5.4 – α and k^0_{app} for the BLMs, at negative overpotentials, in 0.5 mM $Ru(NH_3)_6^{3+}$ + 0.5 mM $Ru(NH_3)_6^{2+}$.

η/V	tBLM			psBLM		
	$\ln(R_{ct}/R_{ct\,ocp})$	α	k^0_{app}/(cm s^{-1})	$\ln(R_{ct}/R_{ct\,ocp})$	α	k^0_{app}/(cm s^{-1})
-0.359	-7.49×10^{-1}	0.175	1.72×10^{-5}	-6.83×10^{-1}	0.172	1.87×10^{-5}
-0.309	-6.56×10^{-1}	0.190	1.22×10^{-5}	-4.88×10^{-1}	0.180	1.15×10^{-5}
-0.259	-5.69×10^{-1}	0.208	8.47×10^{-6}	-3.84×10^{-1}	0.196	7.88×10^{-5}
-0.209	-5.21×10^{-1}	0.237	5.95×10^{-6}	-3.21×10^{-1}	0.221	5.75×10^{-6}
-0.159	-4.18×10^{-1}	0.273	3.66×10^{-6}	-2.21×10^{-1}	0.253	3.42×10^{-6}
-0.109	-3.51×10^{-1}	0.335	2.12×10^{-6}	-1.81×10^{-1}	0.312	2.08×10^{-6}
-0.059	-2.42×10^{-1}	0.448	9.55×10^{-7}	-1.18×10^{-1}	0.421	1.01×10^{-6}
-0.009	-2.19×10^{-1}	0.903	2.24×10^{-7}	-5.89×10^{-2}	0.798	2.49×10^{-7}

5.2.2. Modified films

The modified films (with UQ_{10}, VitE and a mixture of UQ_{10} and VitE) were analysed with NAD^+/NADH as electron mediator in the analyte solution in order to mimic biological electron transfer conditions. The measurements involving the tBLMs were made in degassed solutions, all the measurements were made at room temperature.

5.2.2.1. Cyclic Voltammetry

The characterisation of the modified films was initially done by cyclic voltammetry over a potential range of -1.0 to 1.2V (*vs.* Ag/AgCl, KCl 3.5M). CVs of the films modified with VitE (figures 5.26 and 5.27) and an equimolar mixture of UQ_{10} and VitE (figures 5.28 and 5.29) show that the redox reaction is completely suppressed. This can be attributed to the antioxidant functions of VitE, which suppresses the redox process.[64,65]

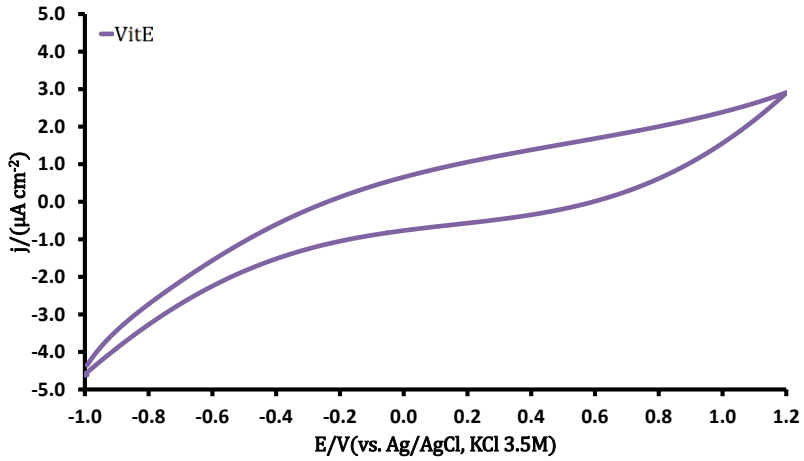

Figure 5.26 – Cyclic voltammograms for the tBLMs modified with VitE in 0.25 mM NAD^+ + 0.25 mM NADH using HEPES buffer (pH 7.4) as background. Scan rate: 50 mV s^{-1}.

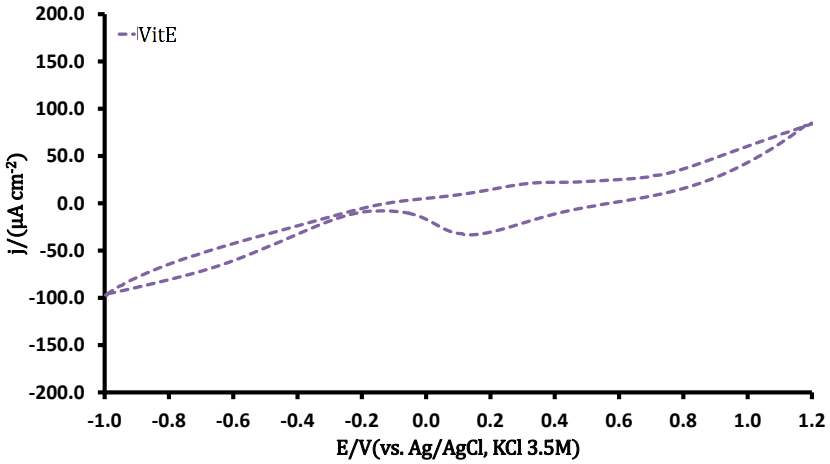

Figure 5.27 – Cyclic voltammograms for the psBLMs modified with VitE in 0.25 mM NAD^+ + 0.25 mM NADH using HEPES buffer (pH 7.4) as background. Scan rate: 50 mV s^{-1}.

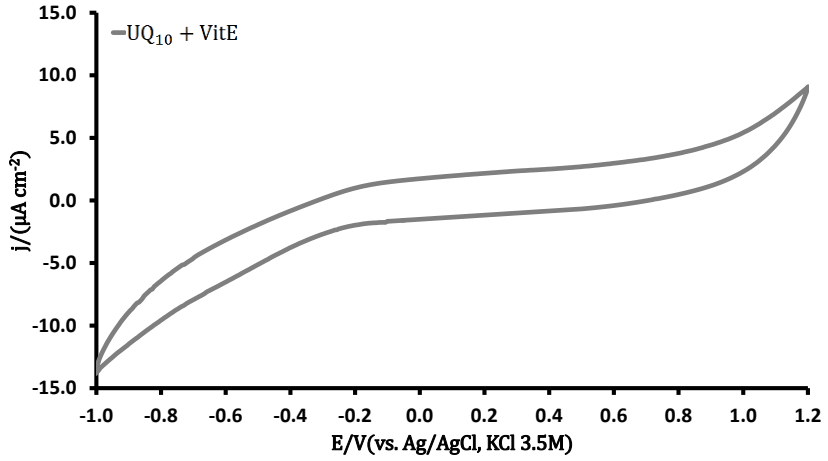

Figure 5.28 – Cyclic voltammograms for the tBLMs modified with UQ_{10}+VitE in 0.25 mM NAD^+ + 0.25 mM NADH using HEPES buffer (pH 7.4) as background. Scan rate: 50 mV s^{-1}.

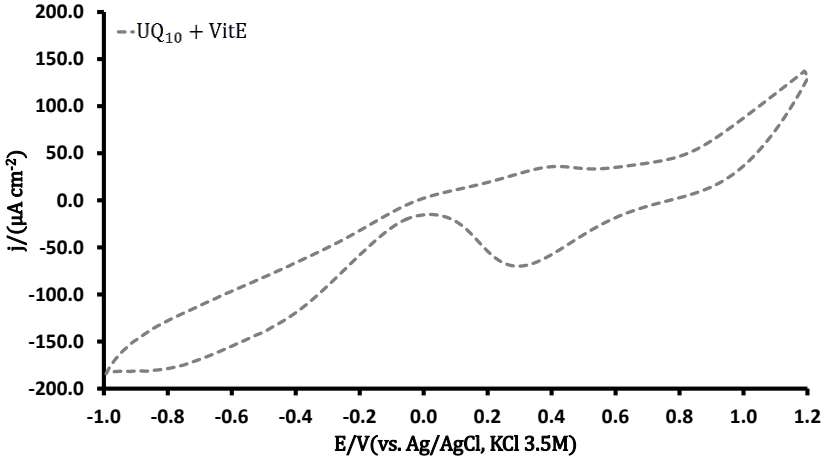

Figure 5.29 – Cyclic voltammograms for the psBLMs modified with UQ_{10}+VitE in 0.25 mM NAD^+ + 0.25 mM NADH using HEPES buffer (pH 7.4) as background. Scan rate: 50 mV s^{-1}.

When only UQ_{10} was used in the modification of the films (figure 5.30 and 5.31), the redox reaction was mediated by the UQ_{10} dissolved in the film.[27] The peak at around 1V corresponds to the oxidation of NADH and the peak between 0.2-0.4V corresponds to the oxidation of $(NAD)_2$ to NAD^+.[49,50] For the psBLM the peaks at around 0.4V correspond to the adsorption of NADH/NAD^+ to the gold surface.[49]

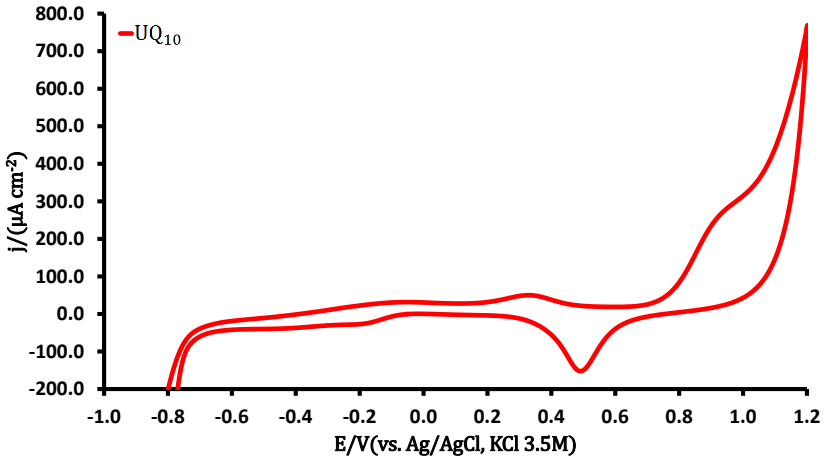

Figure 5.30 – Cyclic voltammograms for the tBLMs modified with UQ_{10} in 0.25 mM NAD^+ + 0.25 mM NADH using HEPES buffer (pH 7.4) as background. Scan rate: 50 mV s^{-1}.

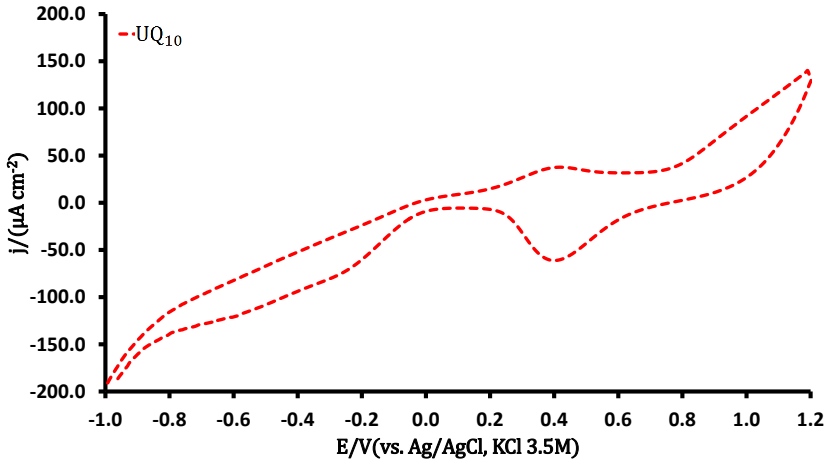

Figure 5.31 – Cyclic voltammograms for the psBLMs modified with UQ_{10} in 0.25 mM NAD^+ + 0.25 mM NADH using HEPES buffer (pH 7.4) as background. Scan rate: 50 mV s^{-1}.

5.2.2.2. Electrochemical Impedance Spectroscopy

When the modification of the films was made only with UQ_{10} the charge transfer resistance decreased, 0.85±0.02 MΩ cm^2 in the case of the tBLMs and 0.22±0.02 MΩ cm^2 for the psBLMs (Table 5.5), when compared to the unmodified films. This can be attributed to the fact that UQ_{10}, which is hydrophobic and sits in the membrane midplane, enables electron transport and redox reactions to occur.[27] The Nyquist plots show a small straight line at low frequencies (figures 5.32 and 5.33) indicating a mass transfer control region and thus Faradaic charge transfer.

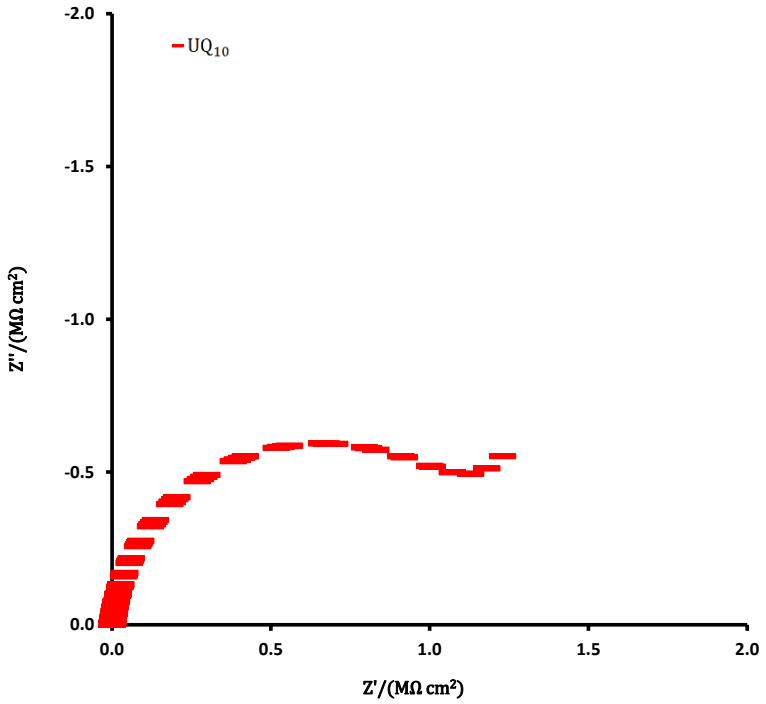

Figure 5.32 – Nyquist plot for the tBLMs modified with UQ_{10} in 0.25 mM NAD^+ + 0.25 mM NADH using HEPES buffer (pH 7.4) as background. In this modification it is possible to observe a mass transfer control region.

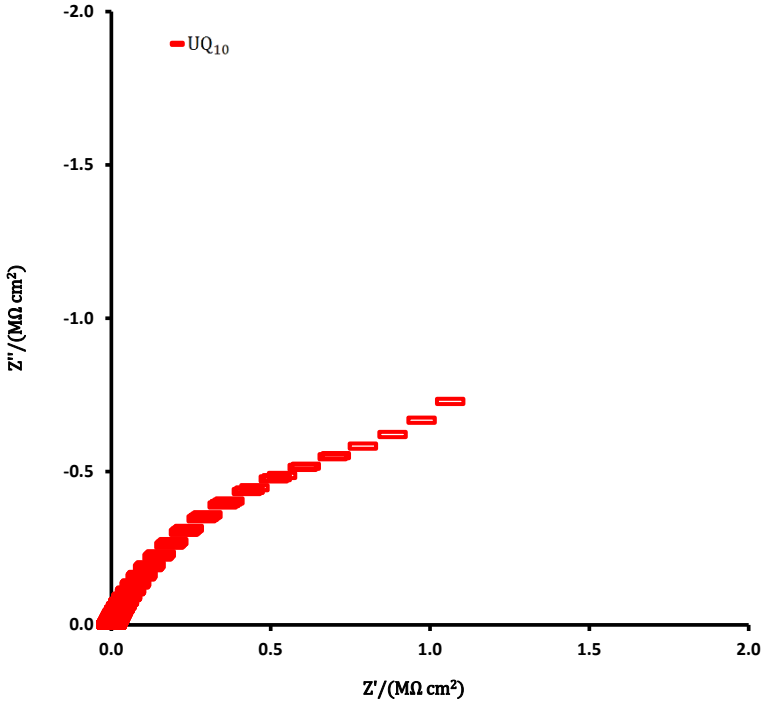

Figure 5.33 – Nyquist plot for the psBLMs modified with UQ_{10} in 0.25 mM NAD^+ + 0.25 mM NADH using HEPES buffer (pH 7.4) as background. In this modification it is possible to observe a mass transfer control region.

In contrast, when VitE was used in the modification of the films (figures 5.34 and 5.35) the charge transfer resistance increased[65] (0.38±0.02 MΩ cm^2 for the tBLMs and 0.05±0.01 MΩ cm^2 in the case of the psBLMs).

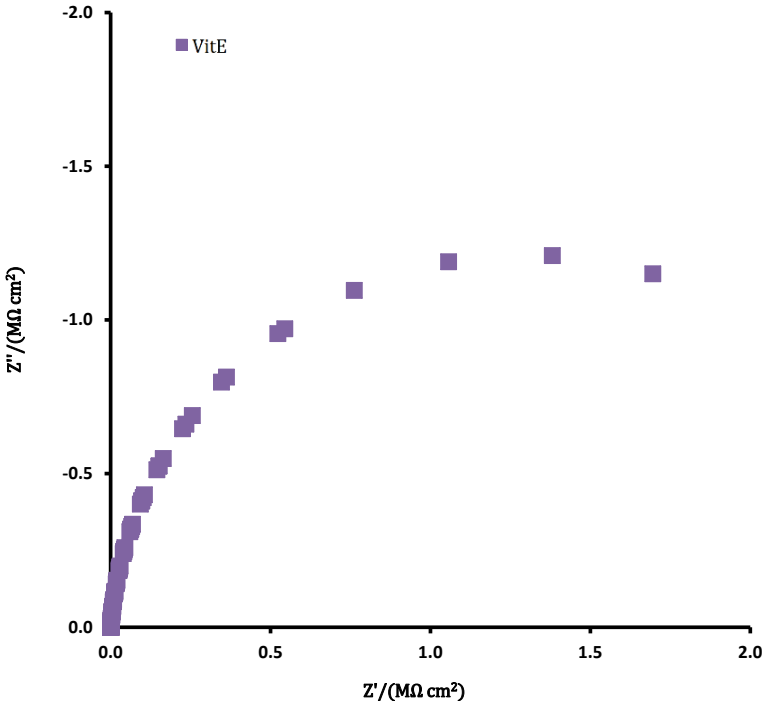

Figure 5.34 – Nyquist plot for the tBLMs modified with VitE in 0.25 mM NAD^+ + 0.25 mM NADH using HEPES buffer (pH 7.4) as background. In this modification only kinetic control is observed.

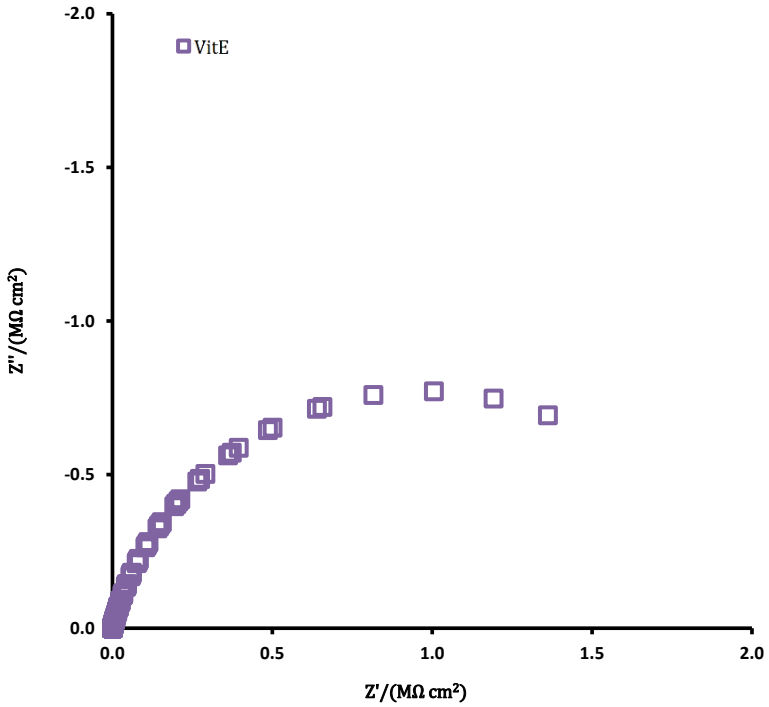

Figure 5.35 – Nyquist plot for the psBLMs modified with VitE in 0.25 mM NAD^+ + 0.25 mM NADH using HEPES buffer (pH 7.4) as background. In this modification only kinetic control is observed.

It is interesting to note that the increment in the charge transfer resistance was smaller (0.12 ± 0.01 MΩ cm^2 for the tBLMs and 0.02 MΩ cm^2 for the psBLMs) when an equimolar mixture of VitE and UQ_{10} was used to make the modification (Table 5.5). Another interesting point is that for the films modified with the equimolar mixture of VitE and UQ_{10}, the electron transfer due to the UQ_{10} was fully supressed. The Nyquist plots show a semi-ellipse in the entire frequency range (figures 5.36 and 5.37), which is in agreement with the observations made using cyclic voltammetry, this was attributable to the antioxidant functions of VitE.[33,64,65]

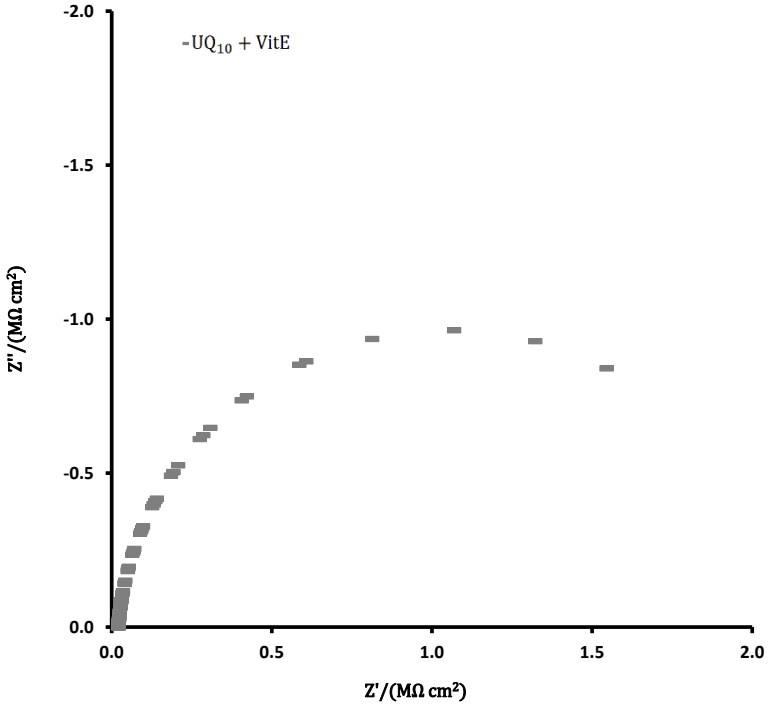

Figure 5.36 – Nyquist plot for the tBLMs modified with UQ_{10}+VitE in 0.25 mM NAD^+ + 0.25 mM NADH using HEPES buffer (pH 7.4) as background. In this modification, even though UQ_{10} is present, only kinetic control is observed.

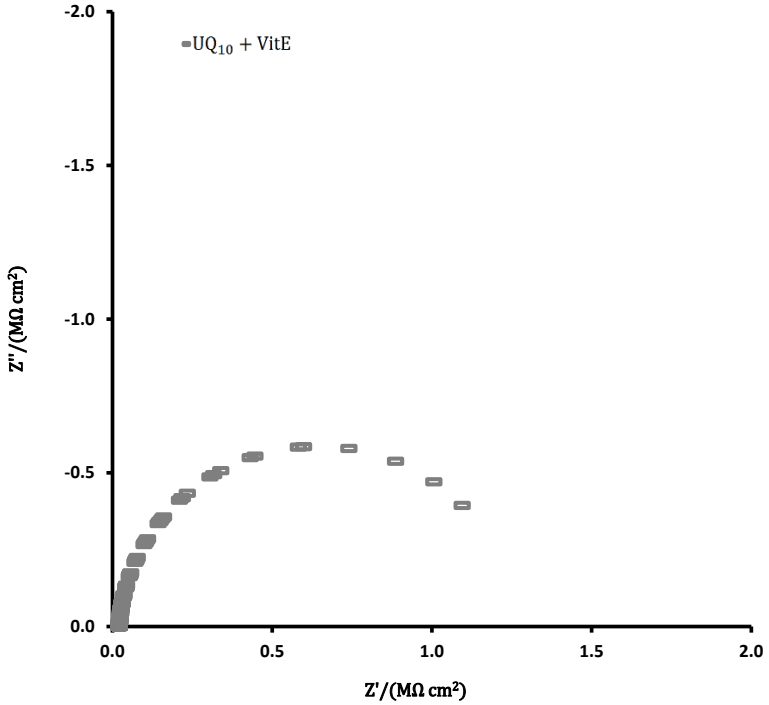

Figure 5.37 – Nyquist plot for the psBLMs modified with UQ_{10}+VitE in 0.25 mM NAD^+ + 0.25 mM NADH using HEPES buffer (pH 7.4) as background. In this modification, even though UQ_{10} is present, only kinetic control is observed.

Table 5.5 – Normalized capacitance and charge transfer resistance of the films modified with UQ_{10}, VitE and a mixture of both. The values here presented indicate that the structures formed were bilayers.

		$C_{layer\ ocp}/(\mu F\ cm^{-2})$	$R_{ct}/(M\Omega\ cm^2)$
tBLM	Unmodified	0.44±0.03	2.22±0.17
	UQ_{10}	0.47±0.04	1.37±0.15
	VitE	0.43±0.03	2.60±0.25
	UQ_{10}+VitE	0.43±0.03	2.34±0.23
psBLM	Unmodified	0.47±0.04	1.90±0.17
	UQ_{10}	0.45±0.05	1.68±0.16
	VitE	0.45±0.04	1.95±0.19
	UQ_{10}+VitE	0.47±0.04	1.92±0.18

5.2.3. Electron Transfer Kinetics

The charge transfer kinetics and the existence of defects caused by collapse of monolayers, which influences the electron transfer kinetics and the quality of the BLM was further analysed. A comparison of electron transfer theory and data was used to investigate this phenomenon in more detail, using EIS data. This analysis was made as in sections 4.2.3. and 5.2.1.3.

The differences between k^0_{th} and k^0_{app} (table 5.6) can only be explained assuming that the electroactive couple ions diffuse through defects in the structure formed; electron transfer occurs via a tunnelling process across a relative thin film.[17] The diffusion through the thin film is the rate limiting step, otherwise the Nyquist plots would not show only a semi-ellipse[17], observed in the films modified with UQ_{10}.

Table 5.6 – Thickness, apparent electron transfer rate constant and standard rate constant caused by tunnelling for the different modified films. The thickness of the films is around 4 nm.

		d/nm	k_{th}^0/(cm s^{-1})		k_{app}^0/(cm s^{-1})
			β=0.72Å^{-1}	β=0.38Å^{-1}	
tBLM	Unmodified	4.2±0.4	(9.88±1.00)x10^{-15}	(1.37±0.14)x10^{-8}	(5.91±0.60)x10^{-8}
	UQ_{10}	3.9±0.4	(6.97±0.70)x10^{-14}	(3.84±0.38)x10^{-8}	(9.54±1.00)x10^{-8}
	VitE	4.3±0.4	(3.66±0.37)x10^{-15}	(8.10±0.80)x10^{-9}	(5.04±0.50)x10^{-8}
	UQ_{10}+VitE	4.2±0.4	(5.21±0.52)x10^{-15}	(9.76±1.00)x10^{-9}	(5.60±0.56)x10^{-8}
psBLM	Unmodified	4.0±0.4	(4.43±0.44)x10^{-14}	(3.02±0.30)x10^{-8}	(6.89±0.70)x10^{-8}
	UQ_{10}	3.7±0.4	(2.57±0.26)x10^{-13}	(7.65±0.77)x10^{-8}	(7.81±0.78)x10^{-8}
	VitE	4.1±0.4	(2.01±0.20)x10^{-14}	(1.99±0.20)x10^{-8}	(6.72±0.67)x10^{-8}
	UQ_{10}+VitE	3.9±0.4	(6.24±0.62)x10^{-14}	(3.62±0.36)x10^{-8}	(6.83±0.68)x10^{-8}

Like in section 5.2.1.3., two values of β were used. Resembling the case of the unmodified films, the differences between d_a and d_0 are 2.2±0.2 nm for β=0.72 Å^{-1} (figure 5.38 and table 5.6) and around 0.4 nm when β=0.38 Å^{-1} (figure 5.39 and table 5.6).

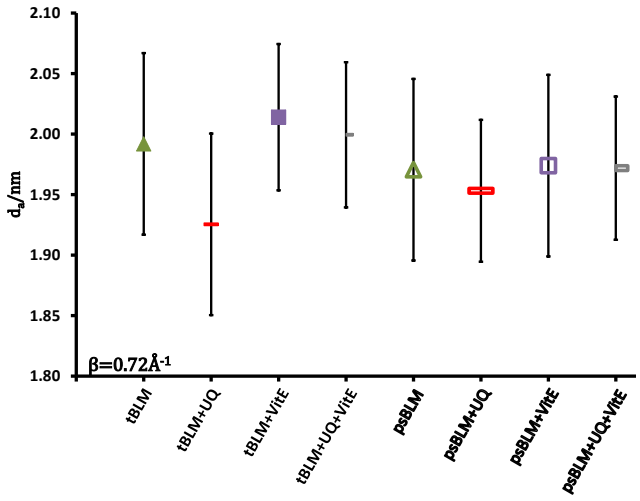

Figure 5.38 – Representation of d_a for the different modifications, for θ_a=1, using β=0.72 Å^{-1}.

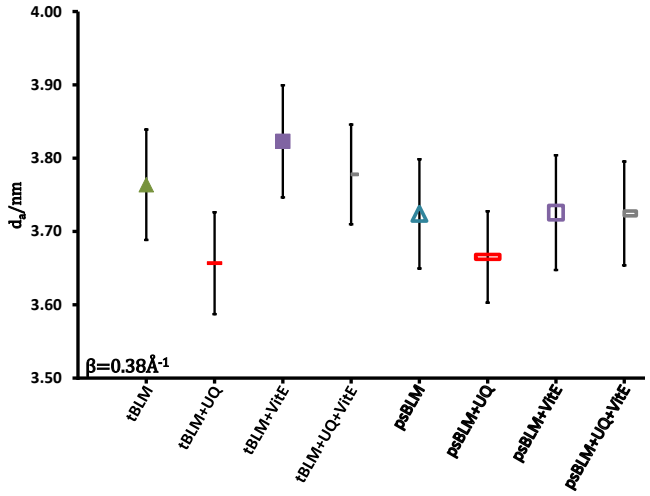

Figure 5.39 – Representation of d_a for the different modifications, for $\theta_a=1$, using $\beta=0.38$ Å^{-1}.

5.3. Conclusion

Electron transfer across phospholipid bilayers (tBLMs and psBLMs) were measured using EIS with three different probe molecules. The capacitance and charge transfer resistance presented in this chapter are consistent with previously reported values. No significant differences were observed between outer $\left(Ru(NH_3)_6^{3+/2+}\right)$ and inner $\left(Fe(CN)_6^{3-/4-}\right)$ sphere electron transfer mechanisms or between these and the biological co – factor NAD^+/NADH.

The analysis and fitting of the experimental values to the theoretical values lead to the use of two different values of the potential independent electron tunnelling coefficient. The difference between the apparent and the standard rate constant caused by electron tunnelling is much smaller when β is close to one-half of that previously reported[18], as was also shown by Mirkin and Bard.[62] Therefore, is concluded that β for electron tunnelling through a phospholipid bilayer is of the order of 0.38 Å^{-1}.

The kinetics of electron transfer across phospholipid bilayers mediated by UQ_{10} was measured as 10^{-8} cm s^{-1}. Electron transfer does not occur when the films were modified with VitE or an equimolar mixture of UQ_{10} and VitE.

Both pore suspended and supported films are essentially porous films. Therefore, is concluded that the same pore model that is used to analyse electron transfer in SAMs and tBLMs is applicable psBLMs.

References

(1) Tien, H. T.; Ottova, A. L. *J. Membr. Sci.* **2001**, *189*, 83–117.
(2) Sackmann, E. *Science* **1996**, *271*, 43–48.
(3) Koper, I. *Mol. Biosyst.* **2007**, *3*, 651–657.
(4) Castellana, E. T.; Cremer, P. S. *Surf. Sci. Rep.* **2006**, *61*, 429–444.
(5) von Heijne, G.; Rees, D. *Curr. Opin. Struct. Biol.* **2008**, *18*, 403–405.
(6) Plant, A. L. *Langmuir* **1993**, *9*, 2764–2767.
(7) Tien, H. T.; Ottova, A. L. *Colloids Surf., A* **1999**, *149*, 217–233.
(8) Junghans, A.; Koper, I. *Langmuir* **2010**, *26*, 11035–11040.
(9) Janshoff, A.; Steinem, C. *Anal. Bioanal.Chem.* **2006**, *385*, 433–451.
(10) Shiba, H.; Maeda, K.; Ichieda, N.; Kasuno, M.; Yoshida, Y.; Shirai, O.; Kihara, S. *J. Electroanal. Chem.* **2003**, *556*, 1–11.
(11) Favero, G.; D'Annibale, A.; Campanella, L.; Santucci, R.; Ferri, T. *Anal. Chim. Acta* **2002**, *460*, 23–34.
(12) Ozaki, S.; Shirai, O.; Kihara, S.; Kano, K. *Electrochem. Commun.* **2007**, *9*, 2266–2270.
(13) Lang, H.; Duschl, C.; Vogel, H. *Langmuir* **1994**, *10*, 197–210.
(14) Vallejo, A. E.; Gervasi, C. A. *Bioelectrochemistry* **2002**, *57*, 1–7.
(15) Cannes, C.; Kanoufi, F.; Bard, A. J. *J. Electroanal. Chem.* **2003**, *547*, 83–91.
(16) Krysinski, P.; Zebrowska, A.; Palys, B.; Lotowski, Z. *J. Electrochem. Soc.* **2002**, *149*, E189–E194.
(17) Diao, P.; Jiang, D.; Cui, X.; Gu, D.; Tong, R.; Zhong, B. *Bioelectrochem. Bioenerg.* **1999**, *48*, 469–475.
(18) Diao, P.; Jiang, D.; Cui, X.; Gu, D.; Tong, R.; Zhong, B. *Bioelectrochem. Bioenerg.* **1998**, *45*, 173–179.
(19) Finklea, H. O.; Avery, S.; Lynch, M.; Furtsch, T. *Langmuir* **1987**, *3*, 409–413.
(20) Jadhav, S. R.; Sui, D.; Garavito, R. M.; Worden, R. M. *J. Colloid Interface Sci.* **2008**, *322*, 465–472.
(21) Wilburn, J. P.; Wright, D. W.; Cliffel, D. E. *Analyst* **2006**, *131*, 311–316.
(22) Shirai, O.; Yoshida, Y.; Kihara, S.; Ohnuki, T.; Uehara, A.; Yamana, H. *J. Electroanal. Chem.* **2006**, *595*, 53–59.
(23) Sandison, M. E.; Zagnoni, M.; Abu-Hantash, M.; Morgan, H. *J. Micromech. Microeng.* **2007**, *17*, S189–S196.
(24) Malmstadt, N.; Nash, M. A.; Purnell, R. F.; Schmidt, J. J. *Nano Lett.* **2006**, *6*, 1961–1965.
(25) Lehninger, A.; Nelson, D.; Cox, M. *Lehninger Principles of Biochemistry*; 5th ed.; W. H. Freeman, 2008.
(26) Gordillo, G. J.; Schiffrin, D. J. *Faraday Discuss.* **2000**, *116*, 89–107.
(27) Cheng, Y.; Cunnane, V. J.; Kontturi, A.-K.; Kontturi, K.; Schiffrin, D. J. *J. Phys. Chem.* **1996**, *100*, 15470–15477.
(28) Crane, F. L.; Sun, I. L.; Barr, R.; Löw, H. *J. Bioenerg. Biomembr.* **1991**, *23*, 773–803.
(29) Söderhäll, J. A.; Laaksonen, A. *J. Phys. Chem. B* **2001**, *105*, 9308–9315.
(30) Afri, M.; Ehrenberg, B.; Talmon, Y.; Schmidt, J.; Cohen, Y.; Frimer, A. A. *Chem. Phys. Lipids* **2004**, *131*, 107–121.
(31) Constantinescu, A.; Maguire, J. J.; Packer, L. *Mol. Aspects Med.* **1994**, *15, Supplement 1*, s57–s65.
(32) Kamal-Eldin, A.; Appelqvist, L.-Å. *Lipids* **1996**, *31*, 671–701.
(33) Traber, M. G.; Atkinson, J. *Free Radical Biol. Med.* **2007**, *43*, 4–15.

(34) Urano, S.; Iida, M.; Otani, I.; Matsuo, M. *Biochem. Biophys. Res. Commun.* **1987**, *146*, 1413–1418.
(35) Kagan, V.; Fabisiak, J.; Quinn, P. *Protoplasma* **2000**, *214*, 11–18.
(36) May, J. M. *Front Biosci* **1998**, *2*, d1 – 10.
(37) Mukai, K.; Itoh, S.; Morimoto, H. *J. Biol. Chem.* **1992**, *267*, 22277–22281.
(38) Stocker, R.; Keaney, J. F. *Physiol. Rev.* **2004**, *84*, 1381–1478.
(39) Gille, L.; Rosenau, T.; Kozlov, A. V.; Gregor, W. *Biochem. Pharmacol.* **2008**, *76*, 289–302.
(40) Gregor, W.; Staniek, K.; Nohl, H.; Gille, L. *Biochem. Pharmacol.* **2006**, *71*, 1589–1601.
(41) Marchal, D.; Boireau, W.; Laval, J. M.; Moiroux, J.; Bourdillon, C. *Biophys. J.* **1997**, *72*, 2679–2687.
(42) Haddox, R. M.; Finklea, H. O. *J Electroanal Chem* **2003**, *550–551*, 351–358.
(43) Lymar, S. V.; Hurst, J. K. *J. Am. Chem. Soc.* **1992**, *114*, 9498–9503.
(44) Patterson, B. C.; Thompson, D. H.; Hurst, J. K. *J. Am. Chem. Soc.* **1988**, *110*, 3656–3657.
(45) Hammarstroem, L.; Almgren, M.; Lind, J.; Merenyi, G.; Norrby, T.; Aakermark, B. *J. Phys. Chem.* **1993**, *97*, 10083–10091.
(46) Hammarstroem, L.; Almgren, M.; Norrby, T. *J. Phys. Chem.* **1992**, *96*, 5017–5024.
(47) Elving, P. J.; Bresnahan, W. T.; Moiroux, J.; Samec, Z. *Bioelectrochem. Bioenerg.* **1982**, *9*, 365–378.
(48) Dawson, R. M. C.; Elliott, D. C.; Elliott, W. H.; Jones, K. M. In *Data for biochemical research*; Oxford University Press, Inc: New York, 1986.
(49) Gordon, L.; Dominguez, E. In *Bioelectrochemistry*; Encyclopedia of Electrochemistry; Wiley-VCH: Weinheim, 2002; Vol. 9, pp. 67–143.
(50) Samec, Z.; Elving, P. J. *J. Electroanal. Chem. Interfacial Electrochem.* **1983**, *144*, 217–234.
(51) Xing, X.; Shao, M.; Liu, C.-C. *J. Electroanal. Chem.* **1996**, *406*, 83–90.
(52) Damian, A.; Omanovic, S. *J. Mol. Catal. A: Chem.* **2006**, *253*, 222–233.
(53) Vockenroth, I. K.; Atanasova, P. P.; Long, J. R.; Jenkins, A. T. A.; Knoll, W.; Köper, I. *Biochim. Biophys. Acta, Biomembr.* **2007**, *1768*, 1114–1120.
(54) Naumowicz, M.; Figaszewski, Z. *Bioelectrochemistry* **2003**, *61*, 21–27.
(55) Plant, A. L.; Gueguetchkeri, M.; Yap, W. *Biophys. J.* **1994**, *67*, 1126–1133.
(56) Schiller, S. M.; Naumann, R.; Lovejoy, K.; Kunz, H.; Knoll, W. *Angew. Chem. Int. Ed.* **2003**, *42*, 208–211.
(57) Jeuken, L. J. C.; Bushby, R. J.; Evans, S. D. *Electrochem. Commun.* **2007**, *9*, 610–614.
(58) Steinem, C.; Janshoff, A.; Ulrich, W.-P.; Sieber, M.; Galla, H.-J. *Biochim. Biophys. Acta, Biomembr.* **1996**, *1279*, 169–180.
(59) Dilger, J.; McLaughlin, S.; McIntosh, T.; Simon, S. *Science* **1979**, *206*, 1196 –1198.
(60) Long, Y.-T.; Li, C.-Z.; Kraatz, H.-B.; Lee, J. S. *Biophys J* **2003**, *84*, 3218–3225.
(61) Wang, S.; Du, D. *Sensors* **2002**, *2*, 41–49.
(62) Tsionsky, M.; Bard, A. J.; Mirkin, M. V. *J. Am. Chem. Soc.* **1997**, *119*, 10785–10792.
(63) Xing, Y. F.; O'Shea, S. J.; Li, S. F. Y. *J. Electroanal. Chem.* **2003**, *542*, 7–11.
(64) Abou-Seif, M. A. M. *Ann. Clin. Biochem.* **1997**, *34*, 645–6650.
(65) Naumowicz, M.; Petelska, A. D.; Figaszewski, Z. A. *Electrochim. Acta* **2009**, *54*, 1089–1094.

6. Bilayer Lipid Membranes Based on the Avidin – Biotin Interaction

Many different procedures have been employed to produce bilayer lipid membranes. In this chapter BLMs are produced taking advantage of the strong avidin – biotin interaction and of the vesicle fusion process. Avidin is deposited in a platinum substrate and then vesicles composed of L-α-phosphatidylcholine and 1,2-dioleoyl-*sn*-glycero-3-phosphoethanolamine-N-(biotinyl) (sodium salt) are burst by applying +0.7 V (*vs.* Ag/AgCl, KCl 3.5 M), leading to the formation of a supported BLM. The vesicles used had methylene blue (MB) inside; its release, when the vesicles burst, was monitored by cyclic voltammetry and UV-Vis. Although its release could not be detected using CV, UV-Vis spectroscopy showed a peak corresponding to MB. The avidin layer and the sBLMs were characterised using cyclic voltammetry and electrochemical impedance spectroscopy, with two different electroactive couples: $Fe(CN)_6^{3-/4-}$ and $Ru(NH_3)_6^{3+/2+}$. The BLMs formed showed a resistance in the MΩ region and a capacitance around 0.8 μF cm^{-2}, indicating that the structure formed is of high quality.

6.1. Introduction

Since Mueller *et al.*[1] reported the reconstitution of a cell membrane structure by means of a biomolecular lipid membrane between two aqueous solutions many advances have been made in the preparation of bilayer lipid membranes (BLMs). One of these developments is the use of solid substrates. The use of a solid support increases not only the stability but also the possibilities in terms of characterisation.[2] Brain and McConnell[3] pioneered this type of BLM almost three decades ago; they showed that phospholipid vesicles fuse to form planar membranes when incubated on treated glass surfaces, figure 6.1. Other hydrophilic surfaces, such as mica,[4,5*] quartz[6,7*] and silicon dioxide,[8,9*] have also been used to produce supported BLMs (sBLMs).

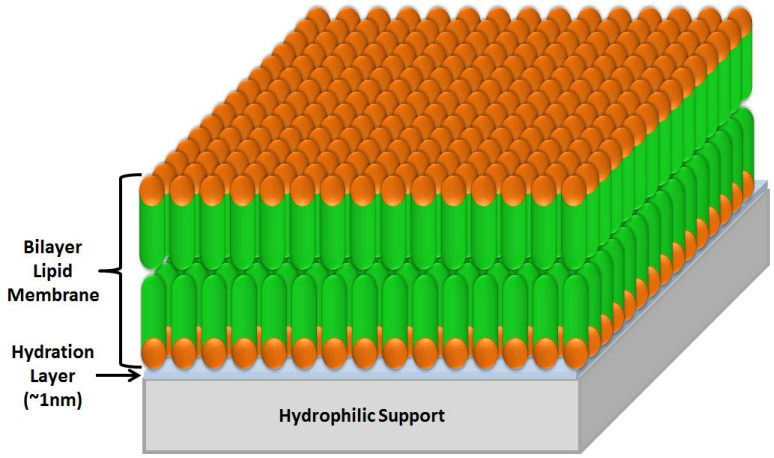

Figure 6.1 – Schematic representation of a solid supported bilayer lipid membrane.

Another improvement that was made in the mimicking of the cell membrane is the use of polymer cushions between the support and the BLM, figure 6.2.[10–12] The use of a soft hydrophilic cushion makes the system a better mimic of the cell membrane and also helps with mobility problems, the immobilisation of lipid bilayers on supports allows a better characterisation of the BLM.[12] Various polymers have been used; Knoll's[10] and

* These references are just examples, there are many more articles published using these supports.

Israelachvili's[12] groups have used polyethylenimine while Sackamnn's[11] group has used polyacrylamide films.

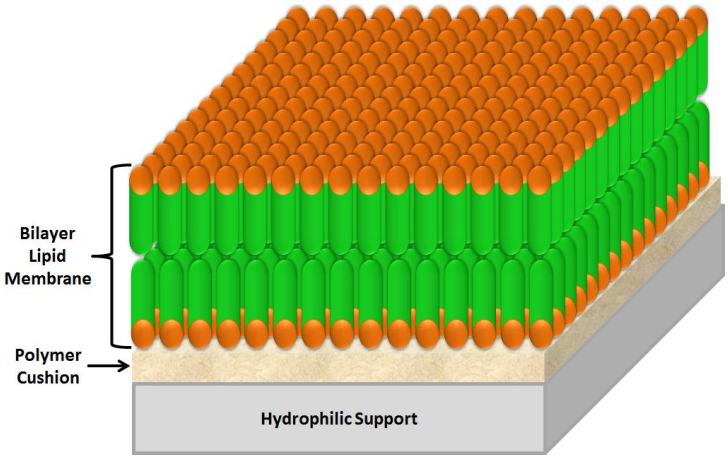

Figure 6.2 – Schematic representation of a solid supported bilayer lipid membrane with a polymer cushion between the solid support and the BLM.

Another cushion that has been used between the BLM and the solid support is avidin or streptavidin.[13–17] Avidin has been used as a cushion mostly in the fabrication of biosensors, and its use is based on the strong avidin – biotin interaction. The dissociation constant between of avidin – biotin is around 10^{-15} M, making it one of the strongest known non-covalent bonds.[18] The binding of biotin to avidin is known to involve the tryptophan and lysine residues present in each subunit of avidin.[19]

Avidin (figure 6.3 a)) is a glycoprotein found in egg whites composed of four identical subunits with a total molecular weight of approximately 66 kDa.[19–21] Each of its subunits has a binding site for biotin and one oligosaccharide modification (mainly mannose and glucosamine[22]).[19,23] Each subunit is organized in an eight-stranded antiparallel orthogonal beta-barrel (figure 6.3 b)), with extended loop regions, which define the biotin binding pocket in the subunit core.[24,25] Avidin is highly basic with an isoelectric point (pI) of about 10.[19]

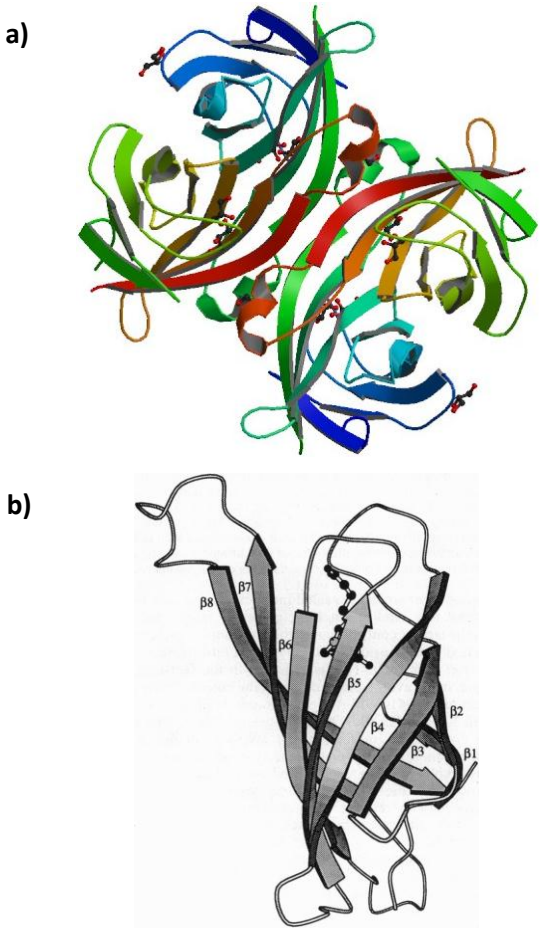

Figure 6.3 – a) Three-dimensional structure of avidin, acquired with x-ray diffraction methods.[26] b) ribbon diagram of the avidin-biotin monomer, with the eight strands of the 3-barrel labelled. Biotin molecule is shown in a ball and stick mode (copyright PNAS, used with permission).[24]

Avidin is extremely resistant to denaturation, even in 8 M urea or 3 M guanidine hydrochloride the protein maintains structural integrity and activity.[18] When avidin is bounded to biotin, the complex is even more stable and it requires 6 – 8 M guanidine – HCl at pH 1.5 to dissociate.[27,28]

Biotin, also known as vitamin H, is a water soluble vitamin composed of an ureido (tetrahydroimidizalone) ring fused with a tetrahydrothiophene ring. A valeric acid substituent is attached to one of the carbon atoms of the tetrahydrothiophene ring (figure 6.4).[29,30]

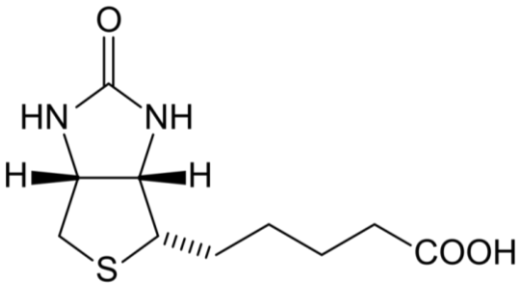

Figure 6.4 – Chemical structure of biotin (5-[(3aS,4S,6aR)-2-oxohexahydro-1H-thieno[3,4-d]imidazol-4-yl]pentanoic acid).

In mammals biotin is an essential nutrient and has roles as carboxyl carrier in carboxylation reactions and in cellular processes including transcription and gene silencing.[29–31]

One problem with the avidin – biotin interaction is that avidin has tendency to bind nonspecifically to other components.[19] To overcome this problem other biotin binding protein can be used. Streptavidin also contains four subunits but has a molecular weight of about 6 kDa smaller than avidin. It has a pI of around 5 – 6, which reduces the nonspecific binding. Another advantage is that streptavidin is not a glycoprotein and this makes it not bind to carbohydrate receptors.[19]

Supported BLMs that use the avidin/streptavidin – biotin interaction were developed by Bourdillon's group[16,17,32] in order to create bilayers of large surface area in porous aluminium oxide supports, this lead to high volume concentration of membrane mimicking chloroplasts or mitochondria.[32] The formation of the BLM involves various steps and starts with the deposition of streptavidin in the aluminium oxide support, then biotinylated vesicles adhere to the streptavidin, finally to promote the formation of the BLM, poly(ethyleneglycol) (PEG) is added to the solution. Jung *et al.*[33] have previously used a similar procedure in gold substrates but they were not interested in the formation of a BLM, they wanted the vesicles to remain intact.

The addition of PEG is necessary because, unlike the case of hydrophobic substrates, the driving forces for the fusion of vesicles are weak and not sufficient to promote fusion. PEG promotes the fusion of the vesicles by osmotic stress; the addition of PEG to the solution makes the vesicles aggregate and deform, due to dehydration, leading to fusion.[34–36]

6.2. Discussion

6.2.1. Bursting of Vesicles to Make Lipid Bilayers

The first step in the production of the sBLMs taking advantage of the avidin – biotin interaction was to make sure that the vesicles would burst by applying potential. Hellberg *et al.*[37] have previously studied this process but using a static mercury electrode. Figure 6.5 is a histogram for the DLS measurement of a 2 mg mL^{-1} solution of 1,2-dioleoyl-*sn*-glycero-3-phosphoethanolamine-N-(biotinyl) (sodium salt) and L-α-phosphatidylcholine (DOPE(B)+EggPC) vesicles, before and after applying +0.7V (*vs.* Ag/AgCl, KCl 3.5M).

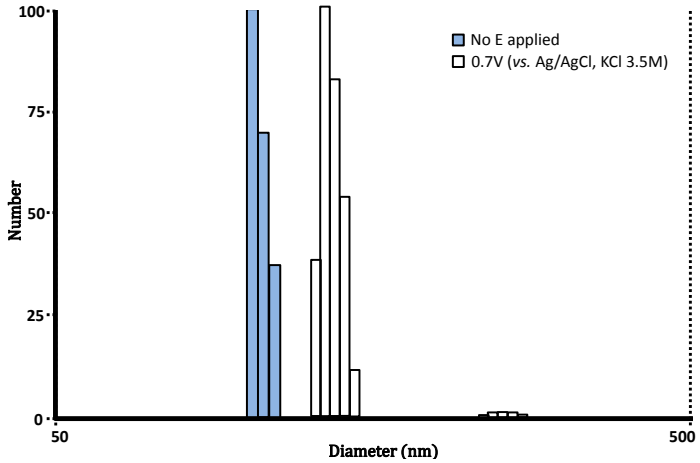

Figure 6.5 – DLS of a 2 mg mL^{-1} solution of DOPE(B)+EggPC vesicles before (blue fill) and after (no fill) +0.7 V (*vs.* Ag/AgCl, KCl 3.5 M) was applied to the solution.

Figure 6.5 shows that the vesicles change in size, and also the size distribution is not as uniform as it was before, when potential was applied to the solution. The average diameter of the vesicles went from 110±4.0 nm to 178±24 nm and the polydispersity

changed from 0.119±0.011 to 0.456±0.032 when potential was applied to the solution. This change in diameter and polydispersity leads to the conclusion that the vesicles did burst when potential was applied.

Dynamic Light Scattering[38,39]

Dynamic light scattering, also known as photon correlation spectroscopy, is one of the most popular methods to determine the size of particles. When light hits matter, an oscillating polarisation of electrons in the molecules is induced by the electric field of the light. The molecules will then produce a second source of light and subsequently scatter light. The size, shape and molecular interactions determine the frequency shifts, the angular distribution, the polarisation and the intensity of the scatter light. Thanks to this is possible to get information about the structure and molecular dynamics of the scattering medium (particles).

A dynamic light scattering experiment is based on two assumptions:

i) the particles are in Brownian motion (random drifting of particles suspended in a fluid (a liquid or a gas)); in this case the probability density function is given by,

$$P(r,t|0,0) = (4\pi Dt)^{-3/2} \exp\left(\frac{-r^2}{4Dt}\right)$$

where D is the diffusion coefficient.

ii) The particles are spherical with a small diameter compared to the molecular dimensions; being so, is possible to apply the Stokes – Einstein relation,

$$D = \frac{k_B T}{6\pi\eta a}$$

where a is the radius of the particles, k_B the Boltzmann constant, T the temperature (K) and η the viscosity of the solvent.

6.2.2. Characterisation of the Avidin Layer

The deposition of the avidin layer on the Pt electrodes was done by dipping the electrodes in avidin solution (10mg mL^{-1} in 0.1 M PBS, pH=7.4[40]) and applying 200 V s^{-1} of an alternating potential with triangular waveform from -0.5 to +2.1 V (*vs.* Ag/AgCl, KCl 3.5 M) for 10 minutes. The electrode was then rinsed with PBS to remove weakly attached avidin.[20,21,41,42] Avidin is adsorbed to Pt, and as well to Au or Ag surfaces, through a hydrophobic or ligating interaction that leads to the formation of a monolayer. This is a process that occurs spontaneously but is slow. By applying a potential with triangular shape the time of adsorption is decreased to just a few minutes. This process, like any other, has its advantages and disvantages; on the bright side this leads to the formation of a monolayer on the Pt surface, the problem is the orientation of the avidin molecules that cannot be controlled.[43,44]

The adsorption kinetics and/or thermodynamics of avidin, and other proteins, depends on the electrical or electrochemical properties of the solid support on which the protein is adsorbed

The characterisation of the avidin layer was done by CV and EIS using two redox couples, $Fe(CN)_6^{3-/4-}$ and $Ru(NH_3)_6^{3+/2+}$. Figures 6.6 and 6.7 refer to the characterization using 0.5 mM $Fe(CN)_6^{3-}$ + 0.5 mM $Fe(CN)_6^{4-}$, 100 mM PBS (pH=7.4) as background. From figure 6.6 it is observable that the redox reaction is completely inhibited. That is confirmed by the EIS spectra, the Nyquist plot shows a semi-ellipse in the entire frequency range (1.0×10^5 – 0.1 Hz).

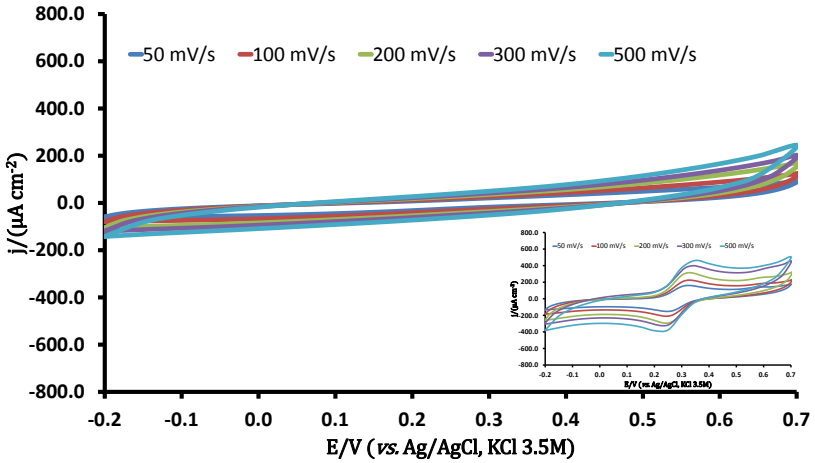

Figure 6.6 – Characterisation of the avidin layer, deposited on the Pt electrodes, using CV. The measurements were made in 0.5 mM $Fe(CN)_6^{3-}$ + 0.5 mM $Fe(CN)_6^{4-}$, in 100 mM PBS (pH=7.4) as background. The absence of anodic and cathodic peaks indicates that the redox reaction is completely inhibited. The inset shows the characterisation of the bare electrode.

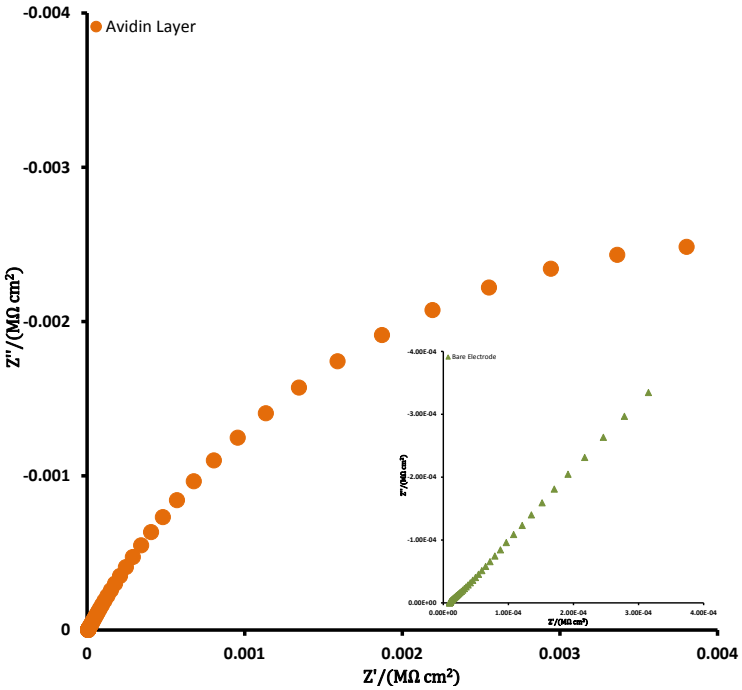

Figure 6.7 – Characterisation of the avidin layer, deposited on the Pt electrodes, using EIS. The measurements were done at OCP of the redox couple, $Fe(CN)_6^{3-/4-}$ in this case. The semi-ellipse in the entire frequency range indicates that the redox reaction is completely inhibited. The inset shows the characterisation of the bare electrode.

Regarding the characterisation with 0.5 mM $Ru(NH_3)_6^{3+}$ + 0.5 mM $Ru(NH_3)_6^{2+}$ in 100 mM PBS (pH=7.4), the redox reaction is not completely inhibited as can be seen in figure 6.8. Also the Nyquist plot (figure 6.9) does not show a semi-ellipse in the entire frequency range, indicating that electron transfer is possible.

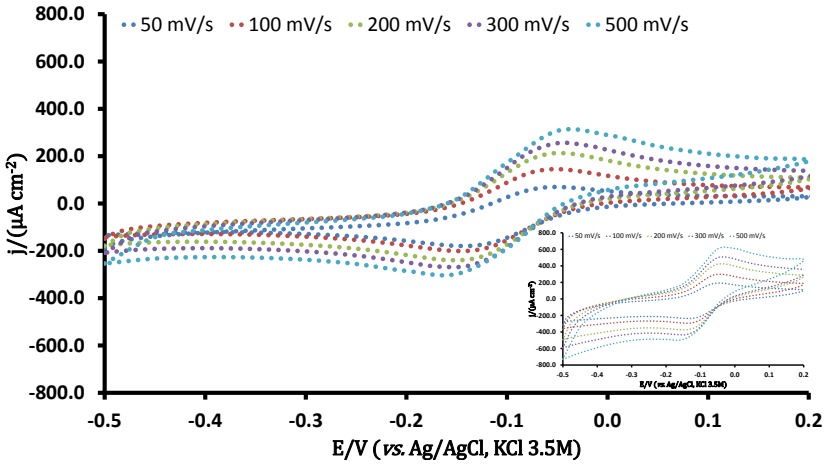

Figure 6.8 – Characterisation of the avidin layer, deposited on the Pt electrodes, using CV. The measurements were made in 0.5 mM $Ru(NH_3)_6^{3+}$ + 0.5 mM $Ru(NH_3)_6^{2+}$, in 100 mM PBS (pH=7.4) as background. The redox reaction is not completely inhibited as is easily observed by the presence of anodic and cathodic peaks. The inset shows the characterisation of the bare electrode.

This difference in behaviour between $Fe(CN)_6^{3-/4-}$ and $Ru(NH_3)_6^{3+/2+}$ can be explained on their electron transfer mechanism. While the first has an inner sphere mechanism, the latter has an outer sphere mechanism.[45–47] The outer sphere electron transfer mechanism allows the electron transfer across, at least, a monolayer of solvent.[46] Bard and co-workers[48] have shown that CVs of ferrocenemethanol, species with outer sphere mechanism, are not influenced by the presence of a monolayer of 3-mercaptopropionic acid on the electrode surface. This monolayer has a thickness of 0.45nm[49] which is around 10 times thinner than a monolayer of avidin (avidin's dimensions are: 56x50x40 Å[50]). While Bard's group reports no difference in the intensity of the CVs,[48] in figure 6.8, it is

possible to observe that the current density in the case of the modified electrode is about one-half of that of bare electrode, the changes in E_p are neglectable.

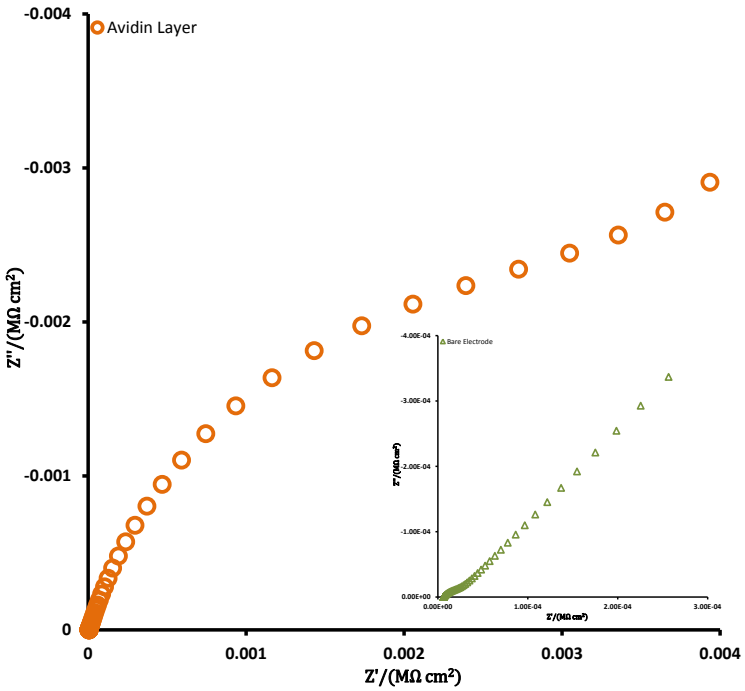

Figure 6.9 – Characterisation of the avidin layer, deposited on the Pt electrodes, using EIS. The measurements were done at OCP of the redox couple, $Ru(NH_3)_6^{3+/2+}$ in this case. The behaviour at low frequencies indicates that the redox reaction is not completely inhibited. The inset shows the characterisation of the bare electrode.

6.2.3. Characterisation of the sBLMs

Figures 6.10 and 6.11 are the cyclic voltammograms after the BLM deposition using $Fe(CN)_6^{3-/4-}$ and $Ru(NH_3)_6^{3+/2+}$, respectively, as electroactive couple. The redox reaction is completely inhibited for both electroactive couples, what is also confirmed by the semi-circle in the entire frequency range of the EIS measurements (figures 6.12 and 6.13). The potential window in figures 6.10 and 6.11 was increased in order to incorporate the region where the redox reaction of the MB occurs. The absence of peaks in the region of the MB redox reaction shows that the MB that is released from the vesicles does not cross the BLM or the avidin layer.

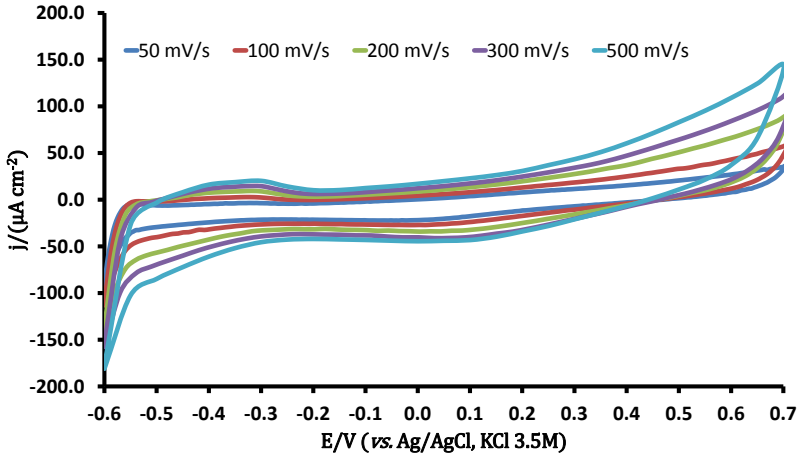

Figure 6.10 – Characterisation of the BLM deposited on the avidin layer, using CV. The measurements were made in 0.5 mM $Fe(CN)_6^{3-}$ + 0.5 mM $Fe(CN)_6^{4-}$, in 100 mM PBS (pH=7.4) as background. Like in the case of the avidin layer, the redox reaction is completely inhibited.

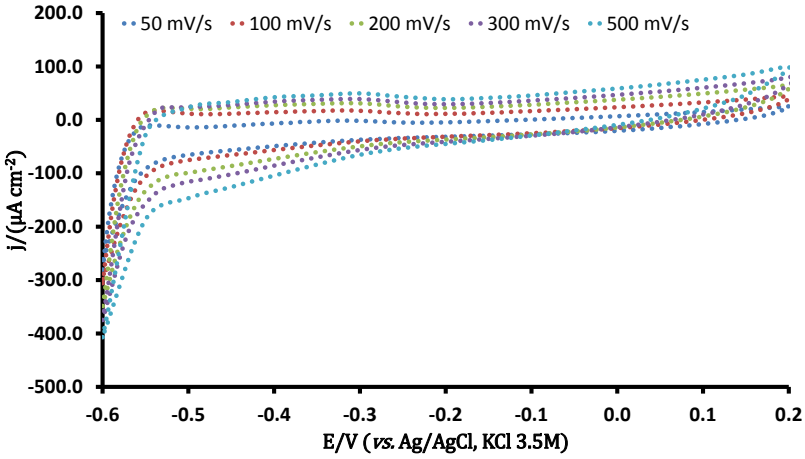

Figure 6.11 – Characterisation of the BLM deposited on the avidin layer, using CV. The measurements were made in 0.5 mM $Ru(NH_3)_6^{3+}$+ 0.5 mM $Ru(NH_3)_6^{2+}$, in 100 mM PBS (pH=7.4) as background. Unlike in the case of the avidin layer, here the redox reaction is completely inhibited.

It is interesting to note in the Nyquist plots, figures 6.12 and 6.13, that at low frequencies it is possible to observe a second semi-circle which corresponds to the avidin layer. The values presented in table 6.1 were extracted by fitting and equivalent circuit to the EIS raw data and show that the structure formed is a bilayer. BLMs should present a resistance in the MΩ cm^2 region[51–56] and a capacitance between 0.4 – 0.8 µF cm^{-2} [52,57–60].

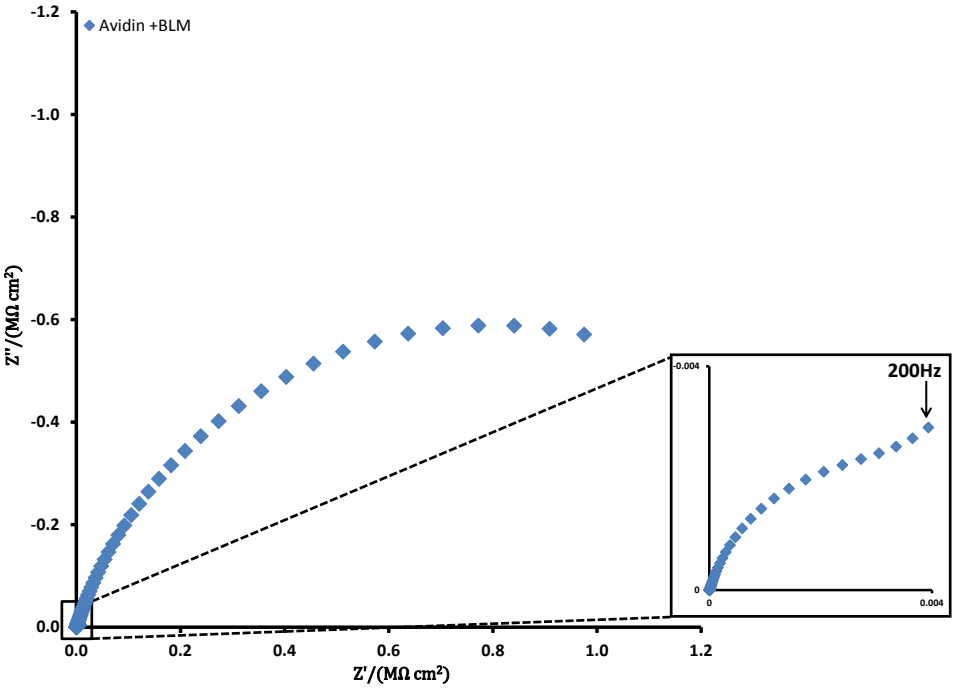

Figure 6.12 – Characterisation of the BLM deposited on the avidin layer, using EIS. The measurements were done at OCP of the redox couple, $Fe(CN)_6^{3-/4-}$ in this case. The semi-circle in the entire frequency range indicates that the redox reaction is completely inhibited. At high frequencies is possible to observe a second semi-circle, this corresponds to the avidin layer.

Table 6.1 – Normalized capacitance and charge transfer resistance of the avidin layer and BLMs. The values here presented indicate that the structures formed are bilayers.

		$C_{layer\ ocp}$/(μF cm^{-2})	R_{ct}/(MΩ cm^2)
$Fe(CN)_6^{3-/4-}$	Avidin Layer	187±15	0.008±0.001
	BLM	0.83±0.08	1.17±0.20
$Ru(NH_3)_6^{2+/3+}$	Avidin Layer	63±6	0.004±0.001
	BLM	0.78±0.08	2.37±0.22

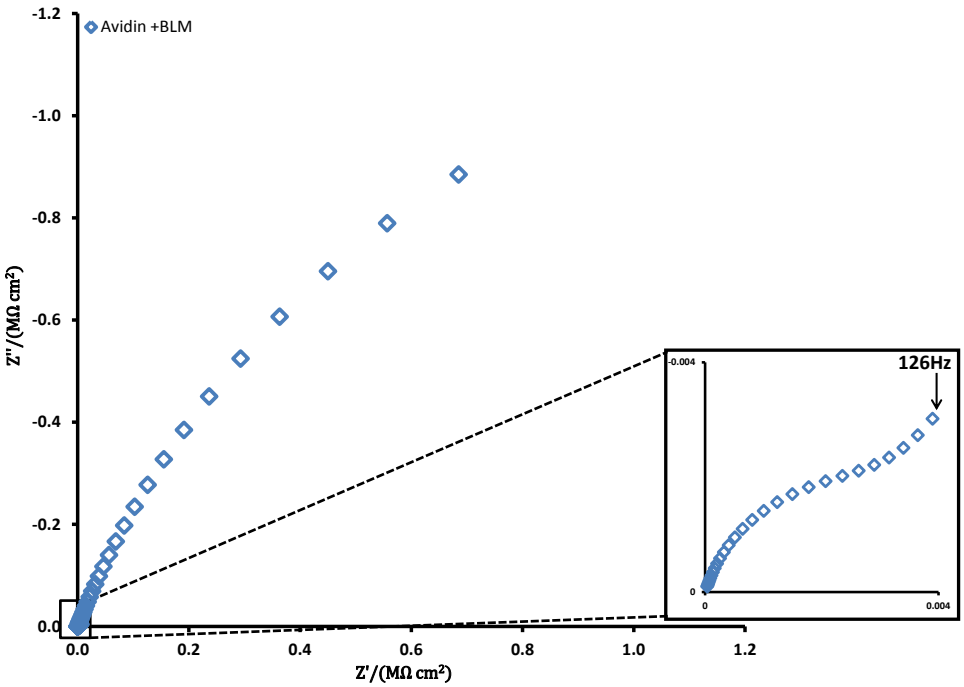

Figure 6.13 – Characterisation of the BLM deposited on the avidin layer, using EIS. The measurements were done at OCP of the redox couple, $Ru(NH_3)_6^{3+/2+}$ in this case. The semi-circle in the entire frequency range indicates that the redox reaction is completely inhibited. At high frequencies is possible to observe a second semi-circle, this corresponds to the avidin layer.

Because the vesicles had methylene blue (MB) inside, a second working electrode was used to detect the presence of MB in the bulk solution, figure 6.14. Although the release of MB due to the vesicle burst is not apparent in the CVs (figure 6.15) it is observable in the UV-Vis spectra (figure 6.16). This might be due to the small concentration of MB in the bulk solution, applying the Beer – Lambert law the determined concentration of MB in the bulk solution due to the burst of vesicles is <0.3 μM. As can be seen in figure 6.17 the minimum amount of MB that is detectable by CV, in this system, is 5 μM.

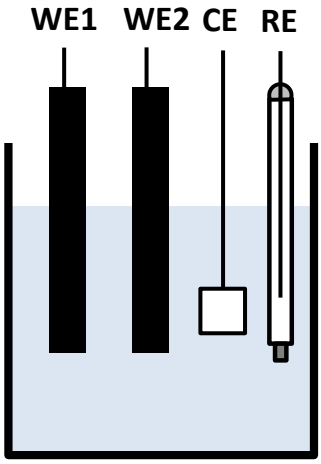

Figure 6.14 – The avidin layer, and thus the BLM, is deposited in WE1. WE2 is used for the detection of MB released when vesicles burst. The electrodes were disposed in a circular way with 1 cm between them.

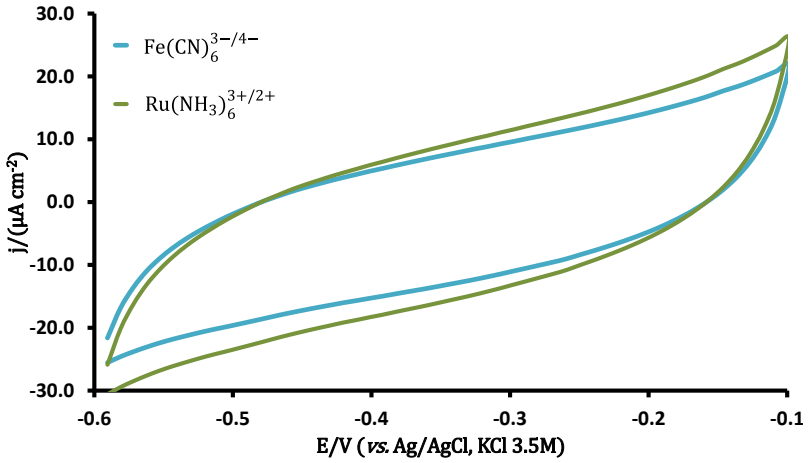

Figure 6.15 – CV for the detection of MB in the bulk solution of $Fe(CN)_6^{3-/4-}$ (blue line) and $Ru(NH_3)_6^{3+/2+}$ (green line) after the bursting of the vesicles. The peaks correspondent to the redox reaction of the MB are not observable.

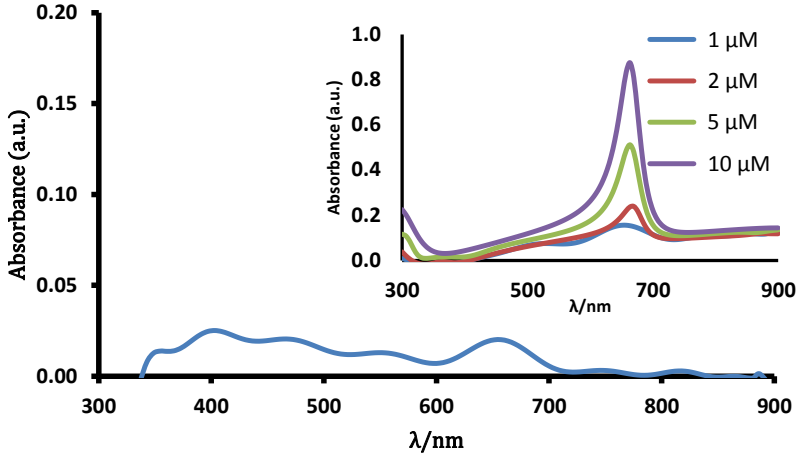

Figure 6.16 – UV-Vis spectra for the detection of MB due to vesicle burst. The inset shows the UV-Vis spectra for different concentrations of MB, used as calibration.

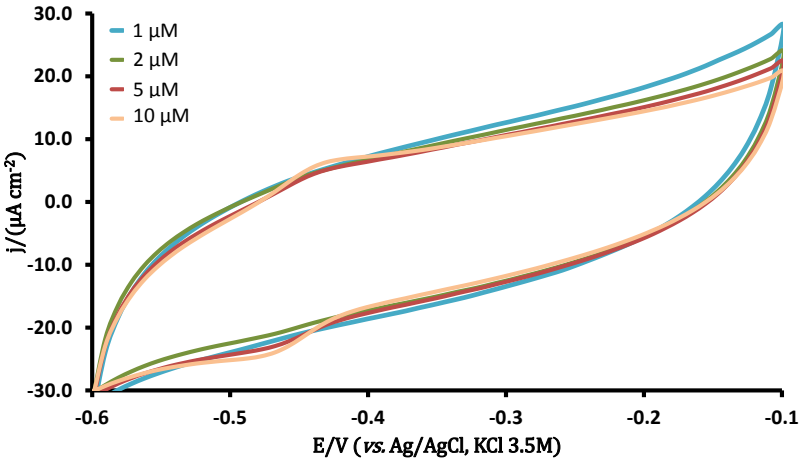

Figure 6.17 – Cyclic voltammograms of solutions of MB with different concentration, using PBS (pH=7.4) as background. The lower detectable amount of MB is 5 µM.

6.2.4. Kinetics of Electron Transfer

In redox active proteins the potential independent electron tunnelling coefficient is given by,

$$\beta = \rho \times 0.9\text{Å}^{-1} + (1 - \rho) \times 2.8\text{Å}^{-1} \qquad (6.1)$$

where ρ represents the density packing of protein atoms; ρ presents a value between 0 and 1, with 1 corresponding to a fully packed medium (β=0.9Å^{-1}) and 0 corresponding to

the interstitial space in the protein structure outside the united van der Walls atomic radii (β=2.8 Å^{-1}).[61,62] Experimentally, it has been shown that β usually presents an intermediate value between the two extremes (β=1.4±0.2 Å^{-1}).[63]

Using the same approach that was used in chapters 4 and 5, the theoretical rate of electron transfer can be calculated for the SAM of avidin (assuming that avidin presents the same β value of proteins with redox properties, although it is not a redox protein). This yields values of k_{th}^0 in the order of 10^{-26} cm s^{-1} for $Fe(CN)_6^{3-/4-}$ and in the order of 10^{-25} cm s^{-1} for $Ru(NH_3)_6^{3+/2+}$. These values are extremely small are very unlikely to be representative of the reality, especially in the case of $Ru(NH_3)_6^{3+/2+}$ where both CV (figure 6.8) and EIS (figure 6.9) show that electron transfer occurs.

The apparent rate of electron transfer (k_{app}^0) is dependent of the resistance of charge transfer and, using equation (4.15), it yields values in the order of 10^{-5} cm s^{-1} for both electroactive couples. Comparing the values of k_{app}^0 with the values of k_{th}^0 shows a difference of 20 – 21 orders of magnitude which is a "good" indication that this method is not applicable.

In the case of the BLM the values of k_{app}^0 are in the order of 10^{-7} cm s^{-1} for both $Fe(CN)_6^{3-/4-}$ and $Ru(NH_3)_6^{3+/2+}$, which is similar to the values of k_{app}^0 presented in chapter 5 for these electroactive couples (table 5.2).

6.3. Conclusions

The formation of sBLMs taking advantage of the strong avidin – biotin interaction was achieved by bursting vesicles that contained DOPE(B), a biotin modified lipid. The vesicles were linked to avidin that was previously deposited on a platinum substrate by the biotin of present in the DOPE(B) lipid. When +0.7V (*vs.* Ag/AgCl, KCl 3.5M) was applied to the

solution, the vesicles burst and lead to the formation of the sBLMs. This method of producing sBLMs from vesicle burst has the advantage of bursting the vesicles without the need of other chemicals/molecules used to create osmotic pressure.

References

(1) Mueller, P.; Rudin, D. O.; Tien, H. T.; Wescott, W. C. *Nature* **1962**, *194*, 979–980.
(2) Sackmann, E. *Science* **1996**, *271*, 43–48.
(3) Brian, A. A.; McConnell, H. M. *PNAS* **1984**, *81*, 6159–6163.
(4) Heim, M.; Cevc, G.; Guckenberger, R.; Knapp, H. F.; Wiegräbe, W. *Biophys. J.* **1995**, *69*, 489–497.
(5) Seeger, H. M.; Cerbo, A. D.; Alessandrini, A.; Facci, P. *J. Phys. Chem. B* **2010**, *114*, 8926–8933.
(6) Hartshorn, C. M.; Jewett, C. M.; Brozik, J. A. *Langmuir* **2010**, *26*, 2609–2617.
(7) Wagner, M. L.; Tamm, L. K. *Biophys J* **2000**, *79*, 1400–1414.
(8) Cho, N.-J.; Frank, C. W.; Kasemo, B.; Hook, F. *Nat. Protocols* **2010**, *5*, 1096–1106.
(9) Zhu, T.; Xu, F.; Yuan, B.; Ren, C.; Jiang, Z.; Ma, Y. *Colloid Surface B* **2012**, *89*, 228–233.
(10) Spinke, J.; Yang, J.; Wolf, H.; Liley, M.; Ringsdorf, H.; Knoll, W. *Biophys. J.* **1992**, *63*, 1667–1671.
(11) Kühner, M.; Tampé, R.; Sackmann, E. *Biophys. J.* **1994**, *67*, 217–226.
(12) Seitz, M.; Ter-Ovanesyan, E.; Hausch, M.; Park, C. K.; Zasadzinski, J. A.; Zentel, R.; Israelachvili, J. N. *Langmuir* **2000**, *16*, 6067–6070.
(13) Snejdarkova, M.; Rehak, M.; Otto, M. *Anal. Chem.* **1993**, *65*, 665–668.
(14) Rehák, M.; Šnejdárková, M.; Otto, M. *Biosens. Bioelectron.* **1994**, *9*, 337–341.
(15) Hianik, T.; Snejdarkova, M.; Cervenanska, Z.; Miernik, A.; vel Krawczyk, T. K.; Trojanowicz, M. *Chem. Anal. (Warsaw)* **1997**, *42*, 901–906.
(16) Proux-Delrouyre, V.; Elie, C.; Laval, J.-M.; Moiroux, J.; Bourdillon, C. *Langmuir* **2002**, *18*, 3263–3272.
(17) Fliniaux, O.; Elie-Caille, C.; Pantigny, J.; Bourdillon, C. *Electrochem. Commun.* **2005**, *7*, 697–702.
(18) Green, N. M. *Biochem. J.* **1963**, *89*, 585–591.
(19) Hermanson, G. T. In *Bioconjugate Techniques*; Academic Press: San Diego, 1996; pp. 570–592.
(20) Anzai, J.; Hoshi, T.; Osa, T. *Chem. Lett.* **1993**, *22*, 1231–1234.
(21) Hoshi, T.; Hiwatashi, Y.; Anzai, J.-I. *ITE Lett Batter New Technol Med* **2004**, *5*, 552–555.
(22) Haugland, R. P.; You, W. W. In *Avidin–Biotin Interactions*; McMahon, R. J., Ed.; Humana Press: Totowa, NJ, 2008; Vol. 418, pp. 13–23.
(23) Bruch, R. C.; White, H. B. *Biochemistry* **1982**, *21*, 5334–5341.
(24) Livnah, O.; Bayer, E. A.; Wilchek, M.; Sussman, J. L. *PNAS* **1993**, *90*, 5076 –5080.
(25) Pugliese, L.; Malcovati, M.; Coda, A.; Bolognesi, M. *J. Mol. Biol.* **1994**, *235*, 42–46.
(26) RCSB Protein Data Bank http://www.rcsb.org/pdb/explore/explore.do?structureId=1VYO (accessed Nov 25, 2011).
(27) Cuatrecasas, P.; Wilchek, M. *Biochem. Biophys. Res. Commun.* **1968**, *33*, 235–239.
(28) Bodanszky, A.; Bodanszky, M. *Specialia* **1970**, *26*, 327–327.
(29) Pacheco-Alvarez, D.; Solórzano-Vargas, R. S.; Del Río, A. L. *Arch. Med. Res.* **2002**, *33*, 439–447.
(30) Staggs, C. G.; Sealey, W. M.; McCabe, B. J.; Teague, A. M.; Mock, D. M. *J. Food Compos. Anal.* **2004**, *17*, 767–776.
(31) Healy, S.; Perez-Cadahia, B.; Jia, D.; McDonald, M. K.; Davie, J. R.; Gravel, R. A. *BBA - Gene Regul. Mech.* **2009**, *1789*, 719–733.
(32) Proux-Delrouyre, V.; Laval, J.-M.; Bourdillon, C. *J. Am. Chem. Soc.* **2001**, *123*, 9176–9177.

(33) Jung, L. S.; Shumaker-Parry, J. S.; Campbell, C. T.; Yee, S. S.; Gelb, M. H. *J. Am. Chem. Soc.* **2000**, *122*, 4177–4184.
(34) Burgess, S. W.; McIntosh, T. J.; Lentz, B. R. *Biochemistry* **1992**, *31*, 2653–2661.
(35) Lee, J.; Lentz, B. R. *PNAS* **1998**, *95*, 9274–9279.
(36) Burridge, K. A.; Figa, M. A.; Wong, J. Y. *Langmuir* **2004**, *20*, 10252–10259.
(37) Hellberg, D.; Scholz, F.; Schauer, F.; Weitschies, W. *Electrochem. Commun.* **2002**, *4*, 305–309.
(38) Berne, B. J.; Pecora, R. *Dynamic light scattering: with applications to chemistry, biology, and physics*; Courier Dover Publications, 2000.
(39) Clark, N. A. *Am. J. Phys.* **1970**, *38*, 575–585.
(40) Dawson, R. M. C.; Elliott, D. C.; Elliott, W. H.; Jones, K. M. In *Data for biochemical research*; Oxford University Press, Inc: New York, 1986.
(41) Anzai, J.; Hoshi, T.; Lee, S.; Osa, T. *Sens. Actuators, B* **1993**, *13*, 73–75.
(42) Hoshi, T.; Anzai, J.; Osa, T. *Anal. Chim. Acta* **1994**, *289*, 321–327.
(43) Anzai, J.-I.; Osa, T. In *Advances in Supramolecular Chemistry, Volume 4*; JAI Press: London, UK, 1997; pp. 143–163.
(44) Hoshi, T.; Anzai, J.; Osa, T. *Anal. Chem.* **1995**, *67*, 770–774.
(45) Cline, K. K.; McDermott, M. T.; McCreery, R. L. *J. Phys. Chem.* **1994**, *98*, 5314–5319.
(46) Bard, A. J.; Faulkner, L. R. *Electrochemical methods: fundamentals and applications*; 2nd ed.; John Wiley & Sons: New York, 2001.
(47) Bard, A. J. *J. Am. Chem. Soc.* **2010**, *132*, 7559–7567.
(48) Xiao, X.; Pan, S.; Jang, J. S.; Fan, F.-R. F.; Bard, A. J. *J. Phys. Chem. C* **2009**, *113*, 14978–14982.
(49) Manheller, M.; Karthaeuser, S.; Blech, K.; Simon, U.; Waser, R. In *2010 10th IEEE Conference on Nanotechnology (IEEE-NANO)*; IEEE, 2010; pp. 919–923.
(50) Steiger, B.; Padeste, C.; Grubelnik, A.; Tiefenauer, L. *Electrochim. Acta* **2003**, *48*, 761–769.
(51) Janshoff, A.; Steinem, C. *Anal. Bioanal.Chem.* **2006**, *385*, 433–451.
(52) Plant, A. L.; Gueguetchkeri, M.; Yap, W. *Biophys. J.* **1994**, *67*, 1126–1133.
(53) Schiller, S. M.; Naumann, R.; Lovejoy, K.; Kunz, H.; Knoll, W. *Angew. Chem. Int. Ed.* **2003**, *42*, 208–211.
(54) Jeuken, L. J. C.; Bushby, R. J.; Evans, S. D. *Electrochem. Commun.* **2007**, *9*, 610–614.
(55) Steinem, C.; Janshoff, A.; Ulrich, W.-P.; Sieber, M.; Galla, H.-J. *Biochim. Biophys. Acta, Biomembr.* **1996**, *1279*, 169–180.
(56) Dilger, J.; McLaughlin, S.; McIntosh, T.; Simon, S. *Science* **1979**, *206*, 1196 –1198.
(57) Diao, P.; Jiang, D.; Cui, X.; Gu, D.; Tong, R.; Zhong, B. *Bioelectrochem. Bioenerg.* **1998**, *45*, 173–179.
(58) Cheng, Y.; Cunnane, V. J.; Kontturi, A.-K.; Kontturi, K.; Schiffrin, D. J. *J. Phys. Chem.* **1996**, *100*, 15470–15477.
(59) Vockenroth, I. K.; Atanasova, P. P.; Long, J. R.; Jenkins, A. T. A.; Knoll, W.; Köper, I. *Biochim. Biophys. Acta, Biomembr.* **2007**, *1768*, 1114–1120.
(60) Naumowicz, M.; Figaszewski, Z. *Bioelectrochemistry* **2003**, *61*, 21–27.
(61) Page, C. C.; Moser, C. C.; Chen, X.; Dutton, P. L. *Nature* **1999**, *402*, 47–52.
(62) Gray, H. B.; Winkler, J. R. *Q Rev Biophys* **2003**, *36*, 341–372.
(63) Moser, C. C.; Keske, J. M.; Warncke, K.; Farid, R. S.; Dutton, P. L. *Nature* **1992**, *355*, 796–802.

7. Conclusion and Future Work

Self – assembled monolayers (SAMs) and bilayer lipid membranes (BLMs) have a wide range of applications; they are used in biosensors[1–3], as mimic of the cell membrane for studies of ion[4–6] and electron transport[7,8], as mimics of the cell membrane transport functions[6,9–15] and many others. Because these structures are so important, fundamental studies are essential. The objective of the work presented in this thesis is the development and characterisation of SAMs and BLMs in terms of electron transfer kinetics, to enable understanding of fundamental concepts of coverage, integrity of SAMs and BLMs their charge transport behaviour and the application of BLMs as cellular membrane mimics.

Initially, the blocking behaviour of the DPPTE and DPPTE+EggPC SAMs was studied using SAMs of two alkanethiols (heptanethiol – HPT and dodecanethiol – DDT) as model systems. Voltammetric studies show that HPT SAMs have pinholes; the CV presents a shape indicating that the diffusion layers of the pinholes interact, leading to a behaviour intermediate between macro- and microelectrode. In the case of SAMs of DDT, DPPTE and DPPTE+EggPC the Faradaic process is completely inhibited. Additionally, the EIS measurements present a semicircle in the entire frequency range indicating that the film formed is well organised and pinhole free. The influence of the applied potential to the stability of the SAMs was studied. It was shown that, although the capacitance is constant, the charge transfer resistance decreases when the applied potential is far from the

equilibrium potential. Conformational changes in the structure of the SAMs led to the formation of defects that decreased the distance between the electroactive couple and the electrode surface.

SAMs of DPPTE and DPPTE+EggPC were characterised in order to evaluate which presented best properties to be used as the lower leaflet of tethered bilayer lipid membranes (tBLMs). Although both DPPTE and DPPTE+EggPC SAMs were of good quality, the later seems to be of better quality, so this is the monolayer that was used to produce tBLMs.

Tethered bilayer lipid membranes (tBLMs) were made using a SAM of DPPTE+EggPC as the lower leaflet and using the process of vesicle fusion to deposit the second layer. The behaviour of the tBLMs was compared to that of pore suspended bilayer lipid membranes (psBLMs). Both types of BLM were characterised in terms of electron transfer using three different probe molecules – $Ru(NH_3)_6^{3+/2+}$, $Fe(CN)_6^{3-/4-}$ and NAD^+/NADH. No significant differences were observed between outer $\left(Ru(NH_3)_6^{3+/2+}\right)$ and inner $\left(Fe(CN)_6^{3-/4-}\right)$ sphere electron transfer mechanisms or the biologically relevant NAD^+/NADH.

The comparison between the experimental (k_{app}^0) and theoretical (k_{th}^0) rates of electron transfer showed a difference of several orders of magnitude when the potential independent electron tunnelling coefficient (β) value used was the one present in previous literature[16]. Because the BLMs produced showed values of capacitance and resistance characteristic of good quality bilayers, a different value of β was used. Based on the conclusions of Mirkin and Bard[17], a value of β about one – half of that previously reported was used; this resulted in the differences between the apparent and the standard rate constant caused by electron tunnelling being much smaller. Therefore, is

concluded that β for electron tunnelling through a phospholipid bilayer is of the order of $0.38Å^{-1}$.

The tBLMs and the psBLMs were modified with two bioactive molecules (ubiquinone 10 (UQ_{10}) and α – tocopherol (VitE)) and an equimolar mixture of the two molecules. Electron transfer does not occur when the films were modified with VitE or the equimolar mixture of UQ_{10} and VitE. Electron transfer when the BLMs (both tBLMs and psBLMs) were modified with UQ_{10} is observed in the CVs and in the Nyquist plots of the EIS data.

The same method that was used to analyse electron rate transfer in SAMs and tBLMs can be used to analyse the kinetics of electron transfer in psBLMs. This method of determination of the rate constants is very important because allows a better characterisation of the film formed.

Tethered BLMs are more stable and robust than psBLMs but the procedure that leads to its formation is slow (24 hours for SAM deposition and a few more hours for the deposition of the second layer). With this in mind an approach based on the strong avidin – biotin interaction was used to produce BLMs.

The formation of BLMs taking advantage of the strong avidin – biotin interaction was achieved by depositing avidin on a Pt electrode and then bursting vesicles that contained 4% (molar ratio) of DSPE, a biotin modified lipid. This is achieved in less than an hour and produces BLMs of good quality as the studies made using CV and EIS have shown. The vesicles were burst by applying +0.7V (*vs.* Ag/AgCl, KCl 3.5M); this method of bursting the vesicles has the advantage of avoiding the addition of other chemicals/molecules to the solution in order to create the osmotic pressure that leads to vesicle burst.

The work presented in this thesis can/should be developed further. In the case of the tBLMs and psBLMs, future studies should include thiolipids of different lengths in order to experimentally determine β.

For the BLMs based on the avidin – biotin interaction, further studies should include the use of different biotin modified lipids and the use of modified forms of avidin (streptavidin, neutravidin) are steps that need to be carried so that this type of BLM can be a real alternative to the more usual tBLMs.

In the case of the BLMs modified with bioactive molecules, future work should go in the direction of adding more, or other, proteins to the bilayer in order to make a better mimic of the cell membrane. 615 types of proteins have been identified from the human cardiac mitochondria[18] so the choice should focus on those that are directly involved in the ion transport process.

References

(1) Wink, T.; Zuilen, S. J. van; Bult, A.; Bennekom, W. P. van *Analyst* **1997**, *122*, 43R–50R.
(2) Castellana, E. T.; Cremer, P. S. *Surf. Sci. Rep.* **2006**, *61*, 429–444.
(3) Tien, H. T. *J. Clin. Lab. Anal.* **1988**, *2*, 256–264.
(4) Shirai, O.; Kihara, S.; Suzuki, M.; Ogura, K.; Matsui, M. *Anal. Sci.* **1991**, *7 (Suppl)*, 607–610.
(5) Shirai, O.; Kihara, S.; Yoshida, Y.; Matsui, M. *J. Electroanal. Chem.* **1995**, *389*, 61–70.
(6) Ozaki, S.; Aoki, S.; Hibi, T.; Kano, K.; Shirai, O. *Electrochem. Commun.* **2008**, *10*, 1509–1512.
(7) Shiba, H.; Maeda, K.; Ichieda, N.; Kasuno, M.; Yoshida, Y.; Shirai, O.; Kihara, S. *J. Electroanal. Chem.* **2003**, *556*, 1–11.
(8) Crane, F. L.; Sun, I. L.; Barr, R.; Löw, H. *J. Bioenerg. Biomembr.* **1991**, *23*, 773–803.
(9) Lundbaek, J. A.; Collingwood, S. A.; Ingolfsson, H. I.; Kapoor, R.; Andersen, O. S. *J. R. Soc. Interface* **2010**, *7*, 373–395.
(10) Schmitt, E. K.; Weichbrodt, C.; Steinem, C. *Soft Matter* **2009**, *5*, 3347–3353.
(11) Becucci, L.; Innocenti, M.; Salvietti, E.; Rindi, A.; Pasquini, I.; Vassalli, M.; Foresti, M. L.; Guidelli, R. *Electrochim. Acta* **2008**, *53*, 6372–6379.
(12) Shirai, O.; Yoshida, Y.; Kihara, S.; Ohnuki, T.; Uehara, A.; Yamana, H. *J. Electroanal. Chem.* **2006**, *595*, 53–59.
(13) Pan, J.; Tieleman, D. P.; Nagle, J. F.; Kučerka, N.; Tristram-Nagle, S. *BBA - Biomembranes* **2009**, *1788*, 1387–1397.
(14) Oliynyk, V.; Jäger, M.; Heimburg, T.; Buckin, V.; Kaatze, U. *Biophys. Chem.* **2008**, *134*, 168–177.
(15) Jadhav, S. R.; Sui, D.; Garavito, R. M.; Worden, R. M. *J. Colloid Interface Sci.* **2008**, *322*, 465–472.
(16) Diao, P.; Jiang, D.; Cui, X.; Gu, D.; Tong, R.; Zhong, B. *Bioelectrochem. Bioenerg.* **1998**, *45*, 173–179.
(17) Tsionsky, M.; Bard, A. J.; Mirkin, M. V. *J. Am. Chem. Soc.* **1997**, *119*, 10785–10792.
(18) Taylor, S. W.; Fahy, E.; Zhang, B.; Glenn, G. M.; Warnock, D. E.; Wiley, S.; Murphy, A. N.; Gaucher, S. P.; Capaldi, R. A.; Gibson, B. W.; Ghosh, S. S. *Nat Biotech* **2003**, *21*, 281–286.

Appendix

A1. Geometrical derivation of Marcus equation

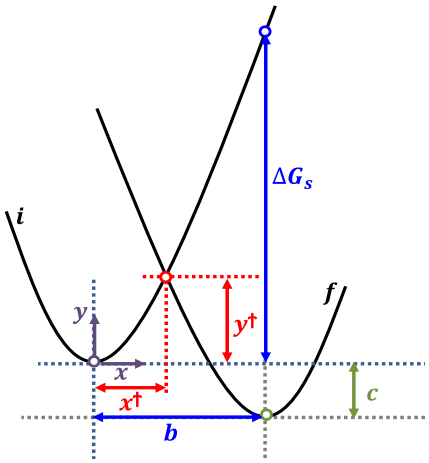

Figure A.1 – Geometrical derivation of Marcus theory.

Paraboles:

$$y_i = ax^2$$

$$y_f = a(x+b)^2 + c$$

Intersection $(x^\dagger, y^\dagger)$:

$$y^\dagger = a\left(x^\dagger\right)^2 = a\left(x^\dagger + b\right)^2 + c$$

$$a\left(x^\dagger\right)^2 = a\left(x^\dagger\right)^2 + 2abx^\dagger + (ab^2 + c)$$

$$2abx^\dagger = -ab^2 - c$$

$$x^\dagger = \frac{-(ab^2 + c)}{2ab}$$

$$y^\dagger = a\left(x^\dagger\right)^2 = \frac{(ab^2 + c)^2}{4ab^2}$$

$$\left.\begin{array}{c} \Delta G_s = ab^2 \\ \Delta G = c \\ \Delta G^\ddagger = y^\dagger \end{array}\right\} \Delta G^\ddagger = \frac{(\Delta G + \Delta G_s)^2}{4\Delta G_s}$$

A2. The Laplace Transform

The Laplace transform $f(s)$ for a function F(t) is

$f(s) = \mathcal{L}\{F(t)\} = \int_0^\infty \exp(-st)\, F(t)dt$

with s being a number sufficiently large for the integral to converge.

Some of the most used Laplace transforms are shown in the table below.

Table A.1 – Laplace transforms.

F(t)	$f(s)=\mathcal{L}\{F(t)\}$
1	$\frac{1}{s}$
t	$\frac{1}{s^2}$
$t^{n-1}/(n-1)!$	$\frac{1}{s^n}$
$\frac{1}{\sqrt{\pi}t}$	$\frac{1}{\sqrt{s}}$
$2\sqrt{\frac{t}{\pi}}$	$s^{-3/2}$
t^{k-1}	$\frac{\Gamma(k)}{s^k}, (k>0)$
$\exp(-at)$	$(s+a)^{-1}$
$t\exp(-at)$	$(s+a)^{-2}$
$a^{-1}\sin at$	$(s^2+a^2)^{-1}$
$\cos at$	$\frac{s}{(s^2+a^2)}$
$a^{-1}\sinh at$	$(s^2-a^2)^{-1}$
$\cosh at$	$\frac{s}{(s^2-a^2)}$

$\frac{k}{2\sqrt{\pi t^3}} exp\left(\frac{-k^2}{4t}\right)$	$\exp\left(-k\sqrt{s}\right), k > 0$
$erfc\frac{k}{2\sqrt{t}}$	$\frac{1}{s}\exp\left(-k\sqrt{s}\right), k \geq 0$
$\frac{1}{\sqrt{\pi t}} exp\left(\frac{-k^2}{4t}\right)$	$\frac{1}{\sqrt{s}}\exp\left(-k\sqrt{s}\right), k \geq 0$
$2\sqrt{\frac{t}{\pi}} exp\left(\frac{-k^2}{4t}\right) - k\ \text{erfc}\frac{k}{\sqrt{t}}$	$\frac{1}{s^{3/2}}\exp\left(-k\sqrt{s}\right), k \geq 0$
$\frac{1}{\sqrt{\pi t}} - a\exp(a^2 t)\ \text{erfc}\ a\sqrt{t}$	$\left(s^{1/2} + a\right)^{-1}$
$\frac{1}{\sqrt{\pi t}} + a\exp(a^2 t)\ \text{erfc}\ a\sqrt{t}$	$\frac{\sqrt{s}}{(s - a^2)}$
$\frac{1}{a}\exp(a^2 t)\ \text{erfc}\ a\sqrt{t}$	$\left[\sqrt{s}(s - a^2)\right]^{-1}$
$\exp(a^2 t)\ \text{erfc}\ a\sqrt{t}$	$\left[\sqrt{s}\left(\sqrt{s} + a\right)\right]^{-1}$